Precipitation of Metal Sulfides in Zinc Solutions

Mikael Manninen

Master's Thesis

Degree Program of Chemistry

University of Oulu

2021

ABSTRACT

Metal sulfide precipitation has long been recognized as an efficient technique to reduce the levels of harmful metals in wastewater towards acceptable limits. Advantages of the method include fast reaction rates, good settling properties of the precipitates, and the extremely low solubilities of most metal sulfides. Unfortunately, implementing sulfide precipitation has its challenges also. For example, the low solubilities easily lead to extremely high supersaturation levels, which can make the process difficult to control. Another disadvantage is the toxicity of sulfide to humans and to the environment. Especially, the generation of hydrogen sulfide can be a concern in certain conditions. To design and operate a sulfide precipitation process in a safe and efficient manner, a good understanding of the phenomena underlying the process is required.

This thesis aims to provide a summary of the theories needed to build a useful conceptual model of the sulfide precipitation process, based on an extensive review of the current scientific literature on metal sulfide systems. The knowledge of these theoretical principles can aid the engineers designing and operating these processes to direct their attention to essential issues in the process. Unfortunately, space limitations require many important details to be left outside the discussion, but I have tried to include references to sources in which these details can be found.

The focus of the thesis is on the solution chemistry and thermodynamics governing sulfide precipitation. Special emphasis has been given to solubility phenomena and modelling of equilibrium systems. In addition, chemical dynamics of the process has been discussed. Thermodynamics provides the means to quantify supersaturation, predict which phases will be stable under given conditions, and predict the solubilities of these phases. All this information can be of enormous practical value but since the timescales of precipitation processes are relatively short, kinetics is also required to complete the image. For example, the rates of nucleation, crystal growth, and aggregation strongly affect the particle size of the obtained precipitates. Finally, modelling mass transfer inside the reactor accurately requires the incorporation of fluid mechanics. Only by combining thermodynamics, kinetics, and fluid mechanics, a complete image of the sulfide precipitation process can be obtained. It is obvious that building a quantitative model incorporating all these aspects can be an overwhelming task.

Fortunately, in many cases, more straightforward approaches, that utilize simplifying assumptions, can still provide valuable information about the process.

TIIVISTELMÄ

Metallien saostus sulfideina on tunnettu jo pitkään lupaavana ja potentiaalisesti tehokkaana menetelmänä haitallisten metallien poistamiseksi jätevedestä. Menetelmän etuja ovat nopeat reaktiot, saostumien hyvät laskeutumisominaisuudet sekä useimpien metallisulfidien erittäin alhaiset liukoisuudet. Sulfidisaostukseen liittyy kuitenkin myös omat hankaluutensa. Alhaisista liukoisuuksista seuraa, että liuoksista tulee helposti erittäin ylikylläisiä, mikä voi tehdä prosessista vaikeasti ohjattavan. Haittapuolena on myös sulfidikemikaalien myrkyllisyys ihmisille ja ympäristölle. Varsinkin myrkyllisen vetysulfidin kehittyminen voi olla suuri huolenaihe. Jotta sulfidisaostusprosessia voitaisiin turvallisesti ja tehokkaasti operoida, on ymmärrettävä prosessin taustalla piileviä ilmiöitä.

Tämän opinnäytetyön tarkoituksena on aihetta käsittelevään tieteelliseen kirjallisuuteen pohjautuen luoda katsaus teorioihin, jotka antavat työkalut luoda käyttökelpoinen käsitteellinen malli prosessista. Näiden periaatteiden tunteminen voi auttaa prosessin parissa työskenteleviä asiantuntijoita suuntaamaan huomionsa olennaisiin asioihin prosessissa. Valitettavasti paljon tärkeitä yksityiskohtia on jouduttu jättämään tarkastelun ulkopuolelle tilarajoitteista johtuen, mutta olen pyrkinyt sisällyttämään mahdollisimman kattavasti viitteitä lähteisiin, joista tarkempaa tietoa voi löytää.

Tarkastelun pääpaino on metallisulfidisysteemien termodynamiikassa ja erityisesti liukoisuuksien mallintamisessa, mutta myös prosessin dynamiikka ansaitsee osansa huomiosta. Termodynamiikka mahdollistaa esimerkiksi ylikylläisyyden kvantifioinnin sekä stabiilien faasien ja niiden liukoisuuksien ennustamisen. Kaikella tällä informaatiolla voi olla erittäin suuri käytännön arvo, mutta koska saostusprosessien viipymäajat ovat verrattain lyhyitä, myös kinetiikkaa tarvitaan viimeistelemään kokonaiskuva prosessista. Esimerkiksi ydintymisen, kiteenkasvun ja aggregaation nopeudet pitkälti määräävät saostuvien partikkelien kokojakauman. Reaktorissa tapahtuvan aineensiirron kuvaamiseksi tarvitaan lisäksi myös virtausmekaniikkaa. Sulfidisaostusprosessin täydelliseen kuvaamiseen vaaditaan siis termodynamiikan, kinetiikan ja virtausmekaniikan yhdistämistä. On selvää, että kaikki nämä aspektit huomioivan kvantitatiivisen mallin luominen voi olla ylivoimainen tehtävä, mutta

monissa tapauksissa yksinkertaistavia oletuksia hyödyntävät suoraviivaisemmat lähestymistavatkin voivat antaa arvokasta tietoa prosessista.

ABBREVIATIONS AND SYMBOLS

Abbreviations

CSTR	Continuous stirred tank reactor
DFT	Density functional theory
IEM	Interaction by exchange with the mean
IEP	Isoelectric point
MSMPR	Mixed-Suspension-Mixed-Product-Removal (A reactor type)
PNC	Pre-nucleation cluster
PSD	Particle size distribution
SCE	Saturated calomel electrode
SHE	Standard hydrogen electrode

Latin symbols

A	Area, m^2, or Debye-Hückel parameter depending on context
a	Activity
B	Empirical constant, see context
C	Number of components in a system or an empirical parameter depending on context
C_ξ	Micromixing constant
c	Concentration, $\mathrm{mol\ l^{-1}}$
D	Diffusion constant, $\mathrm{m^2\ s^{-1}}$
Eh	Oxidation/Reduction potential, V
F	Degrees of freedom or the Faraday constant, $\mathrm{C\ mol^{-1}}$
F_0	Polynomial used in the DeFord and Hume methodology
d_m	Molecular-, or ionic diameter, m
e	Elementary charge, $1.602176634 \cdot 10^{-19}$ C
G	Gibbs free energy, J
G_r	Linear growth rate, $\mathrm{m\ s^{-1}}$

H	Enthalpy, J
I	Ionic strength, mol kg^{-1}
I_p	Peak current, A
J	Nucleation rate, s^{-1}
K	Thermodynamic equilibrium constant
k	Boltzmann constant, $1.3806505 \cdot 10^{-23}$ J K^{-1}
k_turb	Turbulent kinetic energy, $\mathrm{m}^2\mathrm{s}^{-2}$
k_x	Empirical constant, x denotes an arbitrary subscript
k^m	Henry's law constant, Pa kg mol^{-1}
L	Particle size, m
M	Molar mass, kg mol^{-1}
m	molality, mol kg^{-1}
N	Number of molecules or ions
n	population density, amount of substance, number of electrons transferred or empirical constant depending on context
P	Number of phases in a system
P_A	Aggregation probability
p	Pressure, Pa
Q	Reaction quotient
R	The universal gas constant, 8.314 J mol^{-1} K^{-1}
r	Radius, m
S	Entropy, J K^{-1},
S_sat	Supersaturation
Sc	Schmidt number, $\mathrm{Sc} = \nu/D$
T	Temperature, K
U	Internal energy, J
v	Stoichiometric number (negative for reactants, positive for products)
v_i	Velocity, m s^{-1}
v_m	Volume of one molecule, m^3
V	Volume, m^3
V_m	Molar volume, m^3 mol^{-1}
V_MeX	Partial molar volume of species MeX, m^3 mol^{-1}

$\dot{V}$	Volumetric flow rate, $m^3\ s^{-1}$
W	Work, J
w	mass, kg

Greek Symbols

β_{agg}	Aggregation Kernel
β_{col}	Collision Kernel
β_n	n^{th} successive formation constant of a complex
γ	Activity coefficient, molality basis
ϵ_0	Permittivity of vacuum, $8.854187817 \cdot 10^{-12}\ C^2\ N^{-1}\ m^{-2}$
ϵ_r	Relative permittivity of the medium
ε	Turbulent kinetic energy dissipation rate, $m^2\ s^{-3}$
κ	Debye-Hückel parameter, m^{-1}
μ	Chemical potential, $J\ mol^{-1}$
ν	Kinematic viscosity, $m^2 s^{-1}$
σ	Surface energy, $J\ m^{-2}$
τ	Residence time, s
ψ	Electric potential, V

Superscripts

aq	Aqueous phase
s	Solid phase
ref	Arbitrary reference state
α	Phase α
$*$	Denotes the properties of a nucleus of critical size

Subscripts

eq	Equilibrium
OS	Outer sphere complex
sp	Solubility product
$+$	Cation
$-$	Anion
$\pm$	Mean property of an electrolyte

TABLE OF CONTENTS

1. INTRODUCTION

Chemical precipitation is probably the most common method to remove harmful but potentially valuable heavy metals, such as zinc, cadmium, lead etc. from industrial wastewaters.[1] In chemical precipitation, a precipitant, usually a salt containing a suitable anion such as OH^-, CO_3^{2-} or S^{2-}, with which the dissolved metals form insoluble species, is introduced to the system. The formed solids can then be removed from the system using a suitable separation technique such as filtration or settling. By careful selection and control of operation conditions such as pH and precipitant dosage, a high degree of selectivity can be achieved in the chemical precipitation of solutions containing several metals.

The term precipitation commonly refers to phenomena in which solid particles are rapidly formed from a liquid solution phase. The relatively rapid timescale of precipitation is what distinguishes it from the general term *crystallization*. Crystallization is often thought as a process in which solid crystals are formed in a controlled and at least seemingly reversible manner whereas precipitation occurs from clearly supersaturated solutions. Under highly supersaturated conditions the driving force of the precipitation is high, which results in favorable nucleation and consequently, crystals of small particle size are produced in great numbers. The extremely short timescales of many molecular scale subprocesses present complications in obtaining reliable experimental data of these phenomena. Precipitation processes are difficult to model, because the current knowledge of the actual mechanisms involved is limited and largely relies on empirical relations.[2]

This thesis deals with metal sulfide precipitation and the following chapters are intended to provide a comprehensive view on various theoretical topics that one should familiarize with to better understand what might be happening inside a sulfide precipitation reaction vessel and why. The objective of this thesis is to act as a reference that brings together the thermodynamic, kinetic and mass transfer aspects of metal sulfide precipitation and present an extensive summary of the existing literature on the topic.

1.1. Industrial Scale Precipitation of Metal Sulfides

Precipitation of metals as sulfides offers some advantages over the conventional hydroxide precipitation. These advantages include the generally lower solubilities of the precipitates, higher degree of achievable selectivity, rapid reaction rates, better settling properties and the potential commercial value of the precipitates as raw materials for metal refineries.[3, 4]

Metal sulfide precipitation processes have been successfully applied on industrial scale for several decades but still the full potential of sulfide precipitation remains to be harnessed. Although potentially more efficient compared to the more conventional hydroxide precipitation processes, the process is often thought to be difficult to control. This is mostly related to the fact that metal sulfides are more insoluble, and thus, the process is more sensitive to changes in precipitant dosage and operation conditions than the hydroxide precipitation process.[3] The actual implementation of sulfide precipitation varies according to the specific application, so no detailed flow sheet is given here but a general outline of possible practices is presented instead.

Precipitation is a seemingly simple operation, and it begins by introducing the precipitant, sulfide in this case, to the process solution. Due to the sparingly soluble nature of many metal sulfide salts, a precipitate then forms. Sulfide may be introduced to the system in several ways which include the addition of sulfide containing reagents, such as aqueous Na_2S, NaHS, $(NH_4)_2S$, solid FeS, CaS or gaseous H_2S.[3] Sulfide can also be introduced indirectly by a chemical reaction such as the decomposition of sodium thiosulfate or alternatively, a biological sulfate reduction scheme may be employed.[3] The biological sulfate reduction is not addressed further in this work, so the interested reader should refer to other sources for information on this topic.[5] Also, not much consideration will be given to the sulfide source in the later discussion since the focus of this text is on understanding the basic phenomena which occur after the sulfide has been introduced into the solution. Thus, the original source of the active species is usually not so important, although it may affect the precipitation indirectly by influencing the process conditions such as the ionic strength or pH. Gaseous hydrogen sulfide source may also allow for more accurate control of supersaturation conditions compared to aqueous sources such as $Na_2S\ (aq)$ which will be discussed later in a bit more detail.[6]

Industrial precipitation can be carried out in a continuous or (semi)batch operation mode of which the batch configuration is more commonly used.[2] The batch precipitator may consist of an agitated reaction vessel containing the solvent with the dissolved metal species and the

precipitant is fed to the vessel through an inlet pipe (jet) at some desired rate. Alternatively, a double-jet configuration might be used where the reactants are fed into the solvent containing vessel through their own separate inlets. Adjustment of the geometry and reactant flow rates especially in the case of a double jet system can greatly influence the properties, such as the particle size distribution of the formed precipitates by affecting the distribution of supersaturation inside the reactor.[2]

Continuous operation may be achieved by a so called Mixed-Suspension-Mixed-Product-Removal (MSMPR) reactor or a tubular crystallizer, for example (See Fig. 1). In the former, steady state operation of the stirred tank vessel is achieved by continuously supplying in fresh reagents and removing the precipitate as it is formed. In the latter operation mode, reactants are fed to a tubular reactor of a geometry designed to achieve the desired flow conditions. The reactants may be added from several inlets along the length of the reactor to avoid the development of zones of high local supersaturation and to ensure that the reactants are mixed thoroughly. Another way to control supersaturation is to introduce more solvent to the reactor from additional inlets to dilute the mixture.[2]

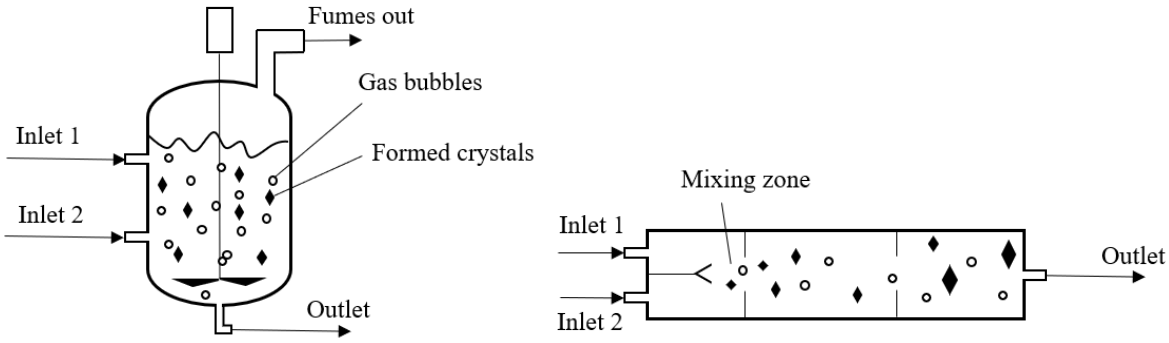

Figure 1. Simplified schematic illustrations of a MSMPR reactor (left), and a tubular crystallizer (right).

1.2. General Chemistry of Sulfide Precipitation

The basic chemical equilibria related to the sulfide precipitation are often, quite questionably as will be discussed shortly, represented as:

$$\mathrm{H_2S\,(aq) \rightleftharpoons HS^-(aq) + H^+(aq)} \quad \mathrm{p}K_{a1} = 6.98\ [\mathrm{T} = 298\ \mathrm{K}]^{7}, \tag{1}$$

$$\mathrm{HS^-(aq) \rightleftharpoons S^{2-}(aq) + H^+(aq)} \quad \mathrm{p}K_{a2} = 17.4\ [\mathrm{T} = 298\ \mathrm{K}]^{8}, \tag{2}$$

$$\mathrm{Me^{2+}(aq) + S^{2-}(aq) \rightleftharpoons MeS(s)}, \tag{3}$$

$$\mathrm{Me^{2+}(aq) + HS^-(aq) \rightleftharpoons MeS(s) + H^+(aq)}, \tag{4}$$

where $\mathrm{Me^{2+}}$ represents an arbitrary divalent metal cation that forms an insoluble sulfide. It should be noted that these reaction equations are drastic simplifications, and the actual mechanisms responsible for metal sulfide formation are much more complicated than indicated by these simple expressions. Experimental findings strongly suggest that metal sulfide complexes and clusters are likely to be involved as intermediate species in sulfide precipitation reactions.[9, 10] Despite not being mechanistically accurate, simple expressions like these can be useful since they can be used in thermodynamic or kinetic calculations in a rather straightforward manner. It is worth noting that especially the second dissociation constant of hydrogen sulfide in conjunction with Eqs. (2) and (3) should be viewed with considerable criticism. A variation of about seven orders of magnitude can be found in the reported literature values for K_{a2}.[8, 11] In fact, there is no evidence suggesting that $\mathrm{S^{2-}(aq)}$ exists at all under any conditions in which case Eqs. (2) and (3) would be simply wrong.[12]

Figure 2 shows the solubilities of selected metal sulfides and hydroxides as a function of pH. In Fig. 2, the formation of soluble metal sulfide species has been completely omitted, which is a very unrealistic assumption as will be seen later. As is obvious from Eqs. (1)–(4) and from Fig. 2, sulfide precipitation is strongly pH dependent. Due to this, and the fact that the solubilities of different metal sulfides differ in general quite much, a stepwise selective precipitation of different metal sulfides is possible.

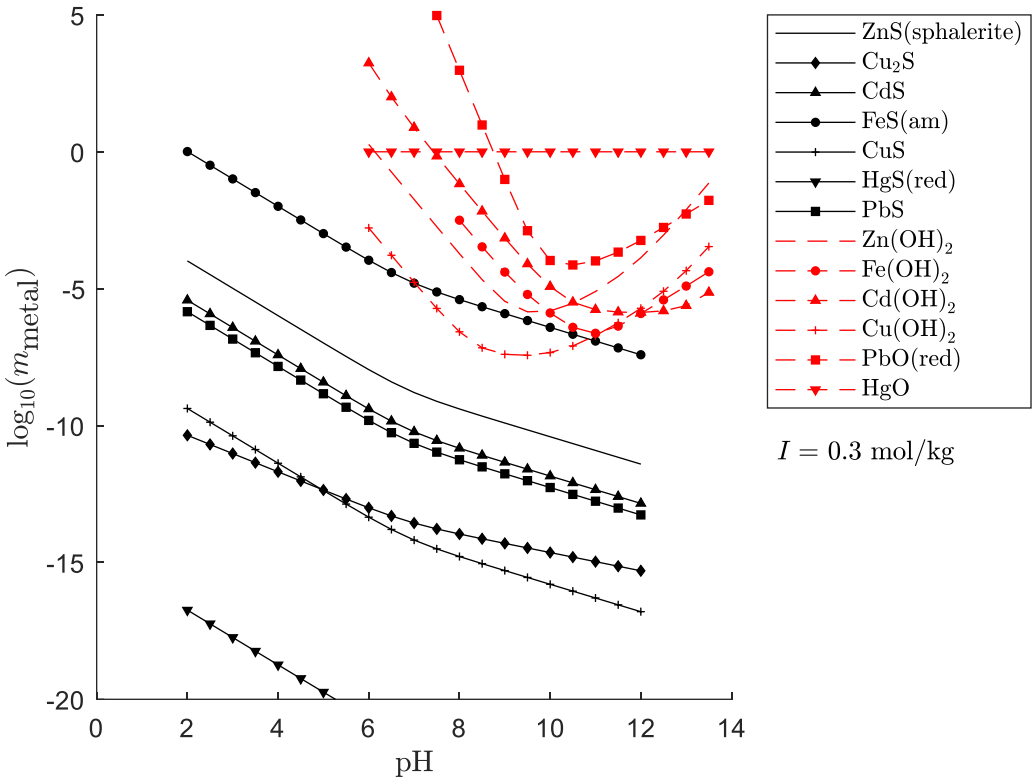

Figure 2. Solubilities of selected metal sulfides as predicted from the values of solubility products only (values from table 1). Solubility curves (considering complexation with OH^-) for metal hydroxides/oxides as a function of pH are shown for comparison. The equilibrium constants for the Fe-O-H system have been taken from Kim et al. (2017)[13] and the rest are from a series of IUPAC reports[14-18] containing critically evaluated thermodynamic data for the relevant systems.

1.3. Frequently Encountered Problems

Most problems associated with metal sulfide precipitation processes are related to difficulties in controlling the supersaturation levels that arise due to the extremely low solubilities of metal sulfides. High supersaturation causes nucleation to be the dominant mechanism of solid phase formation which in turn leads to the formation of vast amounts of fine particles that can be virtually impossible to separate from the solution.[19]

Another issue is the possible formation of soluble polysulfide- and bisulfide complexes which can increase the solubility of the metal sulfide phase when there is an excess of sulfide in the solution.[20] The speciation of metals in aqueous, sulfide containing solutions is not well understood[21], but some considerable research efforts have nevertheless been made to gain more insight on these issues, which will be discussed in section 2.4 in more detail. There are also

several papers suggesting the formation of soluble complexes to be a possible explanation for unexpectedly high metal concentrations observed in effluents of sulfide precipitation reactors.[19, 20, 22]

A notable and obvious shortcoming of sulfide precipitation processes is the possibility of the formation of highly toxic hydrogen sulfide gas. Also, the sulfide solutions and solid reagents itself are highly corrosive and dangerous to handle. This necessitates accurate control of reagent additions and often some pre- or post-treatment of the treated effluent.[23] To minimize the risks associated with the handling of large amounts of reactive sulfide chemicals, methods using a sparingly soluble sulfide compound, most notably FeS or CaS, as the sulfide source have been developed.[23, 24] The problem with these methods is the increased amount of sludge produced since only a small portion of the reagent is consumed in sulfidation.

2. GENERAL THEORY OF PRECIPITATION

By looking at Eqs. (1)–(4) one can quickly realize that if one wants to understand for example, how solid ZnS with crystals of a certain morphology (shape) forms, or predict the particle size distribution of the precipitate under certain operating conditions, these equations are of little use and more detailed knowledge of the mechanisms and the actual species involved in the formation of the solid phase is required. The classical crystallization theory forms a starting point for this discussion but the high supersaturation and rapid reaction rates typical to sulfide precipitation processes require that phenomena such as Ostwald ripening, particle crowding, aggregation and imperfect mixing must often be considered.[2] In the following sections a brief introduction to these topics and to the theory behind them is given on a general level. The contents of this chapter form a background for chapters 3 and 4 which concentrate more on the significance and the application of these concepts to sulfide precipitation systems. Chapter 3 is devoted to thermodynamics of aqueous metal sulfide systems whereas kinetics and mass transfer are discussed in more detail in chapter 4.

2.1. Supersaturation

Consider a system consisting of an arbitrary binary electrolyte MeX dissolved in water. The thermodynamic driving force of crystal formation is termed as *supersaturation*, which is defined as the difference in the chemical potential, $\Delta\mu$, of the dissolved compound in an infinitely large solution phase and that of an infinitely large solid MeX phase that would form at given pressure, temperature and solution composition. This is stated by

$$\Delta\mu = \mu_{\mathrm{MeX}}^{\mathrm{aq}} - \mu_{\mathrm{MeX}}^{\mathrm{s}}, \tag{5}$$

where $\mu_{\mathrm{MeX}}^{\mathrm{aq}}$ and $\mu_{\mathrm{MeX}}^{\mathrm{s}}$ are the chemical potentials of MeX in the aqueous and solid phases, respectively.[25] If the solid phase was formed, the system would eventually reach the new equilibrium at which it must hold $\mu_{\mathrm{MeX}}^{\mathrm{s}} = \mu_{\mathrm{MeX,eq}}^{\mathrm{aq}} = \mu_{\mathrm{Me}^{z+},\mathrm{eq}}^{\mathrm{aq}} + \mu_{\mathrm{X}^{z-},\mathrm{eq}}^{\mathrm{aq}}$. Using the relation $\mu_i = \mu_i^0 + RT\ln(a_i)$ and substituting these to Eq. (5) one gets the following form for the supersaturation:

$$\Delta\mu = \mu^{\mathrm{aq},0}_{\mathrm{MeX}} + RT\ln\left(a^{\mathrm{aq}}_{\mathrm{Me}^{z+}} a^{\mathrm{aq}}_{\mathrm{X}^{z-}}\right) - \left(\mu^{\mathrm{aq},0}_{\mathrm{MeX}} + RT\ln\left(a^{\mathrm{aq}}_{\mathrm{Me}^{z+},\mathrm{eq}} a^{\mathrm{aq}}_{\mathrm{X}^{z-},\mathrm{eq}}\right)\right)$$

$$= RT\ln\left(\frac{a^{\mathrm{aq}}_{\mathrm{Me}^{z+}} a^{\mathrm{aq}}_{\mathrm{X}^{z-}}}{a^{\mathrm{aq}}_{\mathrm{Me}^{z+},\mathrm{eq}} a^{\mathrm{aq}}_{\mathrm{X}^{z-},\mathrm{eq}}}\right) = RT\ln\left(\frac{a^{\mathrm{aq}}_{\mathrm{Me}^{z+}} a^{\mathrm{aq}}_{\mathrm{X}^{z-}}}{K_{\mathrm{sp}}}\right), \tag{6}$$

where R is the universal gas constant, T is the temperature, a_i^{aq} denotes the activity of species i in the aqueous phase and the subscript eq refers to the equilibrium activity of the species at specified T and p. Note that the value for the solubility product K_{sp} is for the given T and p. If one wishes to use some standard state K_{sp} value, one should correct for the possible difference in temperature, and also for pressure as given by[26]

$$\Delta\mu = RT\ln\left(\frac{a^{\mathrm{aq}}_{\mathrm{Me}^{z+}} a^{\mathrm{aq}}_{\mathrm{X}^{z-}}}{K^{\mathrm{ref}}_{\mathrm{sp}}}\right) + \int_{p_{\mathrm{ref}}}^{p} \left(V^{\mathrm{aq}}_{\mathrm{MeX}} - V^{s}_{\mathrm{MeX}}\right)\mathrm{d}p, \tag{7}$$

where $V^{\mathrm{aq}}_{\mathrm{MeX}}$ and $V^{\mathrm{s}}_{\mathrm{MeX}}$ are the partial molar volumes of the solute and the solid at given T, ref denotes the reference state used, at which $K^{\mathrm{ref}}_{\mathrm{sp}}$ is determined. The pressure contribution is often quite negligible and is usually ignored.[27] The activity ratio in Eq. (6) is called the supersaturation ratio. Several different forms for the supersaturation ratio can be found in the literature such as those given by Eqs. (8)–(10).[2, 28, 29] The supersaturation ratio is often denoted with S, but here S_{sat} will be used to avoid confusion with entropy.

$$S_{\mathrm{sat}} = \frac{a^{\mathrm{aq}}_{\mathrm{Me}^{z+}} a^{\mathrm{aq}}_{\mathrm{X}^{z-}}}{K_{\mathrm{sp}}}, \tag{8}$$

$$S_{\mathrm{sat}} = \left(\frac{a^{\nu_+ \mathrm{aq}}_{\mathrm{Me}^{z+}} a^{\nu_- \mathrm{aq}}_{\mathrm{X}^{z-}}}{K_{\mathrm{sp}}}\right)^{1/\nu} = \frac{a^{\mathrm{aq}}_{\pm}}{\sqrt[\nu]{K_{\mathrm{sp}}}}, \qquad \nu = \nu_+ + \nu_- \tag{9}$$

$$S_{\mathrm{sat}} = \frac{c_{\mathrm{MeX}}}{c_{\mathrm{MeX,eq}}}, \tag{10}$$

where ν^+ and ν^- are the stoichiometric numbers of cations and anions released when the salt dissociates, respectively, $a^{\mathrm{aq}}_{\pm}$ is the mean ionic activity of the solute and c_{MeX} is the concentration of the solute MeX on a molar basis. Eq. (10) naturally assumes the solution to be ideal and activities should be used in calculating the saturation ratio whenever possible. Ignoring

nonideality may lead to severe errors as is clearly illustrated in a paper by Schwarzer and Peukert (2004).[30] Supersaturation is probably the most important single variable controlling the precipitation process since it affects the rates of almost all possible subprocesses as will be seen in later.

Even though supersaturation is required for precipitation to take place, it does not necessarily indicate that it happens spontaneously. It is possible, that the species remain in solution even though the solution is supersaturated, that is, the solution is metastable. All solutions have a *metastable limit* which is the maximum allowable supersaturation at which the precipitate does not form spontaneously. The zone between the solubility curve and the metastable limit is called the metastable zone. In practical applications, the metastable zone is often quite narrow, since actual solutions always contain some impurities or solid particles which promote secondary- and heterogenous nucleation, processes for which the energy barrier to overcome is much smaller than for the formation of nuclei from the homogenous solution phase.[31]

2.2. Classical Crystallization Theory

The formation of crystals is traditionally explained by two distinct mechanisms. The first is *nucleation*, which deals with the formation of imperceptibly tiny nuclei that act as precursors for the actual solid phase. As soon as these nuclei form, they begin to grow into larger crystals eventually observable by bare eye. In the classical crystallization theory, the process of crystal growth is divided into two parts, which are the mass transfer of the so-called *growth units* from the bulk solution to the crystal-liquid interface and the incorporation of these units to the crystal which is referred to as the surface integration step.[2]

The classical description of nucleation states that nuclei in supersaturated solutions form due to random microscopic density fluctuations that bring the solute molecules closer to each other.[32] If the nucleus size is below the critical size, the surface energy required to keep the molecules in the nucleus together is greater than the free energy decrease gained in the phase transformation and the nucleus spontaneously dissociates. If the critical size is reached, the energy advantage gained by the formation of the new phase outweighs the loss due to the surface energy and the nucleus will start grow spontaneously as is illustrated in Figure 3.[32]

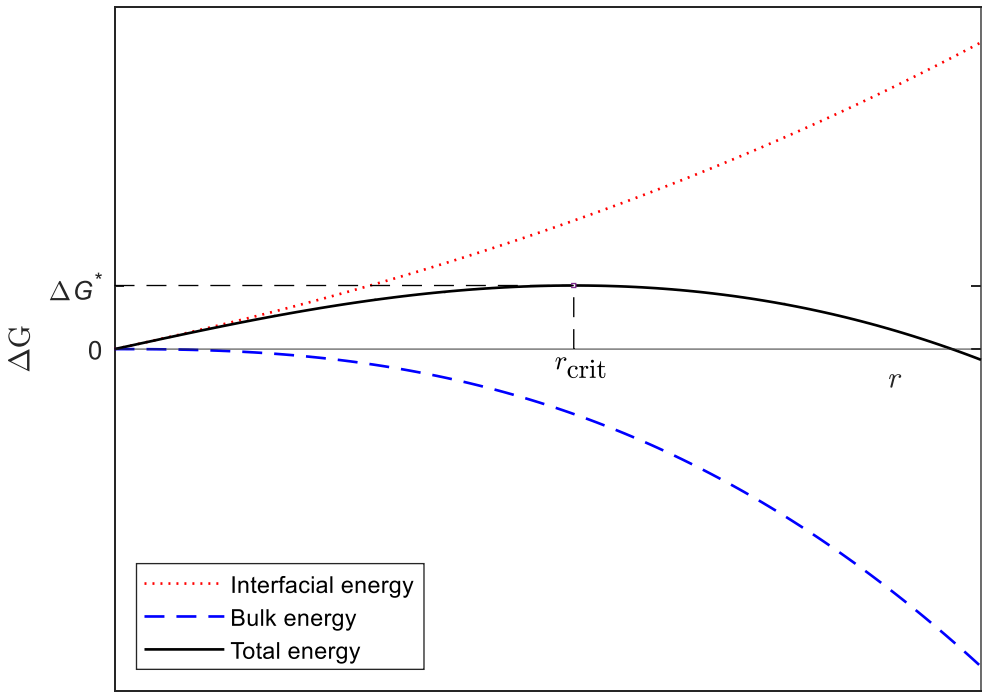

Figure 3. Illustration of the classical description of nucleation. ΔG^* represents an energy barrier that must be overcome for spontaneous nucleation to occur.

Mathematical expressions for the rates of nucleation and crystal growth can be obtained by combining simple semi-empirical and empirical rate laws written for the individual steps. Without going into details, for example the following empirical expressions for homogenous nucleation and crystal growth rates, $J\ (1/\mathrm{s})$ and $G_\mathrm{r}\ (\mathrm{m/s})$ can be derived:[2, 31]

$$J = \frac{D}{d_\mathrm{m}^5 N^*}\left(\frac{4\Delta G^*}{3\pi kT}\right)^{1/2} \exp\left[\frac{-16\pi\sigma^3 {\nu_\mathrm{m}}^2}{3k^3T^3(v\ln S_\mathrm{sat})^2}\right] = \Omega \exp\left[\frac{B}{(v\ln S_\mathrm{sat})^2}\right], \tag{11}$$

$$G_\mathrm{r} = \frac{k_i(a - a_\mathrm{eq})}{1 + (\rho k_i/4D)L}, \tag{12}$$

where D is the diffusion constant of the solute in the medium, d_m is the molecular-, or ionic diameter, N^* is the number of molecules or ions in a single nucleus of critical size. ΔG^* is the Gibbs energy change required to form a crystal of a critical size from the solution, k is the Boltzmann constant, σ is the surface energy, ν_m is the molecular volume, k_i is an empirical

"lumped parameter" constant, ρ is the crystal density, a is the solute activity in the bulk solution, a_{eq} is the equilibrium activity of the solute at given conditions, and L is the particle size (e.g. diameter). Parameters Ω and B contain the constants on the left-hand side of Eq. (11) lumped together. Note that in Eq. (11) all other variables than S_{sat} are considered constant. Eq. (12) is based on Fick's laws of diffusion and on the assumption that the surface integration is first order in terms of solute concentration.[2] Eq. (12) is only one of numerous expressions used for the growth rate that can be found in the literature.[2, 28, 30, 31]

The Gibbs free energy ΔG^* required for the formation of a single spherical nucleus of critical size can be estimated from:[2]

$$\Delta G^* = \frac{16\pi\sigma^3 {\nu_{\mathrm{m}}}^2}{3k^2T^2(\nu \ln S_{\mathrm{sat}})^2}. \tag{13}$$

However, the surface energy σ and the solubility product required to calculate S_{sat} are poorly defined quantities for microscopic nuclei, whose properties can be expected to differ greatly from those of macroscopic crystals.[32] Thus, only rough estimates of the possible magnitude of ΔG^* can be made using Eq. (13). By assuming that the radius of a single ZnS unit in a nucleus is about 0.259 nm (the average of ionic diameters of Zn^{2+} and S^{2-})[33], and by using a value $\sigma = 0.65\ \mathrm{J/m^2}$, which is the surface energy for the lowest energy surface of solid sphalerite[34], an estimate of $\Delta G^* \approx 7 \cdot 10^{-17}$ J is obtained for $T = 298.15$ K and $S_{\mathrm{sat}} = 10$ as defined by Eq. (9). It should be noted that this value is highly unreliable due to the reasons mentioned above and is meant only to provide some perception about the possible magnitude of this energy barrier. The estimated value is somewhat larger than the experimentally determined value 10^{-19} J, for the nucleation of lysozyme crystals under similar conditions.[35] This difference is mainly due to the greater surface energy term used for sphalerite.

A more usual type of nucleation than homogenous nucleation is heterogenous nucleation, in which the nuclei form on the surfaces of particles already present in the solution. These foreign surfaces have a catalytic effect on nucleation since the energy barrier ΔG^* for nucleation on such external surfaces is much lower than for homogenous nucleation. Nucleation induced by already formed particles of the precipitating material is called secondary nucleation which is further divided into three sub-categories: apparent, true, and contact. Apparent secondary nucleation is a mechanism, in which tiny fragments are washed off the seed crystals which may act as new nuclei. In true secondary nucleation, the presence of seed crystals lowers the critical size

required for a nucleus to be stable by promoting favorable sites for nucleation as in heterogenous nucleation. Contact secondary nucleation is caused by collisions of crystals with reactor walls, impellers, or another crystal. Secondary nucleation is generally not significant in precipitation processes of insoluble salts since high supersaturation promotes the primary nucleation mechanism and results in crystals of small particle size. Collisions of small particles with the equipment or each other are low in energy and thus, do not readily cause contact secondary nucleation.[2, 28]

2.2.1. Gibbs-Thomson Effect and Ostwald Ripening

The Gibbs energy change when solid crystals of MeX are in equilibrium with the liquid phase at constant T and p is given by[25]

$$\Delta G = \mu_{\mathrm{MeX}}^{\mathrm{aq}} \mathrm{d}n_{\mathrm{MeX}}^{\mathrm{aq}} + \mu_{\mathrm{MeX}}^{\mathrm{s}} \mathrm{d}n_{\mathrm{MeX}}^{\mathrm{s}} + \sigma \mathrm{d}A = 0, \tag{14}$$

where $n_{\mathrm{MeX}}^{\mathrm{aq}}$ and $n_{\mathrm{MeX}}^{\mathrm{s}}$ are the number moles of MeX in the solution and solid phases, respectively, and $\sigma \mathrm{d}A$ is an excess term (surface energy) compensating for the difference in the chemical potentials of an infinite solid phase and a finite crystal. For spherical crystals $n_{\mathrm{MeX}}^{\mathrm{s}} = 4\pi r^3 / 3V_{\mathrm{m}}^{\mathrm{s}}$, where $V_{\mathrm{m}}^{\mathrm{s}}$ is the molar volume of the solid. By recognizing that for a closed system $n_{\mathrm{MeX}}^{\mathrm{aq}} + n_{\mathrm{MeX}}^{\mathrm{s}} = \mathrm{constant}$, using the result from Eq. (6) for the differences in chemical potential and rearranging Eq. (14), the Gibbs-Thomson equation for spherical crystals can be derived:[2, 25]

$$v \ln \frac{a_{\pm,\mathrm{eq}}(r)}{a_{\pm,\mathrm{eq}}(\infty)} = \frac{2\sigma V_{\mathrm{m}}^{\mathrm{s}}}{RTr}, \tag{15}$$

where, v is the stoichiometric number of ions produced when the salt dissociates, $a_{\pm,\mathrm{eq}}(\infty)$ is the mean ionic activity of the solute in equilibrium with an infinitely large crystal, and $a_{\pm,\mathrm{eq}}(r)$ that of a crystal with radius r. Eq. (15) tells us that the solubility of small crystals is greater than that of large crystals. The physical interpretation of this result is that the contribution of the surface energy associated with the liquid-solid interface to the system's Gibbs energy becomes larger with decreasing crystal size (see Fig. 3). Thus, it can also be deduced that larger crystals will preferentially form while smaller crystals tend to dissolve so that the system's overall Gibbs energy decreases. This phenomenon is often referred to as Ostwald ripening.[2]

2.2.2. Particle Size Distribution and Population Balance

As might be expected from the preceding discussion, the particle size of the precipitates is strongly affected by the supersaturation conditions. At high supersaturation, nucleation rate becomes high, and large numbers of tiny particles form. Naturally, the particles formed will not be of equal size, but the crystal sizes will follow a certain particle size distribution (PSD) instead. Knowing how to predict and control the PSD is often of considerable interest because the particle size affects later unit operations, such as filtration and sedimentation. For this purpose, the equations for the rates of nucleation and growth rate can be used together with the population balance approach developed by Randolph and Larson[36] and a mass balance equation to obtain models for the particle size distribution. The general equation for the population balance from an Eulerian viewpoint is given by:[37]

$$\frac{\delta n}{\delta t} + \nabla \cdot \overline{v_i} n + n \frac{\mathrm{d}(\log V)}{\mathrm{d}t} = B - D - \sum_k \frac{\dot{V}_k n_k}{V}, \tag{16}$$

where n is the population density, t is time, $\overline{v_i}$ is the velocity vector along an internal coordinate (such as the linear growth rate G_r), V is the system volume, B and D are the birth and death functions (are used to include effects such as aggregation and breakage), $\dot{V}_k$ is the volumetric flow rate across the system boundary k. Considering a MSMPR-reactor operating in steady state, and assuming that crystals are formed only through homogenous nucleation and increase in size only by size-independent growth, there are no crystals in the feed, attrition, aggregation and breakage are negligible and that the particle shape factors are not influenced by the particle size, Eq. (16) reduces to[37]

$$\frac{\mathrm{d}n}{\mathrm{d}L} = -\frac{n}{G_\mathrm{r}\tau}, \tag{17}$$

where $\tau = V/\dot{V}$ is the retention time. Eq. (17) is a linear first order ordinary differential equation that can be readily solved. After separating the variables and imposing the initial condition $n(0) = n^0$ the following result is obtained:

$$n = n^0 \exp\left(\frac{-L}{G_\mathrm{r}\tau}\right), \tag{18}$$

where n^0 is the number density of "zero-sized" particles (or nuclei). This equation enables us to calculate the nucleation and growth rates if the PSD is known, or the other way around, estimate the PSD if nucleation and growth rates are known or modelled.[37] The assumptions made in obtaining Eq. (18) are quite unrealistic, and more accurate treatment will require much more complicated measures, although the basic principle remains the same. Models utilizing the population balance have been successfully applied to many precipitation processes.[2, 38, 39]

2.2.3. Shortcomings of the Classical Crystallization Theory

Especially for precipitation processes with high supersaturation levels, the classical crystallization theory is often not sufficient to explain the crystal morphology or growth rates observed experimentally, and other mechanisms must be taken into consideration. Often quite large deviations between the predicted and observed nucleation rates are obtained when using the classical approach.[31, 40]

A notable shortcoming of the classical approach on nucleation is the involvement of surface energy σ in Eq. (11), the main problem being the lack of means for quantifying σ for typical nanometer-scale nuclei.[32] Also, the bulk structure of the nuclei may be significantly different from that of larger crystals, which can make the definition of a representative solubility product for calculating the supersaturation ratio needed in Eq. (11) difficult.[32] For example, there may be some amorphous intermediate phase that dominates at the early stages of nucleation as has been observed to be the case in calcium carbonate precipitation.[41]

Recent experimental findings have also shown that highly dynamic solute aggregates, called pre-nucleation clusters (PNCs) can be stable also in the homogenous regions of phase diagrams (in which phase separations are thermodynamically impossible) and can act as precursor nuclei for the formation of the solid phase. This is in contradiction with the classical crystallization theory, which states that nuclei formation requires some phase separation to take place. More details and an extensive introduction on this topic can be found in the review by Gebauer et al. (2014).[32]

According to the classical approach, crystal growth proceeds only via the incorporation of growth units to existing crystals and is thus governed by mass transfer through the interfacial layer and/or some rather simple surface integration reaction.[31] During the last few decades, new theories have emerged suggesting that crystal growth may in some instances be governed by

processes, in which small nanocrystals aggregate to form larger micron-sized crystals.[42] These mechanisms have been proposed to be likely especially when nucleation is favorable as in solutions of high supersaturation. This is because a sufficient density of primary nanoparticles required for the aggregative growth to take place, can only be provided by a high nucleation rate. The nanoparticle aggregation mechanisms have been proposed to explain polycrystallinity and crystal morphologies deviating from the equilibrium morphology, but classical growth occurring under conditions far from equilibrium can also explain these features. However, the kinetics of these alternative routes are substantially different which is why the correct identification of the actual mechanism is vital. Unfortunately, the understanding of the nanoscale aggregation processes is not currently on a level that accurate predictive models would be realizable.[42]

2.3. Particle Surface Properties

In the preceding discussion we have already needed the concept of surface energy to explain why supersaturated metastable solutions do exist, and why larger crystals are thermodynamically more stable (less soluble) than smaller ones. This gives us some indication, that the chemistry of surfaces plays an important role in precipitation processes, which is indeed the case. In this section some aspects of the thermodynamics and the chemistry of surfaces important from the viewpoint of precipitation processes are briefly discussed. There are several textbooks available that cover the topic extensively and should be consulted for further information.[43-45]

2.3.1. Thermodynamics of Surfaces and the Surface Energy

The thermodynamic treatment of interfaces is greatly simplified by introducing the so-called surface excess quantities. This treatment was originally developed by Gibbs, and it is based on an imaginary model system consisting of two phases of uniform composition separated by an infinitesimally narrow interfacial region.[43] Any extensive thermodynamic property of the system, such as U, G, S or H, can be divided between these three parts. For example, if B denotes some arbitrary extensive thermodynamic property and b is the intensive counterpart of this same property, then the value of B associated with the surface, B^{σ}, is given by[43, 45]

$$B^{\sigma} = B^{\mathrm{sys}} - b^{\alpha}V^{\alpha} - b^{\beta}V^{\beta}, \quad V^{\alpha} + V^{\beta} = V^{\mathrm{sys}}, \tag{19}$$

where B^{sys} is the value of B associated with the entire system and $V^{\alpha}$and V^{β} are the volumes of phases α and β. This kind of treatment greatly simplifies the thermodynamic description of the surfaces since the actual dimensions of the interfacial region or the spatial distributions of the properties in the interface do not need to be known. The position of the imaginary interface must, however, be specified, and it is often convenient to set the surface so that the surface excess amount of the solvent in the interface is zero ($n^{\sigma}_{\mathrm{solvent}} = 0$).[43]

The surface energy, σ, is defined as the work per unit area required to increase the interfacial area as given by[43]

$$\sigma = \frac{\delta \mathrm{W}}{\delta A}, \tag{20}$$

where δW is the work required to increase the area of the interfacial region by δA. For a pure liquid in equilibrium with a pure gas- or another pure immiscible liquid phase, the surface tension, which is the force per unit length required to increase the interfacial area, is equal to the surface energy. However, for solids this is often not the case, because the immobility of the atoms in a solid prevent the crystal from reaching the equilibrium shape (the changes in surface area are not reversible). Thus, the physical interpretation of surface energy for solids is not as straightforward than for liquids.[43, 45]

However, when crystals are growing from a solution in a reversible manner, which at least in principle can be achieved in crystallization processes, the surface energy plays a central role in determining the shape of the resulting crystal. A crystal that is grown reversibly will adopt a shape for which the surface energy is minimal. It can be shown that for a three-dimensional crystal with six faces (opposing faces being similar) that has obtained its equilibrium shape, the following relation holds:[43]

$$\frac{\sigma_1}{r_1} = \frac{\sigma_3}{r_3} = \frac{\sigma_3}{r_3} = \mathrm{constant}, \tag{21}$$

where σ_i is the surface energy of the face perpendicular to r_i which is the distance from the center of the crystal to the corresponding face. Eq. (21) tells us that faces with high surface

energy will tend to be further away from the center which means that such faces will have the smallest area as can be easily verified by geometric considerations.[43]

2.3.2. Electrical Double Layer

In liquid-solid dispersions, there typically is an accumulation of charge on the surfaces of the solid particles. This charge may develop through several mechanisms, which include for example, surface dissociation, adsorption of ionic species from the solution phase, crystal defects, or in the case of ionic solids there may be a slight imbalance in the number of anions and cations on the surface of the crystal.[43]

In the case of metal sulfides, which are ionic sparingly soluble solids, the concentrations of the metal- and sulfide ions in the aqueous phase influence the balance of the numbers of ions on the interface and thus the surface charge of the particles.[43, 46] The surface charge can also be strongly dependent on pH. A common reason for this behavior is that the surfaces of the particles possess functional groups that can react with H^+ and OH^- ions.[43] Regardless of the mechanism behind the generation of surface charges, these generally exist, and they can explain a lot about the behavior of colloidal particles dispersed in solution. Colloidal dispersions are important for our discussion since great numbers of colloidal particles are typically formed in precipitation processes due to the high supersaturation levels.

Due to the surface charges possessed by most solid particles immersed in a solution, an electric field around the solid particle develops and consequently, counterions of the opposite charge accumulate to the vicinity of the particle to preserve electroneutrality. However, the counterions in the solution phase are not strongly bound to the solid particles but can experience diffusion. These interactions lead to the development of the *electrical double layer*, which is illustrated in Figure 4.[43-45, 47]

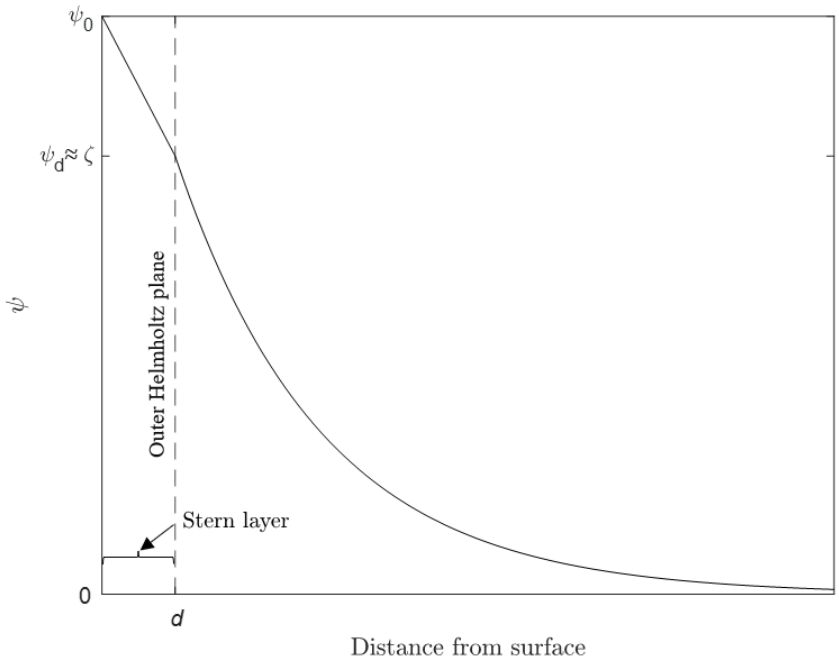

Figure 4. The behavior of the electric potential as a function of distance from a planar surface with a positive potential ψ_0 according to the Stern model. ψ_d denotes the potential at the beginning of the diffuse layer, which is nearly equal to the zeta-potential ζ. d can be thought as the thickness of the first adsorbed layer. See text for more details.

Probably the most widely known description of the electrical double layer is given by the Stern model, which is basically a simple extension of another well-established model, the Gouy-Chapman theory. The Stern model states that the ions closest to the surface are strongly bound to it and the potential drop in this Stern layer behaves differently from that in the diffuse region further away from the surface.[45] The Stern layer can be divided further to inner- and outer Helmholtz layers, which may be necessary if pure electrostatic interactions are not the only type of interactions involved in the adsorption.[47] The Gouy-Chapman model is used to describe the potential drop across the diffuse layer. The model assumes that the concentration of oppositely charged ions as a function of the distance from the surface follows Boltzmann distribution. From this and from electrostatic considerations, the Poisson-Boltzmann equation that describes how the electric potential drops as a function of distance from the surface can be derived:[43]

$$\nabla^2\psi(r) = \frac{-1}{\epsilon_0\epsilon_r}\sum_i \left[n_i^0 z_i e \exp\left(\frac{-z_i e\psi(r)}{kT}\right)\right], \tag{22}$$

where $\psi(r)$ is the electrical potential as a function of radius, n_i^0 is the bulk concentration of ions of type i, z_i the charge of ions of type i, e is the elementary charge, k is the Boltzmann constant, ϵ_0 is permittivity of vacuum and ϵ_r is the relative permittivity of the bulk phase. Note that in the Stern model Eq. (22) applies only when $r > d$ (see Fig. 4). A separate model is needed for the potential drop across the Stern layer. Several models for these purposes have been proposed, but these are beyond the scope of this discussion.[43]

By making the so-called Debye-Hückel approximation, which states that $|z_i e\psi(r)| \ll kT$ (i.e. thermal energy possessed by the ions is considerably larger than the electrical energy), Eq. (22) can be greatly simplified to yield[43, 45]

$$\nabla^2\psi(r) = \left[\frac{\sum_i z_i^2 n_i^0 e^2}{\epsilon_0 \epsilon_r kT}\right]\psi(r) = \kappa^2\psi(r), \tag{23}$$

where the constant κ is called the Debye-Hückel parameter. The reciprocal of this parameter is referred to as the Debye length and is often thought as a measure of the thickness of the double layer. Solving Eq. (23) with physically meaningful boundary conditions, e.g. $\psi(0) = \psi_d$ and $\lim_{r\to\infty} \psi(r) = 0$, yields

$$\psi(r) = \psi_\mathrm{d} \exp(-\kappa r), \tag{24}$$

where r is the distance from the outer edge of the Stern layer and ψ_d is the potential at the edge of the Stern layer. This potential is almost equal to the zeta-potential ζ, that is used extensively in literature dealing with colloidal dispersions.[43] The zeta-potential is defined as the potential at the plane at which the velocity of the fluid is zero[43, 47] (the hydrodynamic slip plane). The conditions at which the ζ-potential becomes zero, is called the isoelectric point (IEP). The ζ-potential is a convenient measure of the surface charge since it can be quite readily measured for example, by electrophoretic techniques although these determinations are not completely free of problems, especially when accurate values are needed.[47] It should also be noted that the Debye-Hückel approximation and thus Eq. (24), are not applicable to many practical situations, where $|\psi_d| > 25$ mV.[45] In these cases, the complete Poisson-Boltzmann equation as given by Eq. (22) must be solved.

2.3.3. Particle Crowding Effect

It has been observed that crystal growth rates can be higher than expected for systems, in which the number density of particles is very high as is the case with many precipitation systems.[2] This effect has been attributed to the small interparticle distance between the particles, which causes the diffusion layers around individual crystals to overlap. The overlap gives rise to higher concentration gradients within the diffusion layers, which leads to faster mass-transfer and consequently, to faster growth rates.[48] The effect has been proposed to become important when the interparticle distance becomes smaller than 20 particle diameters.[2]

2.3.4. Aggregation

The term aggregation generally refers to phenomena, in which individual particles interact to form new, larger particles. According to the IUPAC recommendation[49], the term *agglomeration* should be used for reversible processes only and can be used interchangeably with *flocculation* or *coagulation* whereas aggregation is a general term. We have already seen in chapter 2.2.2 that the aggregation phenomena must be often considered in PSD modelling. These phenomena can generally have a profound effect on the particle size distribution and the settling properties of the precipitates which can be of great importance in industrial precipitation.[2]

The surface charges of small particles can keep them apart from each other through Coulombic repulsion and thus prevent aggregation from occurring. The stabilizing effect of the surface charges is called electrostatic stabilization. Another possible reason causing repulsive forces between individual particles are large macromolecular adsorbents that adhere to the surfaces of the particles and prevent close approach with other particles through steric interactions. This phenomenon is called steric stabilization.[2]

The energy required for two approaching particles to overcome the repulsive interactions between them can be viewed in a somewhat analogous manner as the activation energy of a chemical reaction. If this energy barrier is overcome when two particles collide, aggregation will take place through van der Waals interactions. The situation is however different in a sense that the distances involved are much longer (about 1–100 nm) than with chemical reactions and that the interactions between the particles and the solvent molecules play a significant role during this approach. Particles possessing enough kinetic energy to overcome the energy barrier would thus dissipate this energy through frictional interactions with the solvent much before the

particles would come into contact. The appropriate way to describe the situation is to think that the existence of the energy barrier increases the probability of such diffusion steps that take the particles further apart. Thus, the larger the energy barrier, the more unlikely it is that the two particles ever come into contact. The concepts of interaction between colloidal particles in dispersion were elaborated and constructed into a formal theory by Deryaguin, Landau, Verwey and Overbeek, which is commonly referred to as the DLVO theory.[50, 51] The basis of the theory is that the potential energy as a function of the distance between two particles can be expressed as the superposition of the potential energy curves resulting from Coulombic repulsion and van der Waals attraction.[43]

The kinetics of aggregation phenomena is generally quite complicated, but mathematical descriptions are available which are mainly based on the DLVO theory, although the mathematical descriptions for agglomeration rates with the absence of any energy barriers were derived long before the establishment of the DLVO theory. Unfortunately, there is no room for a detailed discussion of the subject in this thesis, but more information can be found in many textbooks such as those used as the basis of this text.[43-45]

2.4. Speciation of Metals in Sulfidic Solutions

It has been long known that especially under oxidizing and alkaline conditions, sulfides in aqueous media can form larger polysulfide species in addition to the bisulfide (HS^-) and sulfoxide ($SO_3^{2-}, SO_4^{2-}, S_2O_3^{2-}$ etc.) ions.[52] Polysulfides are not thermodynamically stable under ambient conditions and eventually disproportionate to yield sulfoxides and HS^- or are oxidized directly to sulfoxides.[53] These reactions are, however, extremely slow and may take even about a year to proceed to completion.[10, 53] The speciation of polysulfides is governed by the activities of HS^-, OH^- and dissolved zerovalent sulfur S^0 (a virtual species[54]) as suggested by Eqs. (25)–(26).[10, 52]

$$nS^0(aq) + HS^-(aq) \rightleftharpoons S_nS^{2-}(aq) + H^+(aq) \quad (25)$$

$$(n-1)S_nS^{2-}(aq) + HS^-(aq) + OH^-(aq) \rightleftharpoons nS_{n-1}S^{2-}(aq) + H_2O(l) \quad (26)$$

Equilibrium constants for reactions of type (26) are available at least for compounds for which n is up to 5.[55] Theoretical considerations and experimental observations have, however,

suggested the existence of polysulfides with $n > 5$.[53, 55] The thermodynamic data that is available for the polysulfides shows some disagreement between various sources especially for species with low stabilities such as S_2^{2-}, S_3^{2-} ($n = 3$ and $n = 4$).[55]

Figure 5 shows three different Eh – pH diagrams for the S-H_2O system drawn with the EpH module of the HSC Chemistry® 10 process modelling platform developed by Outotec®.[56] Fig 5 a) includes all the important sulfur species and b) all species but those containing S(VI) such as SO_4^{2-}, which is the thermodynamically stable form of sulfur in aqueous solutions under typical ambient conditions.[53] Fig 5 c) illustrates the regions of predominance for each of the polysulfide-ions with sulfoxide species completely excluded from the calculations. The exclusion of sulfoxides is feasible due to the slow kinetics of the disproportionation and oxidation reactions as noted earlier.[53] Thus, the latter two figures correspond to metastable situations. Fig. 6 shows the abundances of various polysulfide species as a function of pH in a system with a unit activity of zerovalent sulfur. It is worth noting, that there is practically always some uncertainty in the thermodynamic data behind figures such as Figs. 5 and 6 and they should thus be viewed with some caution. This will be discussed later in more detail.

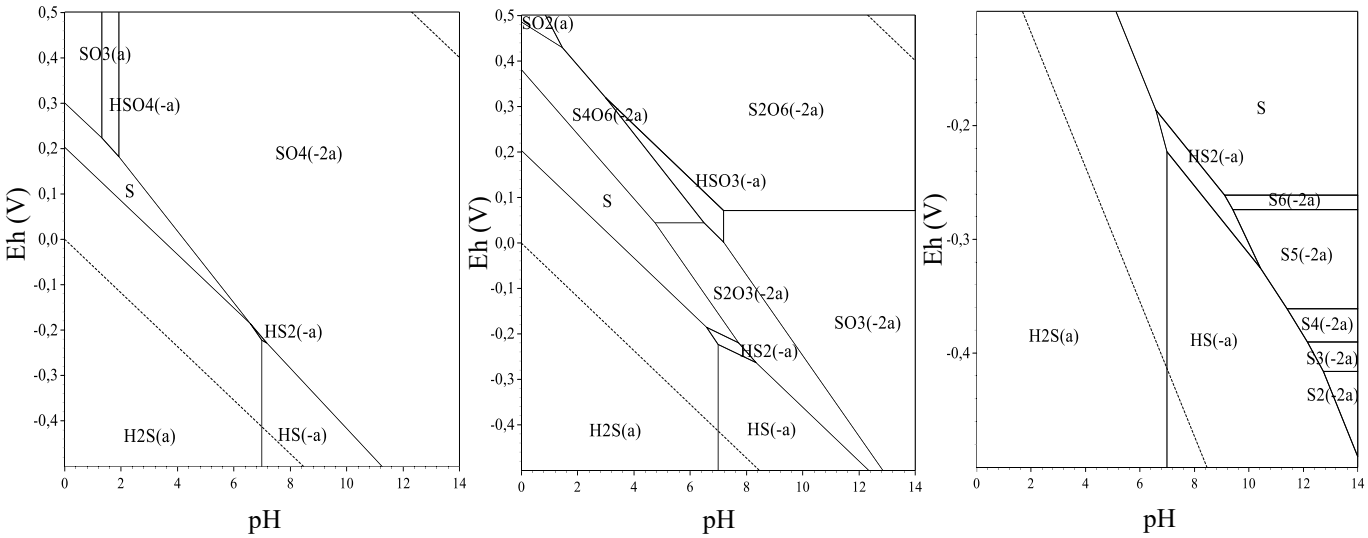

Figure 5. The Eh – pH diagrams of the S-H_2O system at $T = 298$ K, $p = 0.1$ MPa and total sulfur molality of 0.01 mol/kg. a) All sulfur species listed in appendix A included, b) S(VI) species excluded and c) all sulfoxide species excluded.

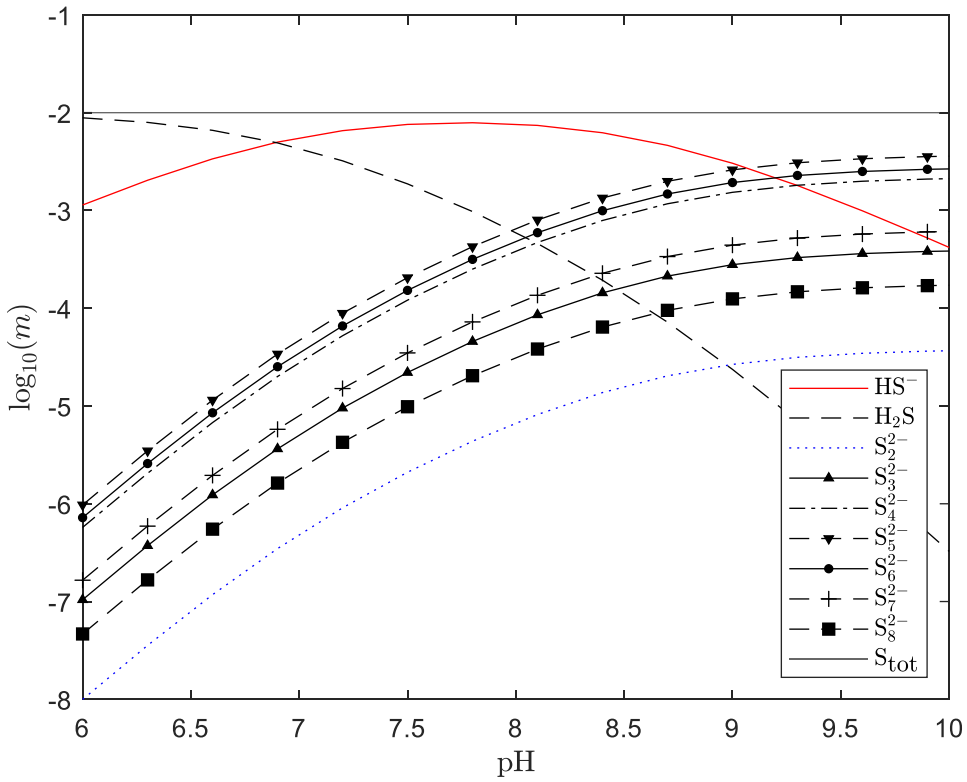

Figure 6. Speciation of polysulfides as a function of pH at $I = 0.3$ mol/kg, activity of zerovalent sulfur $a_{S^0} = 1$, and total amount of sulfide $m_{S(-II),tot} = 10^{-2}$ mol/kg. Calculated using the stability constants from Kamyshny et al. (2004)[55] and estimating the activity coefficients with the Davies equation [Eq. (30)].

Although much research has been done on aqueous sulfide solutions, there are relatively few studies that treat metal polysulfide complexes in detail, but they have nevertheless been proven to exist and studied.[10, 57, 58] Some experimentally determined stability constants at 25 °C for the tetra- and pentasulfide complexes of Fe, Mn, Co, Ni measured in relatively dilute NaCl and Na_2SO_4 solutions can be found in a paper by Chadwell et al. (1999)[57]. They also found that Cu and Zn form particularly stable tetra- and pentasulfide complexes and estimates of the stability constants for these complexes have been given in their papers.[57, 58]

As with most detailed studies of metal sulfide complexes, these investigations have been carried out in very dilute (1–10 μM) solutions with respect to the reactants and thus the information may not be that readily extended to industrial precipitation systems with much higher concentrations of the relevant species.[3] The general lack of integration between sulfide precipitation studies and the more fundamental speciation studies mentioned for example by

Lewis (2010),[3] results probably at least partly from the fact that most of the these fundamental studies have been originally motivated by the need to explain unexpectedly high solubilities of metal sulfides in naturally occurring systems that are encountered in geo- and biochemical processes.[10, 59, 60] As is easily realized, the conditions and the timescales of these processes are typically quite different from those observed in industrial processes.

In addition to polysulfides, many metals also form soluble complexes or molecular clusters with bisulfide ions directly.[10, 61-63] These complexes have been suggested to play a vital part as intermediates in the formation of the solid metal sulfide precipitates.[62] In systems where polysulfides are present in significant amounts, the polysulfide complexes are likely to be formed preferentially over the bisulfide complexes as indicated by the stability constants reported by e.g., Chadwell et al. (1999)[57] and Shea and Helz (1988)[10].

Despite of the indisputable advances in understanding metal sulfide speciation brought about by these research efforts, there still remains some major discrepancies in the field. For example, some authors have proposed that soluble FeS clusters can explain the solubility of $FeS(s)$ in solutions and that Fe^{2+}does not form bisulfide complexes to any significant extent[61, 64] whereas Davison et al. (1999)[65] found that the formation of such clusters was inconsistent with their observations and instead, suggested that complexes of the type $Fe_x(HS)_{2x}$ are responsible for the observed solubility behavior of $FeS(s)$. These contradicting observations are reflected to poor agreement between literature values for the solubility product of amorphous $FeS(s)$ which span over a pK_{sp} range of about 2.9–3.9 reported at 20–25 °C.[64]

3. THERMODYNAMICS OF SULFIDE PRECIPITATION

3.1. Solubilities of Metal Sulfides

The solubility of a salt is in principle, determined by its thermodynamic solubility constant given for a reaction of the type:

$$\mathrm{Me}_{v_+}\mathrm{X}_{v_-}(\mathrm{s}) \rightleftharpoons v_+\mathrm{Me}^{z+}(\mathrm{aq}) + v_-\mathrm{X}^{z-}(\mathrm{aq}), \qquad K_{\mathrm{sp}} = a_{\mathrm{Me}^{z+}}^{v_+} a_{\mathrm{X}^{z-}}^{v_-} = \gamma_{\pm}^{v} m_{\mathrm{Me}^{z+}}^{v_+} m_{\mathrm{X}^{z-}}^{v_-}, \qquad (27)$$

where $\gamma_{\pm}$ is the mean molal activity coefficient of the electrolyte and m_i is the molality of ion i. In reality, ions released from the dissociation of the salt can react further which causes more solid to dissolve to maintain the equilibrium. In the case of metal sulfides, the complex formation reactions discussed in the preceding section are examples of this kind of solubility controlling side reactions. Of course, it should be remembered that the equilibrium constants for these various reactions are temperature and pressure dependent. Also, recall from section 2.2.1 that the particle size of the solid affects the thermodynamic solubility product through surface energy effects. Different solid phases of the same elemental composition have different lattice energies and will consequently have differing solubilities. Further complications arise from the fact, that the activity coefficients that relate the actual concentrations of the species to their activities are strongly dependent on temperature, pressure, ionic strength, and the properties of the solvent. The activity coefficients can be estimated with a reasonable accuracy for dilute solutions (with $I < 1\ \mathrm{mol\ kg^{-1}}$) by using the extended semi-empirical forms of the Debye-Hückel limiting law. Modeling the activity coefficients becomes increasingly difficult with higher ionic strengths and with higher number of components as the solute-solute and solute-solvent interactions become increasingly important.[33, 66]

These considerations imply that the solubility of any sparingly soluble salt is a complicated issue and that the prediction of solubilities for a real multicomponent system with high ionic strength is difficult. For metal sulfides, the situation is further complicated by the rather complex chemistry of polysulfides and the lack of consensus on the actual metal sulfide species existing even in dilute solutions as was discussed earlier.

Table 1. shows some literature values for the $\mathrm{p}K_{\mathrm{sp}}$ values of selected metal sulfides. Note that these values have been given for the reaction of the following form:

$$\mathrm{Me}_x\mathrm{S}_y(\mathrm{s}) + y\mathrm{H}^+(\mathrm{aq}) \rightleftharpoons x\mathrm{Me}^{2(y/x)+}(\mathrm{aq}) + y\mathrm{HS}^-(\mathrm{aq}),$$

$$K_{\mathrm{sp}} = \frac{(a_{\mathrm{Me}^{2(y/x)+}})^x (a_{\mathrm{HS}^-})^y}{(a_{\mathrm{H}^+})^y}, \tag{28}$$

instead of Eq. (3) that is usually used for dissociation reactions of salts. The above form, and a related reaction involving $\mathrm{H_2S(aq)}$ have been used to define solubility products for metal sulfides for a few decades now to avoid the problems associated with the second dissociation constant of $\mathrm{H_2S}$.[67, 68] To make the comparison of the literature values easier, all $\mathrm{p}K_{\mathrm{sp}}$ values in table 1 have been converted to correspond to Eq. (28) if they were originally reported in some other form by using the value $\mathrm{p}K_{\mathrm{a1}} = 6.98$ for the reaction given by Eq. (1). From table 1 it is seen that there is a rather large disagreement between values from different sources, which is explained by the aforementioned difficulties in obtaining reliable experimental data. Table 1 is by no means a complete summary of literature values but is meant to provide some insight on the level of agreement between values from different sources. Also, no discrimination between the values presented here will be attempted, but it is generally advised that more recent values are preferred over the older ones if nothing suggests otherwise. Many more experimental solubility values reported in different forms and under varying conditions can be found in the literature.[69-73]

A rather thorough literature review on ZnS and CdS solubilities reported until 1992 has been compiled by Clever et al. (1992).[69] These authors also discuss the problems related to the determination of solubility products of sulfides in general. They highlight the fact that the systematically high solubility values that appear in older literature arise mainly from the poorly defined value of K_{a2} for the dissociation reaction of $\mathrm{H_2S}$. These authors recommended the values suggested by Licht (1988)[68] to be used as the best estimates for that time. They also note that the older values could be improved by recalculating the derived solubility product values using the original experimental results with present, more accurate thermodynamic data. The authors also note that in many older studies on CdS solubilities, the solid phase is often poorly characterized or just assumed to be greenockite although CdS can exist as a cubic (hawleyite) form also.

Table 1. Values of solubility products for selected metal sulfides.

Reaction	pK_{sp} (T=298.15 K, I = 0)	Phase	Source
$FeS(s) + H^+(aq) \rightleftharpoons Fe^{2+}(aq) + HS^-(aq)$	3.00	amorphous	Davison et al. (1999)[65]
	3.5	amorphous	Rickard (2006)[64]
	2.95	amorphous	Davison et al. (1991)[74]
	2.94	amorphous	Theberge & Luther (1997)[61]
	4.2	not specified	Myers (1986)[67]
	3.92	amorphous	Ball & Nordstrom (1991)[a, 75]
	3.83	amorphous[b]	Benning et al. (2000)[76]
	3.7	not specified	Licht (1988)[c, 68]
	5.1	pyrrhotite	Davison et al. (1991)[74]
	3.6	mackinawite	Davison et al. (1991)[74]
	3.8[d]	mackinawite	Lemire et al. (2013)[77]
	4.65	mackinawite	Ball & Nordstrom (1991)[a, 75]
$FeS_2(s) + 2H^+(aq) + 2e^- \rightleftharpoons Fe^{2+}(aq) + 2HS^-(aq)$	16.4	pyrite	Davison et al. (1991)[74]
	16.3	pyrite	Licht (1988)[c, 68]
	18.46	pyrite	Ball & Nordstrom (1991)[a, 75]
	15.6	marcasite	Licht (1988)[c, 68]
$Fe_3S_4(s) + 4H^+(aq) \rightleftharpoons 2Fe^{3+}(aq) + Fe^{2+}(aq) + 4HS^-(aq)$	45.04	greigite	Ball & Nordstrom (1991)[a, 75]
$HgS(s) + H^+(aq) \rightleftharpoons Hg^{2+}(aq) + HS^-(aq)$	39.1	red	Licht (1988)[c, 68]
	39.4	red	Smith & Martell (1976)[78]
	38.7	black	Licht (1988)[c, 68]
	38.8	black	Smith & Martell (1976)[78]
$ZnS(s) + H^+(aq) \rightleftharpoons Zn^{2+}(aq) + HS^-(aq)$	11.49	sphalerite	Daskalakis & Helz (1993)[63]
	11.62	sphalerite	Ball & Nordstrom (1991)[a, 75]
	11.5	sphalerite	Licht (1988)[c, 68]
	11.39	sphalerite	Bowers et al. (1984)[79]
	10.68	sphalerite	Myers (1986)[67]
	9.68	wurtzite	Ball & Nordstrom (1991)[a, 75]
	8.7	wurtzite	Licht (1988)[c, 68]
	8.5	wurtzite	Myers (1986)[67]
	8.0	amorphous	Licht (1988)[c, 68]
	9.05	amorphous	Ball & Nordstrom (1991)[a, 75]

Table 1. (continued) Values of solubility products for selected metal sulfides.

Reaction	pK_{sp} (T=298,15 K, I = 0)	Phase	Source
$CdS(s) + H^+(aq) \rightleftharpoons Cd^{2+}(aq) + HS^-(aq)$	14.36	greenockite	Daskalakis & Helz (1992)[80]
	13.08	not specified	Myers (1986)[67]
	15.9	not specified	Licht (1988)[c, 68]
	15.93	greenockite	Ball & Nordstrom (1991)[a,75]
$PbS(s) + H^+(aq) \rightleftharpoons Pb^{2+}(aq) + HS^-(aq)$	12.78	galena	Uhler & Helz (1984)[e, 81]
	13.5	galena	Myers (1986)[67]
	15.2	galena	Licht (1988)[c, 68]
	12.1	galena	Nims & Bonner (1929)[82]
	15.13	galena	Ball & Nordstrom (1991)[a,75]
$Cu_2S(s) + H^+(aq) \rightleftharpoons 2Cu^+(aq) + HS^-(aq)$	35.1	chalcocite	Licht (1988)[c, 68]
	34.62	chalcocite	Ball & Nordstrom (1991)[a,75]
$CuS(s) + H^+(aq) \rightleftharpoons Cu^{2+}(aq) + HS^-(aq)$	22.27	covellite	Shea & Helz (1989)[83]
	22.9	covellite	Licht (1988)[c, 68]
	23.04	covellite	Ball & Nordstrom (1991)[a,75]
	22.20	covellite	Myers (1986)[67]

[a] Ball and Nordstrom (1991) contains a compilation of revised thermodynamic data that was available in 1991. The original sources can be found from the referred publication.
[b] Benning et al. (2000) used an aged precipitate that was probably mackinawite.
[c] Licht (1988) calculated the pK_{sp} values from the free energies of formation of metal sulfides and the individual ions available at the time. For $HS^-(aq)$ he used a value of $\Delta_f G^0(HS^-)_{aq} = 12.05$ kJ/mol.
[d] A recommended value based on an excellent revision of literature values conducted by OECD NEA. The estimated uncertainty of this value is ±0.4.[77]
[e] The value shown is that calculated by Shea and Helz (1989)[83] from the data of the original source taking into account the complexation of Pb^{2+} with chloride. This correction had not been made by the original authors.

3.1.1. Empirical Modelling of Metal Sulfide Solubility

The thermodynamic solubility products are not sufficient to model the actual solubilities of metal sulfides since they form soluble complexes as has already been mentioned. The stability constants of these various complexes need to be known if we are to develop useful solubility models. Unfortunately, there is often little consensus on which complexes are present in significant amounts and not surprisingly, the reported stability constants for these complexes vary quite much between different sources.[21]

The general procedure to develop empirical solubility models usually follows approximately the following workflow.[63, 65, 80, 84] First, a number of complexation reactions that could in

principle take place are written down and the expressions for their equilibrium constants are constructed. Other crucial equilibrium relations such Eqs. (1), (2) and (28) with mass- and charge balance equations must of course also be included. Also, some method for the calculation of activity coefficients must be applied. Typically, the extended Debye-Hückel equation or the Davies equation is used for this purpose since the experiments are usually conducted with solutions of relatively low ionic strength.[21] The above set of equations now defines the model, and the various unknown equilibrium constants are regarded as empirical parameters. Experimental solubilities are then measured over a desired range of pH, temperature, ionic strength, sulfide concentrations and pressure. Finally, some nonlinear optimization algorithm is applied to find the values of the unknown constants that best approximate the observed solubility behavior. The model is adjusted by excluding complexes with physically meaningless or small stability constants and possibly some new complexes are introduced to the model if no combination of the initially defined reactions can reproduce the observed results. An obvious flaw in this method is that the stability constants of the complexes are treated as empirical parameters and thus tell nothing about the structure or even the existence of the proposed complexes.[21] For example, all complexes of the form $\mathrm{Fe_x(HS)_{2x}}$ with $x = 1,2,\ldots$ can explain the experimental results obtained by Davison et al. (1999)[65] equally well as the authors pointed out themselves. Thus, there is a risk that the solution obtained by the algorithm is not unique[21] and overfitting is possible when using many adjustable parameters.

Figure 7 shows an example of such solubility model given by Daskalakis and Helz (1993)[63]. These authors fitted several one- to eight-complex models to their data according to a procedure like that described above and arrived at the conclusion that their solubility results could be modelled by three zinc sulfide complexes, $\mathrm{Zn(HS)_4^{2-}}$, $\mathrm{ZnS(HS)^-}$ and $\mathrm{ZnS(HS)_2^{2-}}$. In the original publication the authors also included a zinc chloride complex of the form ($\mathrm{ZnCl^+}$) but it has been omitted in creating Fig. 7 since the contribution of this species to the apparent solubility according to the proposed model was not significant in any pH region. To keep the discussion and the illustrations simple all systems herein are assumed to contain only $\mathrm{S, H, O}$, the metals of interest and some inert electrolyte for ionic strength adjustment. For the same reasons, the formation of hydroxide or mixed hydroxide-sulfide complexes will not be considered. For the estimation of solute activity coefficients, the previously mentioned authors used the extended Debye-Hückel equation:

$$\log_{10}\gamma = \frac{-Az^2 I^{1/2}}{1 + aBI^{1/2}} + CI, \tag{29}$$

where A and B (cm^{-1}) are the Debye-Hückel parameters, a is a factor accounting for the finite size of the hydrated ions (cm) , I is ionic strength $(\mathrm{mol\ kg}^{-1})$ and C is an empirical parameter trying to account for the increasing ion-solvent and ion-ion interactions and the change in the dielectric constant of the solution with increasing molality. The parameter also corrects for the error, which results from using molalities instead of molarities which arises because the Helmholz (constant volume) free energy has been used in derivation of the Debye-Hückel limiting law. For a, the authors used values of $0.5\ \mathrm{nm}$ and $0.6\ \mathrm{nm}$ for monovalent and divalent ions respectively. In this thesis an even simpler modification of Eq. (29) called the Davies equation[85] has been used to model the activity coefficients for creating the illustrations of the various speciation models so that consistency in the estimation of the activity coefficients is achieved.

$$\log_{10}\gamma = -Az^2\left(\frac{I^{1/2}}{1 + I^{1/2}} - 0.3I\right), \tag{30}$$

where $A = 0.5085$. This is reasonable since the figures presented here are meant only to provide some rough guidelines on how the solubilities of different metal sulfides might behave in low ionic strength solutions ($\mathrm{I} \leq 0.5\ \mathrm{mol\ kg}^{-1}$) and how they compare with respect to each other. Furthermore, Eq. (29) itself is already quite a drastic simplification so not much practical value is lost in using Eq. (30) instead. The activity of water has been assumed to be unity and the activity coefficients of neutral species were taken to be 1. The total sulfide concentration is taken to be given by the relation $m_{\mathrm{S(-II),tot}} = m_{\mathrm{HS^-}} + m_{\mathrm{H_2S_{(aq)}}} + \sum m_{\mathrm{S(-II),complexed}}$. The regression analysis carried out by Daskalakis and Helz[63] resulted in stability constants $(\log_{10}K_{\mathrm{yz}})$, $\log_{10}K_{00} = -18.47$, $\log_{10}K_{44} = -3.83$, $\log_{10}K_{21} = -4.64$, and $\log_{10}K_{32} = -5.33$ for the following reaction:

$$\mathrm{ZnS(s)} + (2y - z - 2)\mathrm{HS^-(aq)} + (z - y + 1)\mathrm{H_2S(aq)} \rightleftharpoons \mathrm{ZnS}_y\mathrm{H}_z{}^{-(2y-z-2)}\mathrm{(aq)} \tag{31}$$

The distribution of $\mathrm{H_2S}$ between liquid and gas phases was not considered as there was no mention about the volume of the possible headspace in the article. The experiments were conducted in sealed ampoules and if the headspace volume was very small it is probably feasible

to assume that the hydrogen sulfide stayed almost quantitatively in the solution. The vapor-liquid equilibrium could, however, easily be incorporated in this model by introducing gaseous H_2S to the mass balance assuming that the distribution of H_2S between vapor and solution phases follows Henry's law:

$$p_{H_2S} = k^{m}_{H_2S} m_{H_2S}, \tag{32}$$

where p_{H_2S} is the partial pressure of H_2S, $k^{m}_{H_2S}$ is the Henry's law constant for hydrogen sulfide expressed in molal units and m_{H_2S} is the molality of hydrogen sulfide in the solution phase. It should naturally be kept in mind that Henry's law is only valid for dilute solutions.[33]

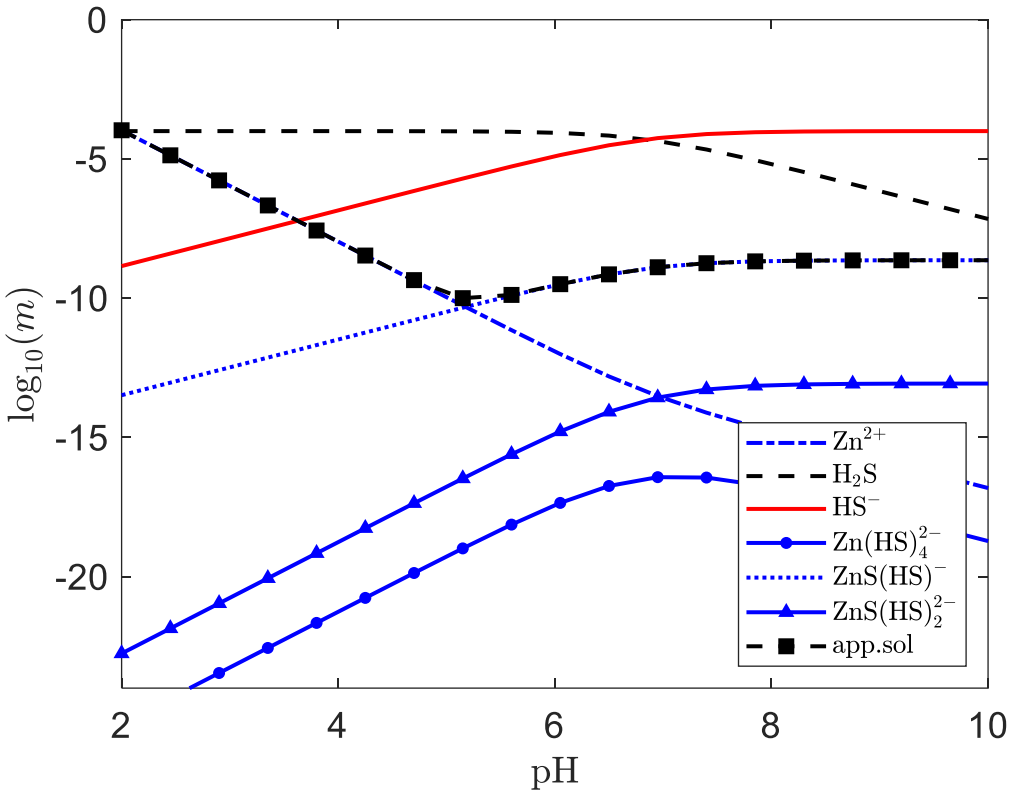

Figure 7. Calculated apparent solubility of sphalerite (app.sol) and the molalities of individual species as functions of pH according to the three-complex-model proposed by Daskalakis and Helz.[63] $T = 298.15$ K, $I = 0.3$ mol/kg and $m_{S(-II),tot} = 10^{-4}$ mol/kg.

Similar empirical solubility models for various other metal sulfides have been constructed.[10, 64, 65, 80, 86, 87] The solubilities of several metal sulfides as functions of pH according to few such investigations are summarized in Fig. 8. The pH range shown for each metal has been limited to the region covered experimentally in each corresponding study. In addition to pH, the

solubilities are also dependent on the concentration of total divalent sulfur, $m_{\mathrm{S(-II),tot}}$, which has been fixed to a value of 0.01 mol/kg in Fig. 8. All of the presented models cover at least a range of about $0.01\ \mathrm{mol/kg} < m_{\mathrm{S(-II),tot}} < 0.1\ \mathrm{mol/kg}$, but the investigations by Rickard[64] and those of Daskalakis and Helz[63, 80] for the solubilities of FeS, ZnS and CdS included experimental datapoints with $m_{\mathrm{S(-II),tot}}$ as low as $(10^{-6} - 10^{-4})$ mol/kg.

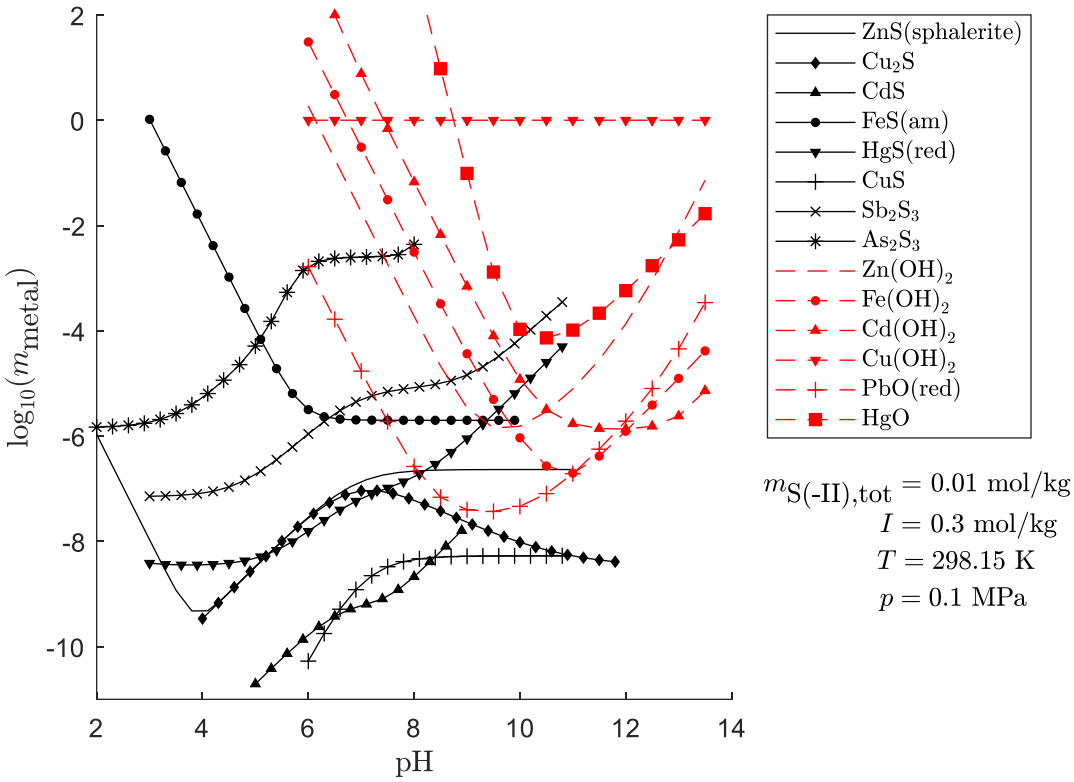

Figure 8. The calculated solubilities of various metal sulfides according to some empirical speciation models. References as follows: ZnS[63], Cu_2S[86], CdS[80], FeS[64], HgS[88], CuS[10], Sb_2S_3[89] and As_2S_3[90]. The activity coefficients have been calculated with Eq. (30). For CuS, the more recent solubility product from Shea and Helz (1989)[83] was used and the stability constants of the two complexes were extrapolated to infinite dilution using the Davies equation. As_2S_3 has been assumed to be in equilibrium with AsS, so $a_{S^0} = 3.91$.[90] See Fig. 2 for the sources of the hydroxide data.

Fig. 8 also gives information on the relative solubilities of the various metal sulfides in dilute solutions with no zerovalent sulfur present. (Except for arsenic, for which the equilibrium between solid orpiment and solid realgar has been assumed to control the activity of zerovalent sulfur.) This figure highlights the fact that the solubilities generally exhibit a complex

dependency on pH (and HS^- concentration which is not shown here). By comparing Figs. 2 and 8 the magnitude of the errors resulting from the use of only solubility products for the predictions of solubilities becomes clear. Polysulfide equilibria [Eq. (26)] have been almost completely omitted in generating Fig. 8, which is most likely an erroneous assumption for most industrial processes or natural systems. Although free polysulfide species have not been considered, some of the considered soluble species are in fact metal polysulfide complexes. Reactions with other ligands such as Cl^- or CO_3^{2-} have not been considered. Also, the structures or even the existence of most of the complexes proposed by the empirical models have not been verified experimentally.[21] As should be clear by this point, the speciation of metals in sulfidic solutions is a complicated issue that is not well understood.

This is well illustrated by Lacour et al. (2005)[91] who tested the applicability of four commercial thermodynamic simulation tools with included databases, namely Minteqa2,[92] Mineql+,[93] OLI Systems Inc. ESP Process and Stream Analyser[94] and Aspen Plus[95] to model the solubility of copper sulfide in a sulfide precipitation reactor. The authors also compiled a set of independent literature values for the equilibrium constants of numerous reactions that potentially affected the solubility and used this data to generate solubility models in a similar manner as has been done in this work to draw Fig 8. It turned out that the differences between the experimental and simulation results obtained using the commercial software were at worst about 20 orders of magnitude. All the commercial programs severely underestimated the copper solubility. This resulted mainly from the fact that the programs' databases were completely lacking data on species that participate in controlling the solubility of copper, such as $CuHS^+$, $Cu(HS)_2^0$ and $CuS(HS)^-$. It should be noted that the discussed databases may have been significantly updated since 2005 and better results might be obtained with the more recent versions of the software. Also, the solubility models constructed by combining the stability constants from different independent sources exhibited so much variation, that the differences in predicted copper solubilities using different combinations of literature data were about 10 orders of magnitude at largest. This illustrates the magnitude of the uncertainties related to the present, largely empirical solubility models and acts as a healthy reminder that models such as those presented in Fig 8. should not be trusted too much and their applicability to any real situation should always be critically evaluated.

3.1.2. Voltammetric Methods for the Determination of Stability Constants

The empirical fitting methods to determine stability constants from solubility measurements are somewhat problematic in the sense that it is possible to have a good fit of the results even if the proposed complexes do not actually exist.[21] Thus independent measurements of the stability constants with different techniques are needed to verify their validity. One of these approaches to determine stability constants utilizes voltammetry which has been applied to metal sulfide systems in several studies, like those of Luther et al. (1993)[96] and Chadwell et al. (1999, 2001)[57, 58]. In voltammetry, current as a function of applied potential is recorded and the location of a current peak is directly related to the standard reduction potential of the reaction responsible for it. The peak height is directly proportional to the concentration of the species involved in the reaction in question.[33, 97] Typically the working electrode is connected to an auxiliary electrode (e.g. a platinum wire) through which the current flows and the potential of the working electrode is measured against a separate reference electrode (e.g. SCE) through which no current flows.[97] In these methods a current signal produced by some suitable species, usually that of sulfide (or polysulfide) ions at a working electrode made of mercury is monitored. This reaction may be expressed as[60]

$$\mathrm{Hg(s) + HS^-(aq) \rightleftharpoons HgS(s) + H^+(aq) + 2e^-}, \tag{33}$$

and the electrode potential for this half-reaction (written in the direction of reduction) is given by the Nernst equation:

$$\mathrm{Eh} = \mathrm{Eh}^0 - \frac{RT}{2F} \ln\left(\frac{\{\mathrm{HS^-}\}}{\{\mathrm{H^+}\}}\right), \tag{34}$$

where Eh is the measured half-cell potential at the electrode, Eh^0 is the standard reduction potential of the half-reaction (33), F is the Faraday constant and curly brackets denote activities of the enclosed species. If a species is not appreciably acidic or basic over the studied pH range, then the following general half-cell reaction for the species can be written:[21]

$$\mathrm{RH}_q \rightarrow \mathrm{O} + q\mathrm{H^+} + n\mathrm{e^-}, \tag{35}$$

where R denotes the reduced form of the species that is oxidized to yield O. If the species R is a sulfide, then $n = 2$. The slope of the plot of Eh versus pH is now given by[21]

$$\frac{\mathrm{d(Eh)}}{\mathrm{d(pH)}} = -0.05915\frac{q}{n}. \tag{36}$$

Thus, the observed slope of such a plot reveals the number of protons attached to the predominant form of the electroactive species in the corresponding pH range. Also, the equilibrium constant of the reaction between the two forms of the electroactive species (e.g. K_{a1} of H_2S) is obtained from the point of intersection of two adjacent lines with differing slopes.[21]

The stability constants of metal sulfide complexes that are electroactive can be determined for example, by following the procedure developed by DeFord and Hume (1951).[98] In this procedure, the sulfide solution is titrated with the metal containing solution at constant pH and both the decrease in current and the positive shift in potential of the sulfide peak [Eq. (33)] are recorded as the metal is added. The successive formation constants of metal sulfide complexes such as $[\mathrm{Me(HS)}]^{+}$, $[\mathrm{Me_2(HS)}]^{3+}$ etc. can be determined by utilizing Eqs. (37)–(39):

$$n\mathrm{Me}^{2+}(\mathrm{aq}) + \mathrm{HS}^{-}(\mathrm{aq}) \rightleftharpoons \mathrm{Me}_n(\mathrm{HS})^{(2n-1)+}(\mathrm{aq}), \quad \beta_n = \frac{[\mathrm{Me_n(HS)}^{(2n-1)+}]}{[\mathrm{Me}^{2+}]^n[\mathrm{HS}^{-}]}, \tag{37}$$

$$F_0([X]) = \sum_{i=0}^{n} \beta_n [X]^n, \tag{38}$$

$$\log_{10}[F_0([X])] = 0.434\frac{nF}{RT}\Delta\mathrm{Eh} + \frac{\log_{10}(I_{\mathrm{p,s}})}{I_{\mathrm{p,c}}}, \tag{39}$$

where $F_0([X])$ is a polynomial defined by Eq. (38), $[X]$ is the total concentration of the added species, β_n is the stability constant of n$^{\mathrm{th}}$ complex, ΔEh is the measured positive shift in potential and $I_{\mathrm{p,s}}$ and $I_{\mathrm{p,c}}$ stand for the peak currents of the measured signal corresponding to the free HS^{-} and the complexed anion respectively. Note that the above approach only works if the complex is labile, that is, it dissociates at the electrode and produces a current signal.[21]

In addition to the DeFord and Hume methodology, at least four other approaches utilizing voltammetry have been used.[21] These include a method, where the peak current relative to the initial peak current measured in the absence of the metal is monitored at constant total sulfide concentration and the signal is interpreted as the free sulfide ion concentration. With appropriate mass balance and equilibrium equations this information can be used to determine the stability constants of the studied complexes. A second alternative method is the so-called competitive

ligand approach, which is very similar to the previous method, but now the change in the concentration of the metal ion is monitored as sulfide is added to the system. To measure the concentration of the "free" metal, it must be complexed with some ligand (e.g. 8-hydroxyquinoline) that exhibits a suitable current peak and is not too stable compared to the metal sulfide complexes. The two remaining methods are the mole ratio method and the chelate scale method. In the mole ratio method, either the concentration of free sulfide or free metal is measured as the other species is added. From the titration data, the reaction stoichiometry can be determined. Now, if the total amounts of both components are known, the mole fraction of the complexed metal can be calculated at given conditions, which allows for the direct calculation of the equilibrium constant. The chelate scale approach utilizes the direct thermodynamic relation between the peak potential (or the half-wave potential) and the equilibrium constant. A detailed discussion of these methods is beyond the scope of this work, and the reader should refer to Rickard and Luther (2006)[21] for further information.

3.1.3. Constructing Solubility Models from External Data

As with any thermodynamic equilibrium constant, the thermodynamic stability constants of the metal sulfide complexes can at least in principle be calculated from Gibbs free energy of formation ($\Delta_f G^0$) data utilizing Hess's law provided that the standard values of thermodynamic quantities (e.g. enthalpy and entropy of formation) for an appropriate set of species are known.[33] Estimates of these values obtained using a wide variety of experimental and computational techniques may be found in the literature. There also exists several commercial and freely available thermodynamic databases that contain large amounts of thermodynamic data. Such databases include for example DIPPR 801®[99], FREED®[100], HSC Chemistry®[56] and the FactSage®[101] databases.

Unfortunately, this approach also is not free of problems. The main problem with the $\Delta_f G^0$ approach is related to the incompatibility between data from different sources.[21, 102] It is difficult if not impossible to verify that none of the values included in the database of the model is in error and even a single erroneous value will affect the whole thermodynamic network, since many values are interconnected through thermodynamic relations which in turn must hold for the data to be internally consistent.[102] If the thermodynamic relations do not hold between the values given in a dataset, then some of the values are obviously erroneous and any equilibrium

calculations based on the data can give meaningless results. This issue of achieving internal consistency is a common problem with thermodynamic databases in general.[102]

The severeness of the effect of erroneous values in a thermodynamic database depends on the species to which the erroneous value is assigned. For example, the Gibbs free energy of formation of $Fe^{2+}(aq)$ was long disputed, since many electrochemical measurements suggested a value of $\Delta_f G^0(Fe^{2+}, aq, T = 298.15\ K, p = 0.1\ MPa) = -79.8\ kJ/mol$ whereas several other workers had obtained a significantly lower value of about $-90\ kJ/mol$ by using solubility techniques.[21] Later, in a critical review by Parker and Khodakovskii (1995)[103], it was concluded that the measurements suggesting the higher value were most likely in error due to the inability to properly account for the kinetic effects in the measurement of the standard potential of the Fe^{2+}/Fe electrode. It can be easily realized, that if a database was based on the erroneous value of $\Delta_f G^0(Fe^{2+}, aq)$, then the derived $\Delta_f G^0$ values for all species that are connected to $Fe^{2+}(aq)$ in some way, would also be in error. Another example relevant to sulfide chemistry is of course the infamous $\Delta_f G^0(S^{2-}, aq)$, or in other words, the pK_{a2} value for H_2S.

To conclude, the dataset used to construct the solubility model should be internally consistent but even if this requirement is fulfilled there is still a chance for the whole network to be in error. Thus, to accurately model the solubility by using external thermodynamic data, a critical and careful evaluation of the used values is required.[21]

3.2. The Concept of System

In section 3.5, the Eh – pH diagrams of various metal sulfide systems will be given. However, before they are presented, the concept of *system* should be discussed in some detail. In thermodynamics, the system is the part of the world that we are interested in and everything else belongs to the surroundings.[33, 104] A system is *closed* if no matter can enter or leave the system and the system is said to be *isolated* if no energy can enter or leave the system.

The proper definition of the system and any assumptions imposed on it is essential before any thermodynamic calculations are carried out since the obtained results will depend greatly on how the system is defined. For example, if we define our system to be an aqueous solution in a bottle open to the atmosphere then the true thermodynamic equilibrium of the system would be a situation in which practically all the water and perhaps some other components included in the system have been evaporated. Thus, there is no point in trying to find the true equilibrium

state of the system if one wants to estimate the concentration of some species in the bottle after some shorter timespan than it takes for the water to significantly evaporate. In order to perform practically meaningful thermodynamic calculations on a system like this, one would be forced to make assumptions such as that no evaporation occurs to any significant extent during the timespan of interest. After the calculations have been carried out, it must be verified that the assumptions made for obtaining the answers were in fact valid before the results can be interpreted. Otherwise, the obtained results are most likely meaningless. This rather artificial example illustrates that one must be careful when applying thermodynamics to real situations and that the true equilibrium often is not the state of practical interest.

3.2.1. Components

For the purposes of the chemistry of aqueous solutions it is often convenient to define the system in such a way, that any parts of it that can be treated homogenous are considered to form a single phase. If the composition of a phase is variable, that is it contains several *components*, then the phase is said to be a solution.[104] The question of what the components of a solution exactly are, is rather arbitrary at least from the viewpoint of thermodynamics. The number of components, however, is not.

The number of components is the minimum number of variables that are required to fully describe the composition of the solution. This means that a phase composed of, for example 10 hydrocarbons, that obviously contain only C and H, is a 10-component phase at low temperatures where the hydrocarbons are stable but is only a two-component phase at high temperatures where the hydrocarbons are rapidly decomposing and forming and an equilibrium between the various hydrocarbons is established. This follows, because the relative amounts of the different hydrocarbons are fixed by their Gibbs free energies of formation and consequently, the composition depends only on the amounts of C and H in the system.[104] This illustrates that the required number of variables to properly define the system may depend on its state (or conditions).

On the other hand, the fact that a component is merely an arbitrary independent variable allows us to choose quite freely the species used to designate it. If we have a set of chemical reactions that include the required number of species, whose relative amounts can be varied independently, plus an unlimited number of other species whose amounts can be expressed in

terms of the former, we can choose freely which of these species to use to designate the independent variables. These species do not even need to actually exist, although this must be remembered when applying the results of thermodynamic calculations to real life.

It may be more difficult to determine the number of components required to define a phase than it might seem at a first glance. For example, if the isotopic composition had a significant effect on some of the macroscopic (thermodynamic) properties of the phase being studied, then the different isotopes of the individual atoms would need to be considered as individual components.[104]

3.2.2. State of the System

The thermodynamic state of the system is defined when all its macroscopic thermodynamic properties are fixed to a constant value. Many of these properties, however, are related and consequently, only a single set of independent variables need to have known values for the state of the system to be defined.[104] The state of the system contains all information on the system at the corresponding moment of time, but it does not tell us how the system will behave in the future or how it has reached the current state.

The power, and also the limitations of thermodynamics pretty much arise from the fact that according to this definition, the difference in any property between two states depends solely on those two states and not upon the manner in which the system may pass from one state to another.[104] As was the case with determining the required number of components to define a phase, the determination of the required number of independent variables to define a thermodynamic state is not always easy. There is, however, a remarkable exception for the situation in which any number of phases are in equilibrium with each other. This is of course the famous Gibbs phase rule given by[33]

$$F = C - P + 2, \tag{40}$$

where F is the number of degrees of freedom for the system (i.e., the required number of independent variables), C is the number of components in the system (as defined above) and P is the number of phases in the system. The phase rule states that, for example, a single-component, single-phase system has always two degrees of freedom. This means that two independent variables, like temperature and pressure are required to completely define the state

of the system at a given point of time. Eq. (40) is valid only for systems in equilibrium where uniform normal pressure over all phases is the only external force acting on the system, surface contributions to the free energy of the system can be considered negligible, and the phase surfaces are deformable, heat conducting and permeable to all components.[33, 105]

3.2.3. Identifying Potential Species

The most difficult part in the generation of Eh – pH diagrams is the selection of the species to be included. Failing to include even a single species important in the real system can render the generated Eh – pH diagrams to be completely useless. On the other hand, thermodynamic calculations do not take into account the various energy barriers that can make a thermodynamically spontaneous reaction to be kinetically hindered and slow. It may be, that a system practically never reaches the equilibrium composition due to the high energy barriers of this type. Thus, for practical purposes, it may be necessary to exclude species whose formation is kinetically unfavorable. This type of Eh – pH diagrams corresponding to metastable situations were already encountered in section 2.4 where the chemistry of polysulfides was discussed. Often, the selection of suitable species must be based on empirical knowledge on the system being studied accompanied with enlightened guesses based on theoretical considerations.[106]

3.3. Eh – pH diagrams and Their Limitations

3.3.1. Principles and Assumptions Behind Eh – pH diagrams

Eh – pH diagrams show the boundaries of the regions of predominance for all the individual species. The shapes and the locations of these boundaries are determined by the Nernst Equation, which is given by Eq. (41) for an arbitrary half-cell reaction of the type $a\mathrm{A} + b\mathrm{B} + n\mathrm{e}^- \rightleftharpoons c\mathrm{C} + d\mathrm{D}$:[106]

$$\mathrm{Eh} = \mathrm{Eh}^0 - \frac{RT}{nF}\ln(Q) = \frac{RT}{nF}\ln(K) - \frac{RT}{nF}\ln\left(\frac{(a_\mathrm{C})^c(a_\mathrm{D})^d}{(a_\mathrm{A})^a(a_\mathrm{B})^b}\right), \tag{41}$$

where Eh^0 is the standard state reduction potential of the reaction, K is the equilibrium constant of the reaction, Q is the reaction quotient at the given composition and n is the number of electrons transferred in the reaction. The potentials in eq. (41) must be measured relative to the

potential of some reference half-cell, which typically is the standard hydrogen electrode (SHE). The standard reduction potential of the SHE is arbitrarily given a value of 0 V. The activity of electrons is always taken to be unity and its Gibbs free energy of formation is taken to be zero, so it does not appear in the equations. If for example, the species D is $H^+(aq)$, then the potential will depend on pH as given by

$$\mathrm{Eh} = \mathrm{Eh}^0 - \frac{0.059}{n}\log_{10}\left(\frac{(a_\mathrm{C})^c}{(a_\mathrm{A})^a(a_\mathrm{B})^b}\right) + \frac{0.059d}{n}\,\mathrm{pH}, \tag{42}$$

where the constants (with $T = 298.15$ K) have been lumped together into a single numerical constant including the conversion from natural logarithm to logarithm base 10. In the case of Eq. (42) a straight line with a positive slope is observed for Eh as a function of pH. If no protons were involved in the reaction, then the corresponding boundary would be a straight horizontal line (Eh independent of pH). If no oxidation or reduction takes place in the reaction, then the corresponding boundary will be a straight vertical line (The reaction is unaffected by Eh). Curved boundaries may also occur if a redox reaction results in a change of the activity of one pH affecting species relative to another. Most lines are, however, straight lines with varying slopes.[106]

The method of constructing the functions that define the boundaries corresponding to each reaction as described above is the traditional approach to generate Eh – pH diagrams. There is however, a more modern computational way to generate the figures. This method involves writing a complete mass balance for the system in addition to the equilibrium equations described above and solving the set of equations for the activities of each component in a vast number of grid points. Now the figure can be constructed since the predominant species at every point of the calculation grid is known.[107] Another similar approach suitable for computation, is to construct a function called Pourbaix potential, which gives the Gibbs free energy of formation of the species as a function of the chemical potentials of water and electrons (which can be expressed in terms of pH and Eh).[108] The stability regions of the species are then obtained by finding the halfspace intersections of the planes given by the Pourbaix potential functions for the various species.

3.3.2. Limitations of Eh – pH diagrams

As already indicated by the above discussion the Eh – pH diagrams contain many assumptions that limit their application to practice. The issue of metastability and the difficulty of selecting the appropriate set of species to include in calculation is one rather severe limitation of these diagrams as was mentioned earlier. Another subject that has also been encountered in earlier discussion is the unreliability and the limited availability of thermodynamic data on the species required to construct the diagrams.

In principle, the Gibbs free energies of formation for the species could be calculated *ab initio* by quantum mechanical calculations, but the current methods utilizing the Density Functional Theory (DFT) can reproduce Gibbs free energies of formation accurately only for solid compounds.[109] However, through the application of a few corrections and with the suitable selection of reference states, the free energies for solid compounds calculated using DFT can be combined with experimental data for aqueous and gaseous species to obtain internally consistent datasets applicable to thermodynamic calculations. Such an approach has been outlined by Persson et al. (2012)[109] who also showed that this approach could successfully reproduce Eh – pH diagrams constructed in the conventional manner.[109]

Despite of the recent advances in the development of computational chemistry, the generation of Eh – pH diagrams still relies firmly on experimental data. The dataset used in generating an Eh – pH diagram should naturally be internally consistent at least to a sufficient degree, which can be difficult to achieve, and it can reduce the amount of available data applicable to the system of interest. In commercial thermodynamic software, the uncertainties in the underlying thermodynamic data are not usually addressed by any visible means which may lead the careless user to be unaware of these inaccuracies. However, the uncertainties can have a significant effect on the predicted stability regions as can be realized by comparing Eh – pH diagrams from different sources.[110] Some values may also be considerably in error. Examples of such major errors include the formerly used too high value for $\Delta_f G^0(Fe^{2+}, aq)$[103] and the too low value of $\Delta_f G^0(S^{2-}, aq)$[12, 68]. Additional, but much lesser uncertainties arise from the inaccuracies related to the numerical methods used in calculation and to the resolution of the graphical representations.[110]

Naturally, the fact that the Eh – pH diagrams are usually represented in terms of activities instead of concentrations, limits their applicability to real situations. The errors resulting from

taking the activity coefficients to be unity becomes pronounced near the extremes of the pH scale of an Eh – pH diagram, since the concentrations of ionic species are naturally larger in such regions.[21] Activity coefficients can be modelled by the extended Debye-Hückel equation if the ionic strength is low, and the methods described by Bromley (1973)[111] and Pitzer (1973)[112] can be applied to high ionic strength systems.

When looking at Eh – pH diagrams, it should be remembered that the lines indicate the points where the activities of the adjacent species are equal. This means that although the indicated species is predominant on one side of this line, there is still a finite concentration of the other species as well. The concentration of the minor species decreases with increasing distance from the boundary.

3.4. Multicomponent Systems

The conventional three element (Me-O-H) Eh – pH diagrams can already present valuable information but often, systems of the real world contain many more elements than three. If these elements did not form compounds with each other, apart from O and H, the Eh – pH diagram for this system would simply be the superposition of the individual three-element Eh – pH diagrams. Naturally, this rarely is the case since as we well know, various complexes and ionic compounds are vital for understanding the vast majority of real-world processes, for example. The same basic principles described in section 3.3 apply for constructing Eh – pH diagrams of systems with more than three components but some complications still arise upon the introduction of additional elements. First, a distinction must be made between components that can be considered as part of the aqueous solution media and components that originate from solid solutions. This arises because in the construction of Eh – pH diagrams, the volume of the aqueous phase is taken to be infinite so the total aqueous concentration (or activity) of the aqueous species containing the element can be treated as constant. If, however, the component of interest is originally present in a solid solution, it is required to specify not the activity in the aqueous phase, but the molar ratio of the elements in the solid solution in order to preserve the mass balance in the calculations.[113]

Practical problems also arise quickly as the number of components is increased, since the number of possible species rises dramatically, and calculation times easily become unpractical. Specifically designed algorithms employing some pretreatment techniques such as filtering the

data for suitable candidate species are thus required to improve the computation efficiency.[108] Naturally, the availability of thermodynamic data for more complex compounds that may form in multicomponent systems is also severely limited and the risk of unintentionally neglecting some important compounds increases with increasing number of components. Also, the number of possible graphical representations increases as each of the elements can be considered as the main element which makes it difficult to present all the important information concisely. Considering these aspects of multielement diagrams, it was decided not to attempt to present Eh – pH diagrams for systems with more than four elements in this work.

It is also worth noting here that the Gibbs phase rule Eq. (40) can be neatly applied to Eh – pH diagrams to deduce the maximum number of solid phases that can occur simultaneously at any point of an Eh – pH diagram.[107] For example, inside any stability region in e.g., the Me-S-O-H system, Eh and pH can both be varied independently while still remaining inside the stability region and there are thus two degrees of freedom. The number of components is 5 since the electron must also be considered as a component. The maximum number of phases is thus $5 - 2 = 3$, one of which is the aqueous phase. Thus, if gaseous species are excluded, there may coexist two solid (or liquid) phases inside any stability region of the Me-S-O-H diagram. Similarly, the maximum number of coexisting solid phases at any boundary is three and at any triple point it is four. The number of solid phases can, however, be lower than the above considerations imply. This is explained by the fact that the actual thermodynamic number of components of the system may be lower than 5, since the *lowest* number of components that is enough to construct all the phases must be used in Eq. (40). This is the case for example, when some of the components is absent from all phases, or when the ratio of some elements is the same in all phases.

3.5. Eh – pH diagrams for the Me-S-O-H system

In this section, the Eh – pH diagrams for various metal (and metalloid) sulfide systems are presented. The figures have been generated with the EpH module of HSC Chemistry® 10 process modelling platform developed by Outotec®.[56] Only aqueous species and solid compounds have been considered, which limits the applicability of these diagrams to situations in which the gas phase equilibria can be neglected. Due to its controversial nature[12], $S^{2-}(aq)$ has been excluded from the calculations. The complete list of included species can be found in appendix A. All the

Eh – pH diagrams presented in this chapter correspond to a highly metastable situation where sulfur species with oxidation states higher than 0, metal oxides, and any large molecules or ions whose formation could be kinetically hindered in the short timescale of typical precipitation processes have been excluded. The excluded species have been shaded in the species list in appendix A. Eh – pH diagrams where all the listed species have been included can be found in appendix B. The thermodynamic enthalpy- and entropy of formation data used was taken directly from the database included in the software without any detailed evaluation of its reliability. A few species for which the data originated from clearly unreliable sources (low reliability rating given by the software database) were excluded. The original sources of the data can be found in the program's database.[56]

Diagrams drawn for both the metal and sulfur as the main element are shown. The water stability region, outside of which hydrogen or oxygen evolution will occur, is indicated by the two dashed lines. The activities of the metal and sulfur have been set equal and the value is about the same magnitude or somewhat larger as the typical molality of the metal in the untreated wastewater of an industrial zinc producer. Eh values are given against the SHE. The stability areas given in the figures correspond to the set of Eh and pH value pairs, for which the indicated species contains the largest proportion of the main element. Note that if there are multiple adjacent phases containing both the metal and sulfur in different stoichiometric proportions, the predominance areas of these species will depend on the selection of the main element. This follows, because relatively small changes in the equilibrium amount of for example, some sulfur rich phase, will result in a significant change in the proportion of total sulfur in the phase in question whereas the proportion of metal in that phase does not significantly change.

The species in the figures are written in the notation used by the HSC Chemistry software. The chemical formula of the species is given first without any subscripts followed by the possible charge and additional symbols that are needed to specify the nature of the species in parentheses. The symbol "a", stands for aqueous species. For solid species no such symbol is used, but the possible allotropes, isomers etc. are distinguished from each other with appropriate uppercase letter combinations given in parentheses.

It cannot be overly emphasized that the species corresponding to each stability region is the *thermodynamically* most stable one of the *selected* set of species. The figures do not tell if there

exists some even more stable species that just was not included in the selected list of species or if the formation of the indicated species is kinetically hindered. In real systems, it is typical that the formation of stable compounds takes place through various less-stable intermediates, and the transformation to the most stable form may take extremely long periods of time.[76, 114] This is the case for example, with iron sulfide precipitates as stated by Anderko and Shuler (1997).[114] Thus for many practical situations it might be advantageous to exclude the metal sulfide phases with higher stabilities to obtain some insight of the metastable phases that could form under the studied conditions.[114] Despite of this, to keep the number of presented figures in reasonable limits, all metal sulfide compounds have been included in the calculation of the figures presented here and the likely occurring kinetic hindrances have not been considered. Thus, it is advised not to give too much meaning on the stability areas of the individual metal sulfide phases. They should be viewed merely as broad estimates of the Eh – pH regions where metal sulfide precipitates are likely to form without giving too much consideration to the morphology of the precipitate. As a final note, it should be remarked that the possible coexisting phases which are likely to be present as predicted by the Gibbs Phase rule are not shown in these figures.

3.5.1. Zn-S-O-H

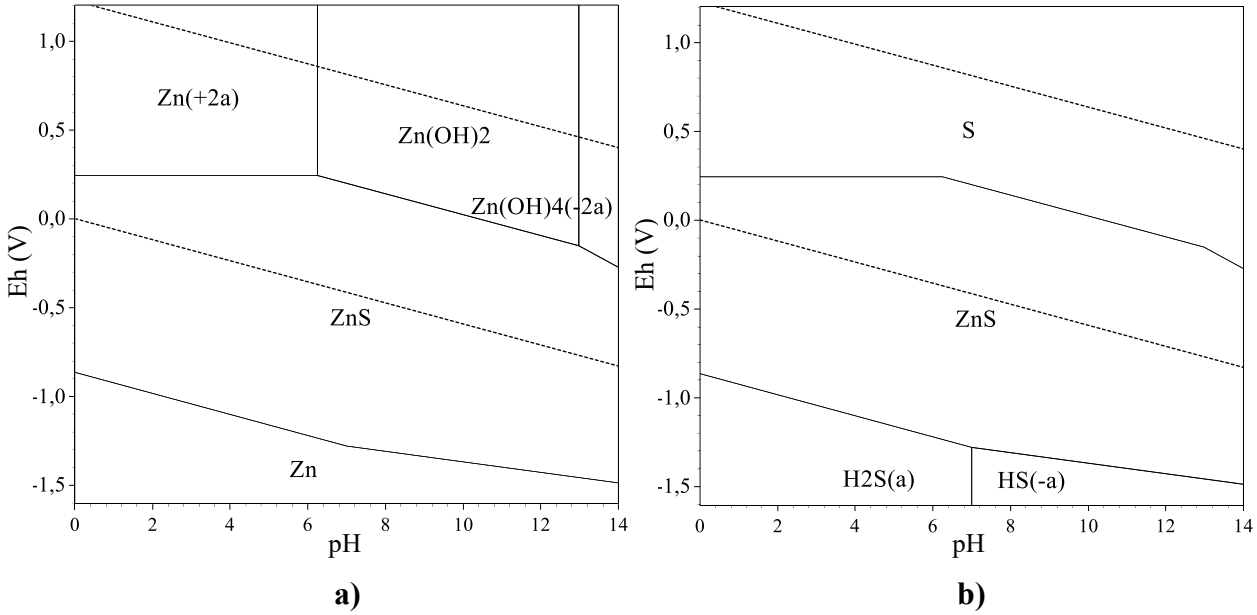

Figure 9. The metastable Eh – pH diagrams of the Zn-S-H_2O system at $T = 298$ K, $p = 0.1$ MPa and total zinc and sulfur molalities of 0.1 mol/kg. a) Zn as the main element b) S as the main element.

From Fig. 9 it is seen that zinc is expected to form sulfides over the entire pH range from 0 to 14 when the environment is not too oxidizing. At high pH, slightly more reducing conditions are required to keep zinc sulfide stable. The ZnS phase indicated in Fig. 9 is sphalerite. Hydroxide formation becomes possible when pH exceeds about 6. This figure also tells that both, aqueous H_2S and HS^- should be efficient in sulfidation except under highly reducing conditions. When performing sulfidation at low pH, care should be taken to not let the reduction potential of the system drop too much, since the risk of $H_2S(g)$ development increases with lower pH and Eh values. However, hydrogen evolution is expected to start to occur before the H_2S stability region is reached although there may be a large overpotential to overcome. Also, the change in Eh is often accompanied with a change in pH as is the case with adding sulfide containing the reagents. For example, although Eh can be significantly decreased by the addition of Na_2S to an aqueous system, it will also easily rise the pH so that the resulting Eh – pH value pair will lie in the safe region, where H_2S (g) development is not a risk. It must be remembered that the gas phase has not been considered in generating Fig. 9 so the areas where H_2S (g) development will occur cannot be accurately evaluated. Also, it must be emphasized that dangerous amounts of H_2S (g) can form in areas outside its stability region also since the lines only indicate the points where the activities of the adjacent species are equal and substantial amounts of both species are present in the near proximity of this boundary on both sides of it. The risk of H_2S (g) formation cannot be evaluated solely by inspecting Eh – pH diagrams since kinetic effects may also play a significant role in the system.

3.5.2. Fe-S-O-H

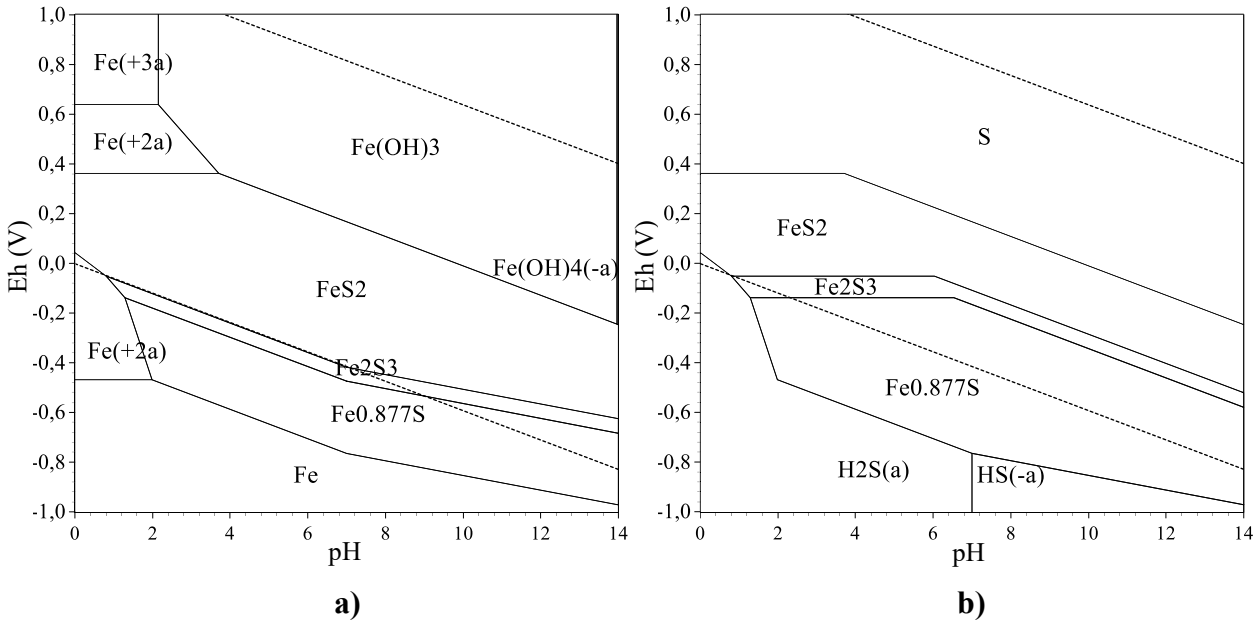

Figure 10. The metastable Eh – pH diagrams of the Fe-S-H_2O system at $T = 298$ K, $p = 0.1$ MPa and total iron and sulfur molalities of 0.01 mol/kg. a) Fe as the main element b) S as the main element.

Fig. 10 shows the regions of predominance for different iron and sulfur species in the Fe-S-H_2O system. It is seen that iron is expected to form insoluble sulfides on a broad range of Eh – pH values, but the dissolution of iron sulfide is expected to occur at low pH under both reducing and oxidizing conditions. Only at slightly positive Eh values pyrite is expected to be stable at low pH. Consequently, the risk of $H_2S\,(g)$ formation associated with sulfide additions is expected to be high when pH is low for systems containing only iron. In addition to pyrite, two other iron sulfide phases, namely iron(III)sulfide Fe_2S_3 and monoclinic pyrrhotite $Fe_{0.877}S$, exhibit regions of stability according to the data used here. The formation of iron(III)hydroxide $Fe(OH)_3$ under oxidizing conditions becomes possible when pH exceeds 2 and requires less and less oxidizing conditions as pH is increased.

The stability regions of the various iron sulfide phases relative to each other are different with different main elements, which can be explained by stoichiometric considerations. For example, there is 2 mol of sulfur but only 1 mol of iron in 1 mol of pyrite, which results in the fact that the proportion of sulfur in the pyrite phase declines more rapidly than the proportion of iron in it as pyrite starts to react to form other compounds. The predominance region of pyrite

is then expected to be narrower when sulfur is used as the main element which is indeed the case. The presence of three stable phases with differing stoichiometries complicates the discussion a little, and as a result, the stability region of $Fe_{0.877}S$ is in fact larger with sulfur as the main element. However, the reason behind this apparent anomaly lies in the same principles.

Although the mentioned phases are expected to be the thermodynamically stable forms of iron sulfide, it is highly probable that none of these phases is obtained in a short timescale process such as industrial precipitation. The synthetic precipitates have been typically observed to be amorphous FeS, or poorly crystalline mackinawite[64] that will subsequently transform to more stable iron sulfide phases upon ageing, as has been discussed by various authors.[76, 114-116] For example, precipitated mackinawite has been reported to be stable for up to 4 months in low temperatures in solutions containing reduced sulfur.[76]

The Eh – pH diagrams presented by Anderko and Shuler (1997)[114] for the Fe-S-H_2O system contain broadly the same features as Fig. 10 with the difference that their diagrams include iron oxides, and iron(III)sulfide was not included in their calculations. These authors also corrected for the difference between activity and molality using the Bromley's method to model the activity coefficients. The Bromley equation was considered more suitable for their purposes than the somewhat more extensive Pitzer equations since the empirical parameters of the former can be estimated from the properties of individual ions and thus large amounts of experimental data is not necessarily required as would be the case with the latter. The authors present a series of diagrams which show the stability regions of metastable iron sulfide species in addition to the diagram including all of the considered iron sulfide phases. Based on the consecutive stability diagrams with references to experimental observations, they propose the following replacement sequence for iron monosulfide species:[114]

$$\begin{aligned} FeHS^{+}(aq) \text{ or } FeCO_3(s) &\rightarrow FeS \text{ (amorphous)} \\ &\rightarrow FeS \text{ (mackinawite)} \\ &\rightarrow FeS \text{ (pyrrhotite)} \end{aligned} \tag{43}$$

They also note that the transformation of mackinawite to pyrrhotite is kinetically hindered and rarely observed in nature. Similar considerations led the authors to suggest that the formation of pyrite from any of the monosulfides can take place either directly or through the formation of marcasite or greigite depending on the conditions.[114] For an excellent general discussion on the

thermodynamics of the Fe-S-H_2O system, see the critical review by Lemire et al. (2013)[77] which is part of the OECD NEA Thermochemical Database Project.

3.5.3. Cu-S-O-H

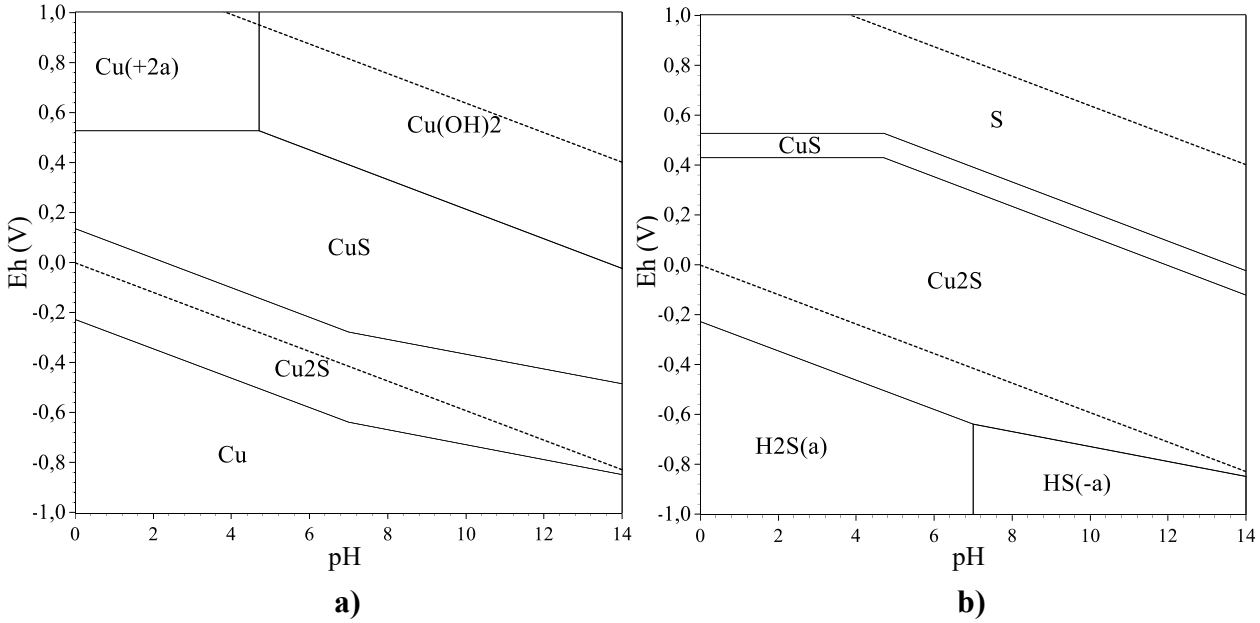

Figure 11. The metastable Eh – pH diagrams of the Cu-S-H_2O system at $T = 298$ K, $p = 0.1$ MPa and total copper and sulfur molalities of 0.001 mol/kg. a) Cu as the main element b) S as the main element.

The Eh – pH diagrams presented in Fig. 11 indicate that copper sulfides will form on a broad range of Eh and pH values under the specified conditions. The stable sulfides of copper according to these figures are covellite CuS and chalcocite Cu_2S whose relative abundances depend on both Eh and pH. The fact that the stability region of Cu_2S with sulfur as the main element is larger than with copper can again be explained by stoichiometric considerations. In 1 mol of CuS and Cu_2S there is the same amount of sulfur, but the amounts of copper are 1 and 2 mol, respectively. Thus, when Cu_2S starts to react to form other species, the proportion of copper in this phase declines more rapidly than the proportion of sulfur.

Only under highly oxidizing conditions and low pH, copper is expected to be in a soluble form. At higher pH and moderately positive Eh values, copper is expected to form mainly hydroxides. Remember that oxides of copper have not been considered since it was though reasonable to assume that within the typical timespan of a precipitation processes, typically

measured in hours at maximum, hydroxide precipitates can be considered metastable. The Eh – pH diagram (Fig. B3) for the Cu-S-H_2O system including all the species in the used database shows that Cu_2O, not $Cu(OH)_2$, is the thermodynamically stable form of copper in a significant region of Eh and pH values.

3.5.4. Cd-S-O-H

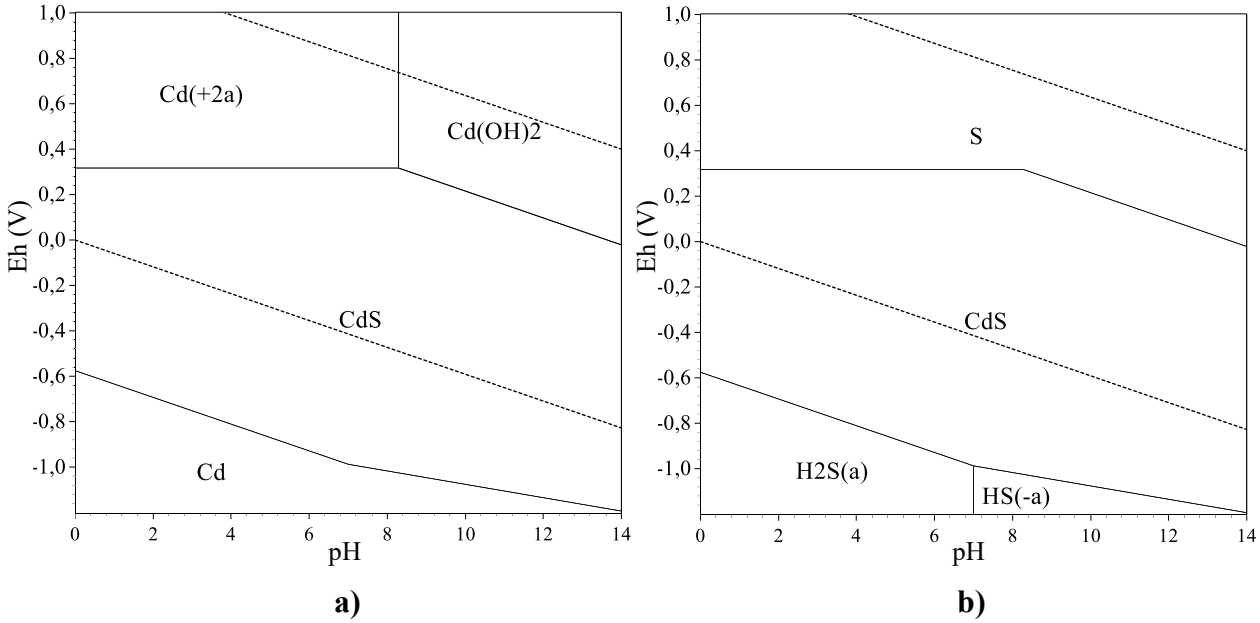

Figure 12. The metastable Eh – pH diagrams of the Cd-S-H_2O system at $T = 298$ K, $p = 0.1$ MPa and total cadmium and sulfur molalities of 0.001 mol/kg. a) Cd as the main element b) S as the main element.

The behavior of Cd-S-H_2O system is rather similar to the Zn-S-H_2O system as can be seen by comparing Figs. 12 and 9. As with Zn, Cd will form hydroxides at high pH under oxidizing conditions whereas CdS will be the dominant phase with all pH values when the conditions are not too oxidizing.

3.5.5. Pb-S-O-H

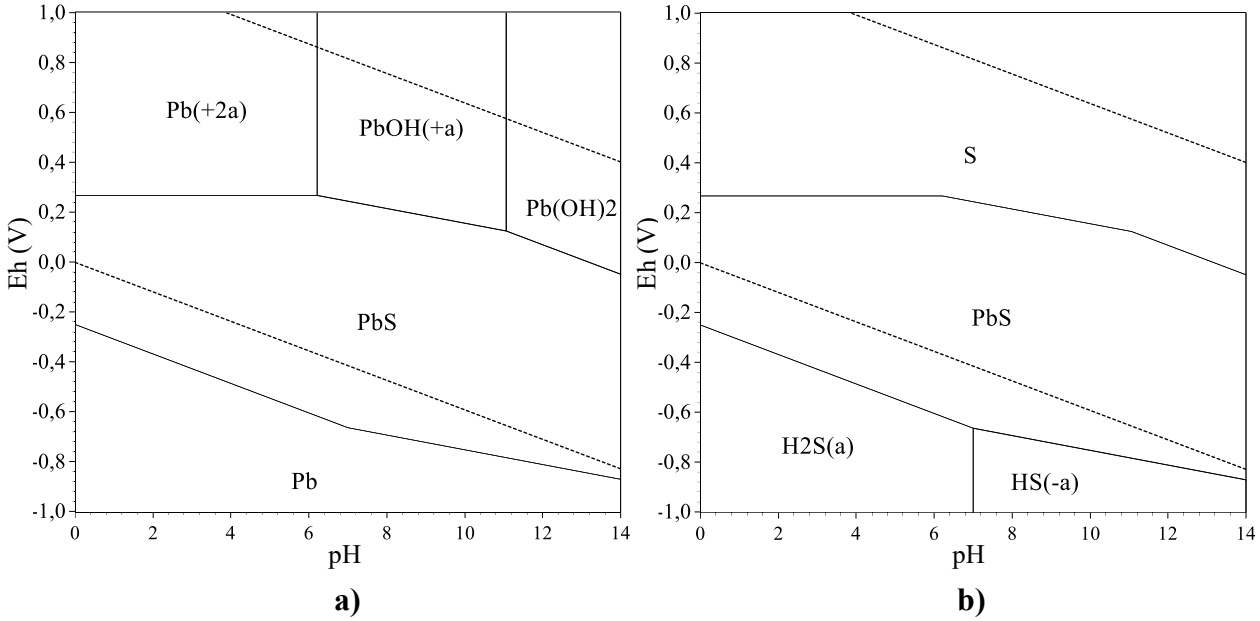

Figure 13. The metastable Eh – pH diagrams of the Pb-S-H_2O system at $T = 298$ K, $p = 0.1$ MPa and total lead and sulfur molalities of $1 \cdot 10^{-4}$ mol/kg. a) Pb as the main element b) S as the main element.

Fig. 13 shows that the equilibrium behavior of lead seems again to be very similar to that observed for zinc and cadmium. The only exception is that lead is expected to form a soluble hydroxide complex at moderate pH values and oxidizing conditions, and insoluble hydroxides will only form at high pH. Again, it is worth noting that the thermodynamically stable solid phases at high pH and Eh are oxides of lead, not $Pb(OH)_2$, as shown in Fig. B5. In general, it must be kept in mind that the number of species for which thermodynamic data is available is very limited and the chemistry of metal hydroxides and sulfides is certainly much more complicated than indicated by these simple figures.

3.5.6. Sb-S-O-H

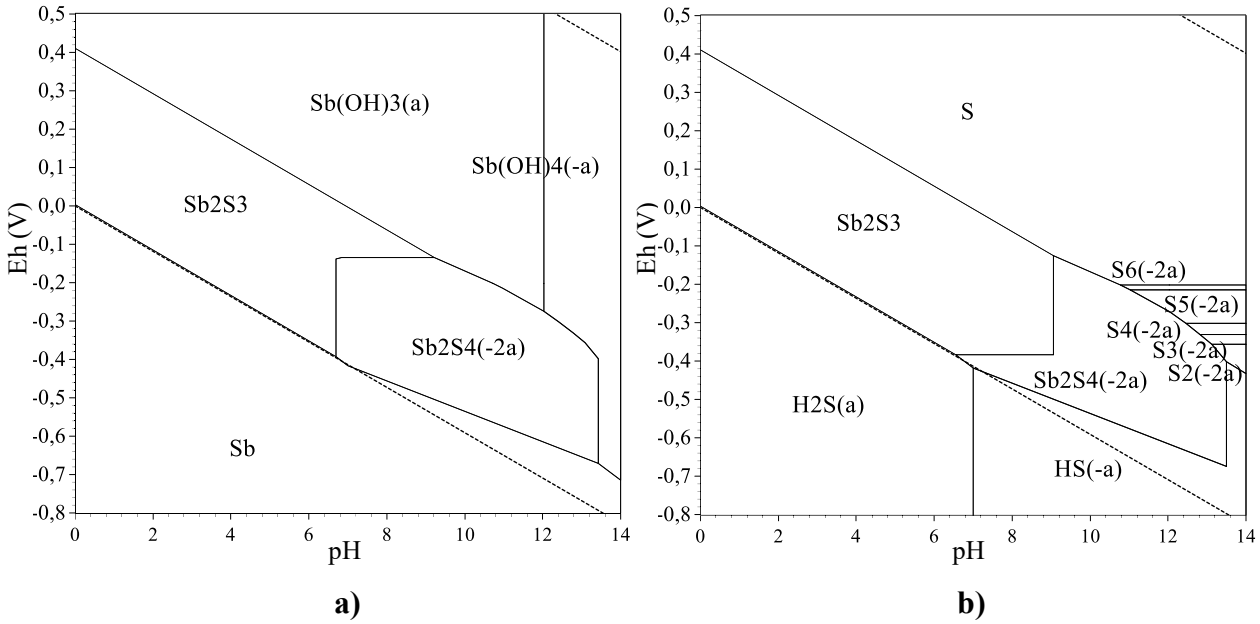

Figure 14. The metastable Eh – pH diagrams of the Sb-S-H_2O system at $T = 298$ K, $p = 0.1$ MPa and total antimony and sulfur molalities of $1 \cdot 10^{-4}$ mol/kg. a) Sb as the main element b) S as the main element.

According to Fig. 14, antimony behaves rather differently compared to the elements discussed so far, which is expected since Sb is a metalloid whereas the other elements have been metals. Antimony is expected to precipitate as stibnite Sb_2S_3 in low pH and moderate Eh values, which is the most abundant antimony containing mineral in nature.[117] At higher pH values, antimony forms a soluble complex $Sb_2S_4^{2-}$. On the contrary to the previous elements, polysulfides exhibit regions of stability in the Sb-S-H_2O system as indicated by Fig. 14 b). Again, Fig. 14 should be viewed with criticism since the number of species considered is very low. Not too surprisingly, the speciation of antimony in sulfidic solutions has been found to be more complicated than was initially thought as discussed in more detail by Helz et al. (2002).[118] Based on their results and previously reported observations, the authors suggested that both Sb(III) and Sb(V) are required to explain the solubility of antimony in sulfide containing environments.

3.5.7. *As-S-O-H*

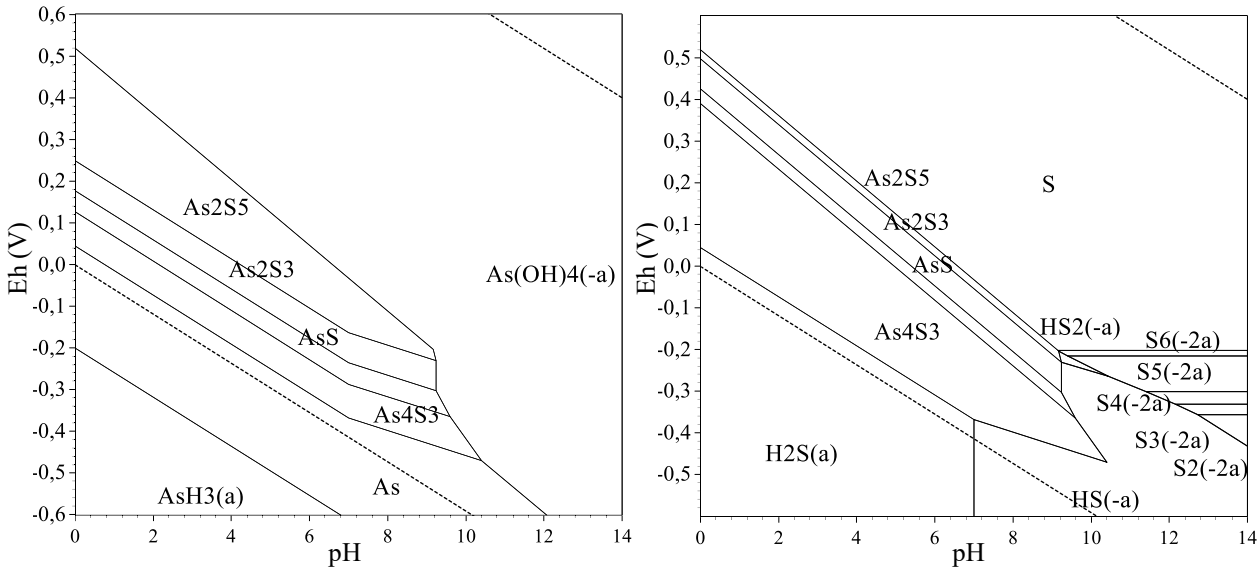

Figure 15. The metastable Eh – pH diagrams of the As-S-H_2O system at $T = 298$ K, $p = 0.1$ MPa and total arsenic and sulfur molalities of $1 \cdot 10^{-4}$ mol/kg. a) As as the main element b) S as the main element.

Like Sb, arsenic is a metalloid and consequently, similarities in their Eh – pH diagrams can be seen. Four different arsenic sulfide phases exhibit regions of stability under the specified conditions. On the basis of Figs. 14 and 15 it is reasonable to expect that antimony and arsenic can be efficiently removed by sulfidation provided that the pH is not too high. It is important to note that all arsenate, and oxythioanion species have been excluded from Fig. 15 to maintain consistency between the other diagrams presented in this section. This is however, a highly unrealistic assumption since arsenic occurs in nature mainly in the form of such species and they are practically always present in systems containing arsenic.[90, 119] The Eh – pH diagram including all such arsenic species found in the HSC Chemistry program's database is presented in Fig. B7, which is probably somewhat more informative than Fig. 15. In a paper by Couture and Van Cappellen (2011),[119] the present understanding on arsenic speciation in sulfidic environments is summarized quite thoroughly and a thermodynamic treatment based on critically evaluated data is presented. Their analysis illustrates that arsenic speciation is closely linked to the speciation of sulfur in the system, or more accurately, to the ratios $S^0(aq)/HS^-(aq)$ and $SO_4^{2-}(aq)/HS^-(aq)$ through affecting the Eh value of the system.[119] It is

recommended to refer to their paper for a more comprehensive discussion on arsenic speciation. It should also be noted that the Eh – pH diagrams presented in their work are more reliable than those presented here since their diagrams are based on the best, critically evaluated thermodynamic data available at the time of publication of their work.

3.5.8. Hg-S-O-H

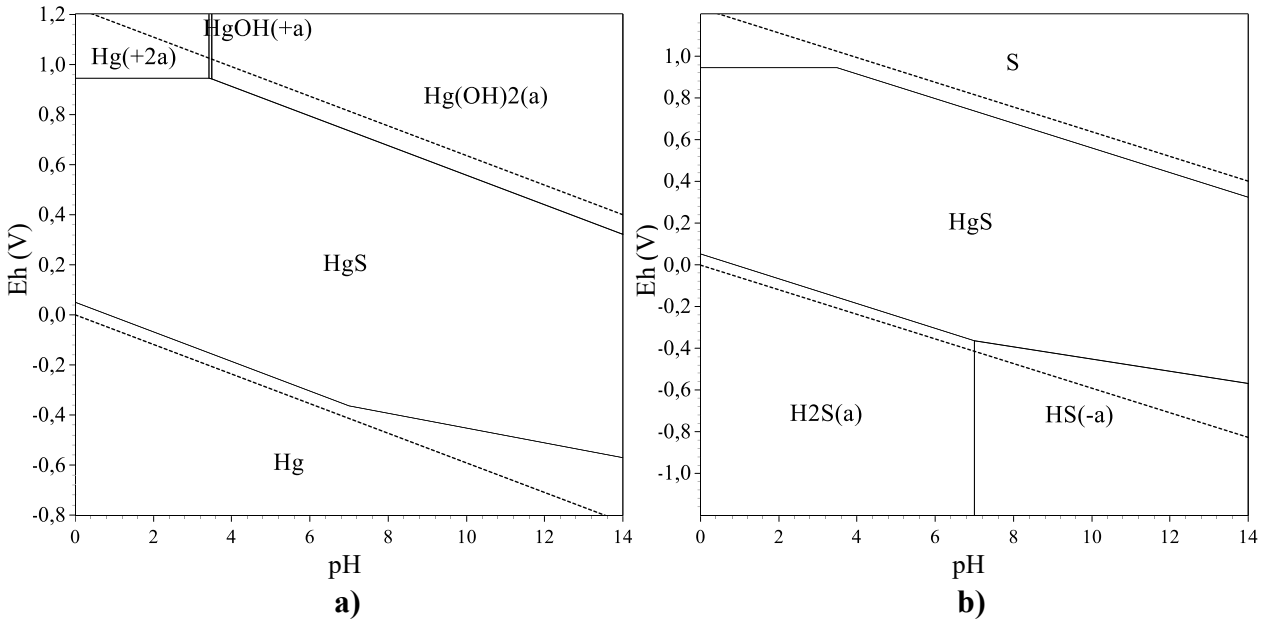

Figure 16. The metastable Eh – pH diagrams of the Hg-S-H_2O system at $T = 298$ K, $p = 0.1$ MPa and total mercury and sulfur molalities of $1 \cdot 10^{-6}$ mol/kg. a) Hg as the main element b) S as the main element.

Fig. 16 shows that mercury sulfide HgS, is expected to be stable almost in the entire stability region of water. At highly oxidizing conditions HgS should dissolve due to the oxidation of sulfide to zerovalent sulfur. Under these conditions, hydrated mercury(II)-ion $Hg^{2+}(aq)$, its hydroxide complex $HgOH^{+}(aq)$, or aqueous mercury(II)hydroxide $Hg(OH)_2(a)$ is expected to be the (meta)stable mercury species depending on pH. Again, Fig. B8 gives us indication, that the thermodynamically stable phase would actually be HgO. Also, by comparing Figs. 16 and B8 the effect of the metastability assumption to the stability region of HgS is clearly seen. In Fig. B8, there is a large region, where sulfur will oxidize to sulfoxides or further to sulfate, which will cause the reduction of Hg^{2+} to Hg, and thus the dissolution of HgS. Hence, by forcing

the sulfur to stay in a reduced form by excluding the oxidized sulfur species, the stability region of HgS is considerably increased in Fig. 16.

3.6. Application of Thermodynamic Models to Real Systems

Applying thermodynamics can be a powerful tool to gain insight about the behavior of real, industrial scale processes although it has its limitations also, as has been mentioned numerous times in the preceding sections. Not many studies seem to be available in the public literature which describe the application of rigorous thermodynamic models to real processes. Probably the main reason limiting the applicability of thermodynamic modelling in industry is the limited availability of thermodynamic data combined with the vast number of important species whose actual nature is often at least uncertain. However, some thermodynamic models have been successfully applied to industrial scale systems and this section gives one example of such a study. Another example, in which a simple thermodynamic model was applied to predict zinc concentration in the effluent of a small-scale MSMPR precipitator is also given.

Shakeri-Yekta et al. (2014)[120] constructed a thermodynamic model to predict the solubility and speciation of iron and trace metals in continuous full scale anaerobic digesters used to produce biogas. They applied their model to reactors with molar Fe：S ratios of both larger and lower than 1. Their model included a total of 68 reactions involving, inorganic and organic sulfide, polysulfide, carbonate, and phosphate species of the studied metals with equilibrium constants taken from various literature sources. In addition, they calculated a notable amount of saturation indices, that is, the ionic activity product divided by the solubility constant, of non-sulfide minerals of the trace metals. These were all negative indicating that the solution phases were undersaturated with respect to solid hydroxide, oxide, phosphate, and chloride minerals of the trace metals. There was no mention on the modelling of activity coefficients of the aqueous species so solution nonideality had apparently been ignored.

To model the solubility of iron(II)sulfide, the authors tried both the solubility model of Davison et al. (1999)[65] and that of Rickard (2006)[21]. The authors could not explicitly discriminate between these models since both resulted in reasonable overall modelling results although the resulting speciation of iron was different. Rickard's solubility model, however, resulted in a slightly better fit.[120]

The model input parameters were pH, temperature, partial pressure of $CO_2(g)$ and the total concentrations of Fe, Na, P, Cl and the trace metals. The total concentrations of thiols and inorganic sulfur were roughly estimated from the X-ray Absorption Near-Edge Structure spectroscopy (XANES) data. Since Fe was in great excess compared to the other metals, the modeling was conducted with the following three step process. First, the concentrations of various inorganic ligands and the organic thiols were calculated by using the estimated amount of total inorganic sulfur as the initial input which was slightly adjusted so that the modelled amount of $FeS(s)$ best conformed with the experimentally observed value. In the second step, the aqueous concentrations of $HS^-(aq)$ and organic thiols were adjusted so that the experimentally observed aqueous Fe concentration was matched as closely as possible. This approach was validated by applying it to model the sulfide concentrations in two laboratory scale reactors in which the partial pressure of $H_2S(g)$ was known and thus the concentration of $HS^-(aq)$ could be calculated. In conditions, where $Fe(II)$ dominated over sulfide, the solubility of $FeCO_3(s)$ was the adjustable parameter instead of the concentration of $HS^-(aq)$. The final step was to solve the speciation of the trace metals: $Co(II)$, $Ni(II)$, $Zn(II)$, $Cu(I)$, $Cd(II)$ and $Pb(II)$. Finally, all the steps were iteratively repeated until the best agreement between the experimental and modelled total Fe concentrations was obtained.[120]

The modelled $FeS(s)$ concentration in the sludge was found to agree very well with experimentally determined values. To successfully model the aqueous $Fe(II)$ concentration, the formation of metal-thiol complexes had to be allowed as described above which was thought to be reasonable, since experimental observations had supported the presence of thiols in the biogas sludge. With the above modelling approach, the measured total concentrations of the trace metals in all the studied reactors could be reproduced reasonably well and the speciation of the studied elements could be estimated.[120] Although successful in reproducing the experimental results, the modeling approach used by these authors is rather empirical in nature and contains many adjustable parameters that rely on experimental knowledge on the system. This is not surprising for systems of this degree of complexity, since all the numerous reactions and other important physical phenomena cannot be accounted for theoretically. Thus, the model has limited predictive ability and is meant more to provide information on the link between the speciation of trace metals and the more abundant elements than to predict the speciation in a system for which no prior knowledge is available.

Veeken et al. (2003)[20] constructed a 17 species thermodynamic model for ZnS precipitation in a MSMPR reactor. The model was observed to be able to reproduce the experimentally measured zinc concentrations in the effluent stream of the reactor fairly well over the entire pS range studied. They observed that the Zn concentration in the effluent exhibited a minimum at $pS = 15$ and increased at sulfide concentrations both lower and higher. This increase in solubility at higher sulfide concentrations was attributed to formation of soluble zinc sulfide complexes.

4. DYNAMICS OF SULFIDE PRECIPITATION

The preceding chapter was devoted to the thermodynamic aspects of sulfide precipitation, the knowledge of which is necessary, but not sufficient to develop a practically useful understanding of any real process. As has been mentioned, thermodynamics does not consider time as a variable so other theories are required to incorporate time dependencies into a process model. This is where the theories of chemical kinetics, mass transfer and fluid mechanics come into play. Garside (1985)[28] postulated in his review on crystallizer modelling, that a crystallizer (or precipitator) is essentially just a chemical reactor, and from the reaction engineering viewpoint, it can be treated in a similar manner than any other reactor but with a few distinct features. First, the participation of the solid phase in the reaction necessitates the incorporation of a population balance (see section 2.2.2) in addition to the mass- and energy balances. Another feature is that the kinetics of crystallization is divided in two separate parts: nucleation and growth.

The classical crystallization theory discussed briefly in section 2.2 combines the basic theories of chemical kinetics and mass transfer and has been widely used in describing the kinetics of precipitation processes. Due to the limited scope of the thesis, only a basic introduction could be given but many texts covering the subject on a general level can be found elsewhere.[2, 28, 31]

Fluid mechanics is a complete branch of physics which has seen wide application in chemical industry. As the available computational power has increased the significance and popularity of computational fluid dynamics (CFD) in practical applications has risen. It is not possible to treat this subject on a general level here since it would require a whole book. Comprehensive textbooks on fluid mechanics are however readily available and can be consulted for a detailed discussion on this field.[121, 122]

The purpose of the following sections is to present, how these basic theories and concepts have been applied to practice in the case of sulfide precipitation and to give some perception on how well they have worked. Each subsection has been devoted to some individual phenomenon and it is discussed, how the effect of the phenomenon could be included in models for sulfide precipitation systems.

4.1. Reaction Kinetics

Although precipitation kinetics is often modelled using the concepts of nucleation and crystal growth, conventional chemical kinetics can also be successfully applied to many such processes. An example of a study applying only conventional solution kinetics is that of Rickard (1995)[123], who investigated the precipitation of FeS using a capillary apparatus specifically designed to probe the short timescale (down to 100 ms) reactions involved in the process. The empirical rate law in terms of the concentration of total dissolved sulfide was of the form:

$$\frac{-\mathrm{d}[\sum \mathrm{S}]}{\mathrm{d}t} = k_0[\sum \mathrm{S}] \tag{44}$$

He found that the simple rate law given by Eq. (44) could be explained by a rather complex two-stage process, the first of which included two competing reaction pathways given by Eqs. (45) and (46).

$$\mathrm{Fe^{2+}(aq) + H_2S\ (aq) \rightleftharpoons FeS(s) + 2H^+(aq)} \tag{45}$$

$$\mathrm{Fe^{2+}(aq) + 2HS^-(aq) \rightleftharpoons Fe(SH)_2(s)} \tag{46}$$

Since reaction (46) dominated at high pH and sulfide concentrations whereas reaction (45) became dominant at low pH and low sulfide concentrations, he could obtain empirical rate laws separately for both of the reactions, which were of the form:

$$-\frac{\mathrm{d}\left(a_{\mathrm{H_2S}}\right)}{\mathrm{d}t} = k_1' a_{\mathrm{H_2S}}, \tag{47}$$

$$-\frac{\mathrm{d}(a_{\mathrm{HS^-}})}{\mathrm{d}t} = k_2' (a_{\mathrm{HS^-}})^2, \tag{48}$$

where k_1' and k_2' are the empirical rate constants with values of $90\ \mathrm{s^{-1}}$ and $1.3 \cdot 10^7 \mathrm{l\ mol^{-1}\ s^{-1}}$ at 25°C, respectively. Rickard also showed that both equations were consistent with Eigen-Wilkins mechanisms written for the corresponding reactions with the following theoretical rate expressions:

$$-\frac{\mathrm{d}\left(a_{\mathrm{H_2S}}\right)}{\mathrm{d}t} = k_{-\mathrm{w}} K_{\mathrm{OS}}' a_{\mathrm{Fe^{2+}}} a_{\mathrm{H_2S}}, \tag{49}$$

$$-\frac{\mathrm{d}(a_{\mathrm{HS^-}})}{\mathrm{d}t} = k_{-\mathrm{w}} K''_{\mathrm{OS}} K_{\mathrm{FeSH^+}} a_{\mathrm{Fe^{2+}}} (a_{\mathrm{HS^-}})^2, \tag{50}$$

where $k_{-\mathrm{w}}$ is the rate constant for the removal of water molecules from the inner sphere of the hexaaquairon(II) complexes, $K_{\mathrm{FeSH^+}}$ is the stability constant of the complex $\mathrm{FeSH^+}$, and K'_{OS} and K''_{OS} are the stability constants of the outer-sphere-complexes $\mathrm{Fe(H_2O)_6 \cdot H_2S^{2+}}$ and $\mathrm{Fe(HS) \cdot (H_2O)_5^+ \cdot (HS^-)}$, respectively. From these forms it is obvious that $k'_1 = k_{-\mathrm{w}} K'_{\mathrm{OS}} a_{\mathrm{Fe^{2+}}}$ and $k'_2 = k_{-\mathrm{w}} K''_{\mathrm{OS}} K_{\mathrm{FeSH^+}} a_{\mathrm{Fe^{2+}}}$. Rickard observed, that at least in his experiments the rate of the overall process could be approximated with Eq. (44) which essentially just sums the rates together. As Rickard also himself noted the, reaction rates will, however, depend on Fe(II) concentration also, but in these expressions its effect has been hidden within the empirical constants k'_1 and k'_2.

The second stage of the reaction was proposed to involve the conversion of the initially formed $\mathrm{Fe(HS)_2(s)}$ to amorphous $\mathrm{FeS(s)}$ through the relatively slow reaction of the form:[123]

$$\mathrm{Fe(HS)_2(s) \rightarrow FeS(s) + H_2S(aq).} \tag{51}$$

This step was required to explain the anomalous rise in $\mathrm{H_2S}$ concentration after about 400 ms reaction time and it had been recognized also earlier by Rickard (1989)[124]. However, direct experimental evidence of any intermediate solid phase could not be presented.

Detailed kinetic studies on sulfide precipitation that do not use crystallization concepts like those of Rickard can provide valuable mechanistic insight but are relatively rare. However, in many studies concentrated on modelling[6, 116, 125-127], simple empirical rate laws have been used to describe the kinetics of precipitation, which may be sufficient for practical purposes if the particle size distribution does not have to be modelled. It seems that in most studies utilizing CFD modelling, this simplified approach has been adopted and no population balance has been considered.[6, 126] However, the coupling of CFD calculations with population balance and a micromixing model has been demonstrated to be capable of predicting the resulting particle size distribution of a barium sulfate precipitation process.[38] This approach will be discussed in more detail shortly.

4.2. Crystallization Kinetics

To model the PSD of a precipitation process, the phenomena discussed in chapter 2 must be accounted for by appropriate mathematical descriptions. In this section, some models used to account for nucleation, growth, aggregation, and breakage are presented. The focus is on sulfide precipitation systems, but other examples have also been included since the available literature for metal sulfide systems is somewhat scarce and the same basic principles apply regardless of the substance being precipitated.

4.2.1. Nucleation

The theoretical background of nucleation was already briefly presented in section 2.2, so that discussion will not be repeated here. The high supersaturations typical for sulfide precipitation promote homogenous, or heterogenous nucleation and secondary nucleation can quite reasonably be ignored.[28] Thus, Eq. (11) or some modification of it is often used to incorporate nucleation in population balance models for such processes.[20, 30, 38, 39, 128-130] For example, the following expression, the derivation of which can be found in Mersmann (2001)[29], has been used quite successfully.[30, 38, 128]

$$J = 1.5D\left(\sqrt[\nu]{K_{\mathrm{sp}}}S_{\mathrm{sat}}N_{\mathrm{A}}\right)^{7/3}\sqrt{\frac{\sigma}{kT}}v_{\mathrm{m}}\exp\left[\frac{-16\pi\sigma^3{v_{\mathrm{m}}}^2}{3k^3T^3(\nu\ln S_{\mathrm{sat}})^2}\right], \tag{52}$$

where, according to Mersmann, the surface energy σ can be expressed as:

$$\sigma = \frac{K}{(v_{\mathrm{m}})^{2/3}}\ln\left(\frac{1}{v_{\mathrm{m}}N_{\mathrm{A}}\sqrt[\nu]{K_{\mathrm{sp}}}}\right)kT, \tag{53}$$

where K is an empirical parameter whose value should be determined experimentally. Mersmann however suggests that a value of $K = 0.414$ can be used for predictive calculations if no experimental data is available although the actual constant is probably slightly lower than this.[29] Probably the most simplified but still usable empirical expression for the nucleation rate is given by:[2, 20, 39, 131]

$$J = k_{\mathrm{N}}(S_{\mathrm{sat}} - 1)^n, \tag{54}$$

where k_{N} and n are empirical constants.

4.2.2. Growth

Although much better understood, crystal growth rate is also often modelled with simple empirical relations as is the case for nucleation rate. The actual mechanism of crystal growth depends greatly on the nature of the particles, or more specifically, on their surface roughness. Rough surfaces have many potential kink sites where surface integration may take place and continuous normal growth will be the dominating mechanism. On the other hand, if the particle surface is smooth, there are only a few sites, such as the steps associated with screw dislocations, on which the surface integration can occur, and growth rate can be limited by the rate of surface diffusion on the particle-solution interface. In the latter case, the dominating mechanism is the so-called layer growth, which means that the particle will grow in layer-by-layer manner. The layer growth scheme forms the basis of the well-established Burton-Cabrera-Frank theory[132], which in its simplest form predicts the linear growth rate of a face of a smooth crystal to be given by[132]

$$G_{\mathrm{r}} = k_{\mathrm{BCF}} \frac{(S_{\mathrm{sat}} - 1)^2}{\sigma_{\mathrm{BCF}}} \tanh\left(\frac{\sigma_{\mathrm{BCF}}}{S_{\mathrm{sat}} - 1}\right) \tag{55}$$

where k_{BCF} and σ_{BCF} are parameters that depend on temperature and the properties of the crystallizing substance and the crystallization media. The detailed forms of the parameters can be found in the original paper of Burton, Carbera and Frank.[132] At low supersaturations ($S_{\mathrm{sat}} - 1 \ll \sigma_{\mathrm{BCF}}$) Eq. (55) reduces to[2]

$$G_{\mathrm{r}} = \frac{k_{\mathrm{BCF}}}{\sigma_{\mathrm{BCF}}} (S_{\mathrm{sat}} - 1)^2, \tag{56}$$

and at high supersaturations ($S_{\mathrm{sat}} - 1 \gg \sigma_{\mathrm{BCF}}$) to[2]

$$G_{\mathrm{r}} = k_{\mathrm{BCF}} (S_{\mathrm{sat}} - 1). \tag{57}$$

In many modelling studies[28, 39, 130, 133], the following empirical form is often used which can be seen as kind of an intermediate between these two extreme cases:

$$G_{\mathrm{r}} = k_{\mathrm{g}} (S_{\mathrm{sat}} - 1)^n, \tag{58}$$

where k_{g} and n are empirical parameters.

In many cases, the growth rate has been observed to be dependent on crystal size, at least apparently. Ostwald ripening can explain the different growth rates only when the crystal size is small (less than 1 μm). For larger crystals such phenomenon could be explained by the increasing probability of surface dislocations as the particle surface becomes larger. However, in many cases these effects are negligible, and the apparent size dependency of growth rate is caused by a phenomenon known as the growth rate dispersion. This theory suggests that the growth rate of individual crystals exhibits a degree of randomness which stems from the probabilistic nature of the occurrence of dislocations. The number and the distribution of dislocations on the surfaces of the crystals can vary from crystal-to-crystal and may also change as the crystal experiences a collision or grows imperfectly. Thus, the growth rate predicted by the BCF theory will also exhibit changes.[31]

4.2.3. Aggregation and Breakage

In precipitation processes, aggregation can be an important factor in determining the shape of the resulting PSD. This is due to the high particle concentrations and small particle sizes typical to such processes.[2] The theories of colloid stability such as the DLVO theory form the theoretical basis of the discussion on aggregation and breakage, which were briefly treated in section 2.3. Aggregation can be incorporated in mathematical models by introducing an aggregation kernel β into the population balance equation which is essentially a measure of the frequency of collisions leading to aggregation. Since not every collision leads to aggregation, the aggregation kernel is often expressed as the product of aggregation probability, P_{A}, and collision kernel, β_{c}:[134]

$$\beta = P_{\mathrm{A}}\beta_{\mathrm{c}}. \tag{59}$$

The collision frequency is derived by considering the flow pattern of the reactor and the size of the involved particles in the system. Two types of collisions must be distinguished, which are ortho- and perikinetic collisions. Orthokinetic collisions are the impacts brought about by the turbulent shear forces whereas perikinetic collisions are the ones associated with the Brownian motion of the particles. As can be easily imagined, the magnitudes of the impact frequencies and the forces involved in these collisions can be quite different in magnitude and these collisions must thus be treated separately. The flow is practically always turbulent, which makes

the treatment rather laborious. The relative length- and timescales of the Brownian motion and turbulence must be considered in order to determine the appropriate form of the collision kernel. A detailed outline of derivation of the collision kernel is beyond the scope of this text and other sources should be consulted for further details.[38, 134]

The aggregates suspended in a precipitation reactor may experience large hydrodynamic or cavitation stresses caused by vigorous mixing and highly turbulent flow conditions. Thus, it is not a surprise that the formed aggregates may also disintegrate back into smaller fragments due to these forces. The actual mechanism through which this happens, depends on the structures of the aggregates and the types of forces involved. Breakage can be included in the process model by introducing a breakage kernel in a similar manner as was done for aggregation. Again, this is by no means a straightforward task and requires, for example, the evaluation of the magnitudes of the bonding forces in the aggregates, flow pattern of the system, and the magnitudes of the important stresses.[134]

After having determined the functional forms of the aggregation and breakage kernels, they can be introduced into the population balance [Eq. (16)] in the form of birth and death rate functions. It seems to be quite common that only an aggregation kernel is used, and breakage is neglected. Despite of this, the obtained results have been satisfying in many cases[38, 135]. To present an example of birth and death rate functions used in the literature, the simple expressions from a zinc sulfide precipitation study by Al-Tarazi et al. (2004)[39] are shown:

$$B = \frac{1}{2}\int_0^{V_2} \beta(V_1, V_2 - V_1) n(V_1, t) n(V_2 - V_1) \mathrm{d}V_1, \tag{60}$$

$$D = n(V_2)\int_0^{\infty} \beta(V_1, V_2) n(V_1) \mathrm{d}V_1, \tag{61}$$

where V_1 and $V_2 - V_1$ are the volumes of the colliding particles forming the aggregate, whose volume is then V_2, and $\beta(V_1, V_2 - V_1)$ is the aggregation kernel given by the empirical expression[39]

$$\beta(V_1, V_2 - V_1) = k_\beta G_\mathrm{r}^h J^p \tau^q, \tag{62}$$

where τ is the residence time (s), and k_β, h, p and q are empirical constants. Note that this equation assumes the aggregation kernel to be independent of particle size so β is now

essentially a constant with respect to V_1 and can be taken outside the integrals in Eqs. (60) and (61). In general, this is not the case, however, which is why the nature of β as a function of particle volumes has been emphasized by expressing it as $\beta(V_1, V_2 - V_1)$.

4.3. Mass Transfer

Through CFD calculations and practical experience it can be realized that the assumption of perfect mixing certainly does not apply to fast precipitation reactions carried out in large stirred-tank reactors frequently used in industrial scale processes. This heterogeneity leads to the development of zones of varying degrees of supersaturation and consequently, to very different conditions for precipitation. Thus, it is clear, that models able to describe the complex fluid mixing behavior in the various reactors are required. Nowadays, it is possible to model the complex flow patterns of systems with rather complicated geometries by employing CFD calculations with modern turbulence models.[136] However, there are practical limitations for the maximum density of the CFD calculation grid, since calculation times easily become unpractical as the grid is thickened. This means that the hydrodynamic conditions on the molecular scale (i.e. micromixing conditions), cannot be reached by means of direct CFD simulation. The information on heterogeneity caused by mixing on this scale is, however, crucial to model processes such as fast chemical reactions, nucleation and crystal growth accurately, since the time- and length scales for these processes are close to that of micromixing.[134] In other words, the assumption of homogeneity of a single grid element is often false and a so-called micromixing model must be applied to account for the unsteady molecular diffusion induced by turbulent mixing.[2, 128]

To simplify the mathematical treatment of the mixing phenomena, the process of mixing can be divided into three stages: macro- meso- and micromixing, each having their own characteristic time- and length scales. Macromixing is driven by the large-scale motions of groups of fluid elements and can be described with streamlines extending throughout the whole system. Macromixing can be modelled with CFD calculations, and it sets the general concentration environment for meso- and micromixing. Mesomixing is mixing on a scale smaller than the characteristic length of the system (e.g. reactor diameter) but larger than the microscale, where viscous- and molecular diffusion become important. Mesomixing driven by turbulent diffusion can be important in the development of a reactant plume near the inlet port,

for example. Micromixing comprises the mixing happening on the smallest scales of motion, where diffusion is the principal mechanism of mass transfer. Micromixing is the most important level of mixing for fast chemical reactions such as sulfide precipitation, since micromixing conditions set the surface area available for molecular diffusion, which in turn determines the reaction rate if diffusion is the limiting step. Micromixing takes place through the deformation of fluid elements due to viscous forces, followed by molecular diffusion.[137, 138]

An important point to note is that before any modelling attempts are made, it is advantageous to recognize the relevant timescales for the process in question. Timescale analysis as described for example, in Bałdyga (2016)[134] can be used to decide the scales on which modelling needs to be conducted and on which it is not required. For example, there is no reason to incorporate a micromixing model if, for some reason, the relevant reactions happen on much larger timescales than the timescales characteristic to micromixing.[134]

4.3.1. Micromixing Models

A detailed discussion on mixing models will not be attempted here, but due to the importance of micromixing for precipitation modelling, a few examples of simple micromixing models will be presented. In the model proposed by Baldyga and Bourne (1989)[139, 140] it is assumed that a fluid element draws mass from its environment through a process called engulfment which is driven by the elongation of microscale fluid vortices. In their paper they show that the more general but complex engulfment-deformation-diffusion (EDD) model can be substantially simplified provided that $\mathrm{Sc} \ll 4000$ and that the conditions are such that more than two vortex generations are required to mix the two fluids completely. Taking into account self-engulfment (i.e. engulfment that doesn't lead into a reaction) and the possible rate of appearance (or consumption), r_i, of the substance i through a chemical reaction within the fluid element, this model can be summarized with the following equations:[138]

$$\frac{\mathrm{d}V_i}{\mathrm{d}t} = E(1 - X_i)V_i, \tag{63}$$

$$\frac{\mathrm{d}c_i}{\mathrm{d}t} = E(1 - X_i)(\bar{c}_i - c_i) + r_i, \tag{64}$$

$$E = 0.05776(\varepsilon/\nu)^{1/2}, \tag{65}$$

where V_i is the volume of the fluid element containing component i, $\bar{c}_i$ is the average concentration of component i in the surrounding fluid elements, c_i is the concentration of component i in the fluid element in question, X_i is the volume fraction of fluid containing component i in the surroundings ($X_i \approx 1$ if the concentration of the other component is negligible with respect to $\bar{c}_i$ and $X_i \approx 0$ if the situation is converse) and E is an engulfment rate parameter that can be given in terms of the turbulent kinetic energy dissipation rate ε and kinematic viscosity ν. Eqs. (63) and (64) give the rates of change for the volume of the fluid element, and for the concentration of component i in the fluid element, respectively. The above model can be viewed as a theoretically justified form of the empirical equation called the interaction by exchange with the mean (IEM) model, which is given by[128, 138]

$$\frac{\mathrm{d}c_i}{\mathrm{d}t} = k_\mathrm{m}(\bar{c}_i - c_i) + r_i, \tag{66}$$

where k_m is an empirical rate constant that can be expressed as[128]

$$k_\mathrm{m} = C_\xi \frac{\varepsilon}{2k_\mathrm{turb}}, \tag{67}$$

where k_turb is the turbulent kinetic energy and C_ξ is a micromixing constant. Some authors have assigned a constant value of $C_\xi = 2.00$ or $C_\xi = 1.65$, but C_ξ has been shown to exhibit a strong dependency on Reynolds number. For example, Metzger & Kind (2017)[128] modelled this dependency with the following empirical equation:

$$C_\xi = C_{\xi,\max} \frac{(\mathrm{Re_T})^n}{A^n + (\mathrm{Re_T})^n}, \tag{68}$$

where $C_{\xi,\max} = 2.26638$, $A = 5.51115$, $n = 0.91242$ and $\mathrm{Re_T}$ is the turbulent Reynolds number given by:

$$\mathrm{Re_T} = \frac{\mathrm{k_{turb}}}{\sqrt{\varepsilon\nu}}. \tag{69}$$

Note that the IEM model does not take self-engulfment into account.[138]

4.4. Time Dependent Modelling of Sulfide Precipitation Processes

The most comprehensive approach to construct time dependent models for precipitators would be to simultaneously solve the population balance equation and the flow field for the reactor with the aid of CFD. This is, however, easier said than done since neither the population balance nor the transport equations needed to describe the fluid flow can be solved analytically for all except the simplest cases. Thus, there are many studies[20, 39, 131, 141, 142] that do not incorporate fluid dynamics at all and rely on the more or less false assumption of perfect mixing. Although the information attained by such simplified models may not be very detailed or accurate, it can be enough for practical applications where rough estimates are sufficient. Such models may be useful to develop simple process monitoring and control strategies, for example.[125, 141, 142]

Two approaches have, however, been adopted among researchers to overcome the computational difficulties. The first approach is to combine accurate CFD modelling with a simple precipitation model whereas the other approach uses separate CFD calculation to obtain generalized flow parameters which are then subsequently used to solve the population balance equation. A rather severe limitation of the former is, that due to the overly simplified precipitation model, the particle size distribution cannot be predicted accurately whereas the latter method suffers from the loss of local information (e.g., distribution of concentrations or fluid velocities) of the conditions in the reactor due to the generalization of the flow parameters. The advantage of the latter method is that a more advanced precipitation model including equations for e.g., nucleation, growth rate and agglomeration can be relatively easily included due to the decreased computational complexity.[136]

4.4.1. Models for Automated Process Control

A few studies aimed to develop means for the automated control of sulfide precipitation have been conducted at least for the continuous stirred tank reactor (CSTR) precipitating zinc sulfide.[125, 141, 142] The basic idea is to use only input parameters such as pH, pS and flow rate that can be readily monitored in an industrial facility. The difficulty is to construct a sufficiently accurate relation between these few variables and the output concentrations of the important species since precipitation is an extremely complex process that depends on a rather large number of factors.

Grootscholten et al. (2008)[125] presented a so-called unknown input observer algorithm that can predict the resulting zinc and total sulfide concentrations in the effluent of a CSTR using only pS and pH electrode readings as model inputs. Naturally, other process conditions, such as the initial concentrations of the reagents and feed flow rates must be specified also. Their model is essentially a reduced form of the model originally outlined by König et al. (2005)[141], which in turn was based on mass balances for zinc and total sulfide. In this model, zinc sulfide precipitation was expressed as an irreversible second-order reaction. König and co-workers noted that the rate constant depended greatly on feed flow rates. As stated in a third similar paper by Sampaio et al (2009)[142], this results from the fact that the "rate constant" is merely a parameter into which many effects such as those caused by imperfect mixing and parallel reactions have been lumped. Grootscholten et al. provided a method to roughly estimate this "rate constant" continuously from the observer data (which are also estimates). Their observer algorithm was demonstrated to be able to deal with disturbances in the initial concentration of zinc and could also quite accurately estimate the zinc and total sulfide concentrations from the data of a real-world experiment, where the objective had been to maintain pS at 15. The results suggested that the presented approach could be suitable in automatic on-line control of zinc sulfide precipitation.

However, there are some further limitations to this approach that should be mentioned. For example, these models do not consider hydroxide formation and are thus limited to pH values lower than 7. All three research groups also mentioned that the model outputs were greatly affected by small variations in inputted flow rates and initial concentrations, which places demanding requirements for their measurement accuracy.[125, 141, 142] Sampaio et al. (2009)[142] demonstrated that it can be advantageous to eliminate the error resulting from the high uncertainty of the Zn measurement by treating the initial Zn concentration as unknown instead of the "rate constant" which is then expressed as a function of pS. The actual form of this function must be determined experimentally.

4.4.2. Applying the Population Balance to Sulfide Precipitation

Studies utilizing only population balance without any mixing models or CFD modelling naturally assume prefect mixing and thus ignore any effects brought about by heterogenous flow

conditions. Thus, the information provided by such experiments may not be very detailed or accurate but may still provide valuable insight or useful empirical relations.

Veeken et al. (2003)[20] used the simple population balance [Eq. (18)] for the MSMPR reactor to model the PSD of the resulting precipitate and to derive empirical expressions for nucleation rate, growth rate and aggregation kernel for a zinc sulfide precipitation process. They used a sulfide selective electrode and a thermodynamic speciation model to calculate the supersaturation levels for the conditions of their experiments. Eq. (18) was fitted to the experimentally obtained PSDs and the resulting R^2 values for 7 experiments ranged from 0.833 to 0.998 demonstrating that their system could be adequately modelled by the simple MSMPR formalism. For two experiments, the Zn concentration was below the detection limit and supersaturation levels for these experiments could not be calculated. With the aid of a LiCl tracer they observed that the macromixing in the reactor was essentially perfect. Note that the perfectness of mixing on the microscale cannot be assured by this visual observation. Imperfect mixing probably explains at least some of the observed deviations from the ideal MSMPR model.[20]

Al-Tarazi et al. (2004)[39] also used the population balance equation to study the kinetics of a MSMPR-reactor for zinc sulfide precipitation. As in the formerly mentioned study these authors also recorded the experimental PSDs and fitted simple empirical equations for nucleation rate, growth rate and aggregation kernel. The obtained fit qualities were moderate at best, which gives some indication that the MSMPR assumptions were not perfectly satisfied and/or the empirical expressions are of incorrect form to model zinc sulfide precipitation. Despite the lack of quantitative accuracy, the model was able to qualitatively explain the general trends in nucleation rate, growth rate and aggregation kernel with respect to supersaturation.[39]

In another study by Al-Tarazi et al. (2004)[131] a theoretical model for the precipitation of copper and zinc by $H_2S(g)$ was developed. The simulation conditions were selected to resemble those of the wastewater of an industrial zinc producer. The system was assumed to consist of a homogenous gas phase in contact with a solution composed of a well-mixed bulk and a boundary layer. The model equations were mass balances written for a total of 9 species, an electroneutrality equation, and a population balance. Higbie's penetration theory was applied to model the mass transfer of hydrogen sulfide through the gas-liquid interface. The values for the various constants, such as diffusion constants, rate constants and equilibrium constants required

by the model were extracted from literature. Some reactions were assumed fast, and their rate constants were assigned arbitrary high values. Population balance was used to incorporate equations for the nucleation and growth of the metal sulfide particles. From the model output, relations such as the concentration profiles of the various species across the boundary layer (or fluid packages), mean particle sizes of the precipitates and the bulk concentrations of the metals as functions of time, pH and $H_2S(g)$ concentration could be obtained to name a few examples. Their model also predicted that the rate of precipitation was limited solely by the transfer of $H_2S(g)$ from the gas to the solution phase. It is noteworthy that the authors did not present any experimental data to validate their model so the predictive capabilities of the model could not be assessed, and the model should be used to give tentative guidelines only.[131]

4.4.3. CFD Modelling of Sulfide Precipitation Systems

It seems that only a couple of studies incorporating hydrodynamics with the aid of CFD calculations have appeared in the field of sulfide precipitation.[6, 126] To my knowledge, none of the present studies on sulfide precipitation systems incorporate both population balance, and CFD modelling. Such studies are, however, available for other systems with other precipitates, of which the most common one is barium sulfate $BaSO_4$.[30, 38, 128-130, 135]

Yang et al. (2019)[126] designed and evaluated three different geometries for tubular continuous copper sulfide precipitators with the aid of CFD modelling. Copper sulfide precipitation was modelled as a simple irreversible second-order reaction. For turbulence modelling, the authors used the k-ε turbulence model. This widely used model introduces transport equations for turbulent kinetic energy, k_{turb}, and kinetic energy dissipation rate, ε, which together with the transport equations for mass and momentum comprise a closed set of equations that can be solved numerically.[121, 143] Note that temperature was not included as a variable in the model and thus the transport equation for energy was not needed. A separate wall function was adopted to model the flow in the viscous layer near the reactor walls. The model could successfully predict the concentration of copper in the effluent of all three reactors as a function of time after startup. Significant differences were observed in the times required to reach a steady-state, and in copper concentrations in the effluent among the three studied reactor geometries. The most efficient reactor layout was such, that two Na_2S inlets were located at opposite sides near the top of the reactor and the wastewater inlet and outlet were located at the top and bottom respectively.

Population balance was not considered and thus no information about the PSD could be obtained with this model. Despite of this, the results provide an excellent example of the power of CFD in developing models for sulfide precipitation systems even without the population balance or detailed information about the precipitation kinetics.

In a similar study by the same group[6], a time dependent model for batch copper sulfide precipitation with H_2S (g) was developed. The modelled reactor was a small cylinder with H_2S aerator located at the bottom. Otherwise, the modelling approach was based on the transport equations for mass and momentum accompanied with the k-ε turbulence model as in the preceding study, but now the presence of two phases had to be considered. To do this they used a two-phase macroscopic Euler-Euler model with the assumptions that the density of the gas was negligible compared to that of the liquid, the gas occupied only a small volume fraction, the phases always travelled with their terminal velocity and that both phases shared the same pressure field. They also assumed that the mass transfer rate of H_2S from the gas to the liquid phase was given by[6]

$$\frac{\mathrm{d}(w_{\mathrm{H_2S}})}{\mathrm{d}t} = k_{\mathrm{H_2S}}\left(c_{\mathrm{H_2S,eq}} - c_{\mathrm{H_2S}}\right)M_{\mathrm{H_2S}}\frac{A_{\mathrm{b}}}{V}, \tag{70}$$

where $k_{\mathrm{H_2S}}$ is an empirical gas-liquid mass transfer coefficient, $c_{\mathrm{H_2S,eq}}$ is the equilibrium concentration of H_2S in the liquid phase as given by Henry's law, $M_{\mathrm{H_2S}}$ is the molar mass of H_2S, A_{b} is the gas liquid contact area and V is the volume of the liquid phase. The simulation results were validated by performing a series of precipitation experiments and comparing the simulated and experimental copper concentrations as a function of operation time. The simulation results showed excellent agreement with the experimental data with all studied H_2S bubble sizes and flow rates. Again, no PSD modelling could be conducted due to the absence of population balance treatment, but the authors still provided experimental PSDs and compared the PSDs of the precipitates to those obtained from the earlier study with $Na_2S(aq)$. It was clear that using $Na_2S(aq)$ resulted in much smaller mean particle size due to the high local supersaturations that cannot be avoided in practice when using a solution or solid reagent. In the case of $H_2S(g)$ as the precipitation agent, the mass transfer from the gas to the liquid phase limits the rate of precipitation which can prevent the local supersaturation from reaching extremely high levels. The simulation results showed that the supersaturation levels in the

studied reactor were 4–5 orders of magnitude smaller than in the previous reactors using $Na_2S(aq)$.[6]

5. SUMMARY AND CONCLUDING WORDS

In the preceding chapters, the physico-chemical phenomena behind sulfide precipitation processes were discussed. In the first two chapters, an introduction to the basic concepts of precipitation and crystallization science was given. The definition of supersaturation was outlined, followed by a brief introduction to the classical crystallization theory and to the surface chemistry of suspended particles. Finally, some discussion was devoted to the chemistry of polysulfides and metal sulfide complexes.

In chapter 3 sulfide precipitation was approached from the viewpoint of thermodynamics. A compilation of the values for the solubility products of selected metal sulfides was given, and different approaches for the modelling of the solubilities of metal sulfides were outlined. The extensively used method of deriving equilibrium constants from solubility data was discussed in some detail and a few such solubility models found in the literature were presented. The application of voltammetry to the determination of equilibrium constants was briefly addressed. Also, some discussion was devoted to the issues in the reliability of thermodynamic data. Another important topic of this chapter was the construction and usage of Eh – pH diagrams for metal sulfide systems. The principles and assumptions behind these diagrams and the limitations imposed by them were discussed. Eh – pH diagrams for four element (Me-S-O-H) systems were constructed using the HSC Chemistry® 10 process modelling platform. Finally, the application of thermodynamics to real sulfide precipitation systems was illustrated through a couple of examples from the literature.

The review of the metal sulfide literature showed that although substantial advances have been made, there are significant discrepancies in the values of many important thermodynamic quantities, such as the solubility products of metal sulfides. At worst, the deviations in the values are several orders of magnitude. The solubility predictions obtained by commercial thermodynamic software can be off even 20 orders of magnitude due to the inaccuracies or the complete lack of data for important solubility controlling species. Thus, there is an urgent need for reliable thermodynamic data on these species. Studies aiming to identify the potentially important species in sulfide precipitation processes and those concentrating on the accurate determination of the thermodynamic properties of these species could add considerable value to this field.

In chapter 4 the emphasis was on the dynamic modelling of metal sulfide precipitation with some consideration of the hydrodynamics as well. The general approach to construct dynamic models for precipitation systems was outlined and some example studies from the field were presented. The potential of combining the population balance with CFD calculations to model sulfide precipitation systems was recognized, but no studies implementing this approach to sulfide precipitation systems were found in the current literature.

In general, the literature for metal sulfide systems on this field was found to be relatively scarce and it is apparent that much work remains to be done. Especially, studies aiming to develop accurate dynamic models for sulfide precipitation reactors by combining CFD calculations with the population balance approach could be a valuable addition to this field.

6. REFERENCES

1. Eckenfelder W. W., Ford D. L. & Englande A. J., *Industrial water quality,* McGraw-Hill, **2009**.

2. Karpinski P. H. & Wey J. S., *Precipitation processes,* in: *Handbook of industrial crystallization:* Ed. Myerson A., Butterworth-Heinemann, **2002**.

3. Lewis A. E., *Hydrometallurgy,* **2010***, 104*(2), 222-234.

4. Prokkola H., Nurmesniemi E. & Lassi U., *ChemEngineering,* **2020***, 4*(3), 51.

5. Kumar M., Nandi M. & Pakshirajan K., *J. Environ. Manage.,* **2021***, 278*, 111555.

6. Zeng W., Guo W., Li B., Wei Z., Dionysiou D. D. & Xiao R., *J. Hazard. Mater.,* **2021***, 408*, 124868.

7. Suleimenov O. M. & Seward T. M., *Geochim. Cosmochim. Acta,* **1997***, 61*(24), 5187-5198.

8. Migdisov A., Williams-Jones A., Lakshtanov L. & Victorovich A., *Geochim. Cosmochim. Acta,* **2002***, 66*, 1713-1725.

9. Luther G. W., Theberge S. M. & Rickard D. T., *Geochim. Cosmochim. Acta,* **1999***, 63*(19), 3159-3169.

10. Shea D. & Helz G. R., *Geochim. Cosmochim. Acta,* **1988***, 52*(7), 1815-1825.

11. Sun W., Nešić S., Young D. & Woollam R., *Ind. Eng. Chem. Res.,* **2008***, 47*, 1738-1742.

12. May P. M., Batka D., Hefter G., Königsberger E. & Rowland D., *Chem. Commun.,* **2018***, 54*(16), 1980-1983.

13. Kim S., Marrs C., Nemer M. & Je-Hun Jang J., *ACS Earth Space Chem.,* **2017***, 1*(10), 647-663.

14. Powell K. J., Brown P. L., Byrne R. H., Gajda T., Hefter G., Sjöberg S. et al., *Pure Appl. Chem.,* **2005***, 77*(4), 739-800.

15. Powell K. J., Brown P. L., Byrne R. H., Gajda T., Hefter G., Sjöberg S. et al., *Pure Appl. Chem.,* **2007***, 79*(5), 895-950.

16. Powell K. J., Brown P. L., Byrne R. H., Gajda T., Hefter G., Leuz A. et al., *Pure Appl. Chem.,* **2009***, 81*(12), 2425-2476.

17. Powell K. J., Brown P. L., Byrne R. H., Gajda T., Hefter G., Leuz A. et al., *Pure Appl. Chem.,* **2011***, 83*(5), 1163-1214.

18. Powell K. J., Brown P. L., Byrne R. H., Gajda T., Hefter G., Leuz A. et al., *Pure Appl. Chem.,* **2013***, 85*(12), 2249-2311.

19. Lewis A. E. & van Hille R. P., *Hydrometallurgy,* **2006***, 81*(3), 197-204.

20. Veeken A. H. M., Akoto L., Hulshoff Pol L. W. & Weijma J., *Water Res.,* **2003***, 37*(15), 3709-3717.

21. Rickard D. T. & Luther G. W., *Reviews in mineralogy and geochemistry,* **2006***, 61*(1), 421-504.

22. van Hille R. P., Peterson K. A. & Lewis A. E., *Chem. Eng. Sci.,* **2005***, 60*(10), 2571-2578.

23. Wang L. K., Vaccari D. A., Li Y. & Shammas N. K., *Chemical precipitation,* in: *Physicochemical treatment processes:* Ed. Wang L. K., Hung Y. & Shammas N. K., Humana Press, **2005**.

24. Soya K., Mihara N., Kuchar D., Kubota M., Matsuda H. & Fukuta T., *Engineering and Technology,* **2008***, 44*, 356-360.

25. Ivan V. M., *Crystal growth for beginners: Fundamentals of nucleation, crystal growth and epitaxy (2nd edition),* World Scientific, **2003**.

26. Kashchiev D. & van Rosmalen G. M., *J. Colloid Interface Sci.,* **1995***, 169*(1), 214-219.

27. Baillon F., Espitalier F., Cogné C., Peczalski R. & Louisnard O., *Crystallization and freezing processes assisted by power ultrasound,* in: *Power ultrasonics:* Ed. Gallego-Juárez J. A. & Graff K. F., Woodhead Publishing, **2015**.

28. Garside J., *Chem. Eng. Sci.,* **1985***, 40*(1), 3-26.

29. Mersmann A., *Crystallization technology handbook,* CRC Press, **2001**.

30. Schwarzer H. & Peukert W., *AIChE J.,* **2004***, 50*(12), 3234-3247.

31. Myerson A. & Ginde R., *Crystals, crystal growth, and nucleation,* in: *Handbook of industrial crystallization:* Ed. Myerson A., Butterworth-Heinemann, **2002**.

32. Gebauer D., Kellermeier M., Gale J. D., Bergström L. & Cölfen H., *Chem. Soc. Rev.,* **2014***, 43*(7), 2348-2371.

33. Atkins P. & De Paula J., *Atkins' physical chemistry,* Oxford University Press, **2014**.

34. Wright K., Watson G. W., Parker S. C. & Vaughan D. J., *American Mineralogist,* **1998***, 83*(1-2), 141-146.

35. Vekilov P. G., *Nanoscale,* **2010***, 2*(11), 2346-2357.

36. Randolph A. D. & Larson M. A., *Theory of particulate processes,* Academic Press, **1988**.

37. Berglund K. A., *Analysis and measurement of crystallization utilizing the population balance,* in: *Handbook of industrial crystallization:* Ed. Myerson A., Butterworth-Heinemann, **2002**.

38. Schwarzer H., Schwertfirm F., Manhart M., Schmid H. & Peukert W., *Chem. Eng. Sci.,* **2006***, 61*(1), 167-181.

39. Al-Tarazi M., Heesink A. B., Azzam M. O. J., Yahya S. A. & Versteeg G. F., *Cryst. Res. Technol.,* **2004***, 39*(8), 675-685.

40. Kashchiev D., *J. Chem. Phys.,* **2008***, 129*(16), 164701.

41. Rieger J., Frechen T., Cox G., Heckmann W., Schmidt C. & Thieme J., *Faraday Discuss.,* **2007***, 136*, 265-277.

42. Andreassen J. & Lewis A. E., *Classical and nonclassical theories of crystal growth,* in: *New perspectives on mineral nucleation and growth:* Ed. Van Driessche, A. E. S., Kellermeier M., Benning L. G. & Gebauer D., Springer, **2017**.

43. Hunter R. J., *Foundations of colloid science,* Oxford University Press, **2001**.

44. Tadros T. F., *Basic principles of interface science and colloid stability,* De Gruyter, **2018**.

45. Barnes G. & Gentle I., *Interfacial science: An introduction,* Oxford University Press, **2011**.

46. Mokone T. P., Lewis A. E. & van Hille R. P., *Hydrometallurgy,* **2012***, 119-120*, 55-66.

47. Delgado A. V., González-Caballero F., Hunter R. J., Koopal L. K. & Lyklema J., *J. Colloid Interface Sci.,* **2007***, 309*(2), 194-224.

48. Jagannathan R. & Wey J. S., *J. Cryst. Growth,* **1981***, 51*(3), 601-606.

49. Alemán J. V., Chadwick A. V., He J., Hess M., Horie K., Jones R. G. et al., *Pure Appl. Chem.,* **2007***, 79*(10), 1801-1829.

50. Verwey E. J. W., Overbeek J. T. G. & van Nes K., *Theory of the stability of lyophobic colloids; the interaction of sol particles having an electric double layer,* Elsevier, **1948**.

51. Derjaguin B. & Landau L., *Acta Physico Chimica USSR,* **1941***, 14*, 633.

52. Giggenbach W., *Inorg. Chem.,* **1972***, 11*(6), 1201-1207.

53. Bedoya-Lora F. E., Hankin A. & Kelsall G. H., *Electrochim. Acta,* **2019***, 314*, 40-48.

54. Helz G. R., *Geochem. T.,* **2014***, 15*(1), 13.

55. Kamyshny A., Goifman A., Gun J., Rizkov D. & Lev O., *Environ. Sci. Technol.,* **2004***, 38*(24), 6633-6644.

56. Roine. A, HSC Chemistry® [Software], Metso Outotec, Pori 2021, Software available at www.mogroup.com/hsc, Retriewed: May 6, 2021.

57. Chadwell S. J., Rickard D. T. & Luther G. W., *Aquat. Geochem.,* **1999***, 5*(1), 29-57.

58. Chadwell S. J., Rickard D. T. & Luther G. W., *Electroanalysis,* **2001***, 13*(1), 21-29.

59. Cloke P. L., *Geochim. Cosmochim. Acta,* **1963***, 27*(12), 1265-1298.

60. Luther G. W. & Rickard D. T., *J. Nanopart. Res.,* **2005***, 7*(4), 389-407.

61. Theberge S. M. & Luther G. W., *Aquat. Geochem.,* **1997***, 3*, 191-211.

62. Luther G. W., Theberge S. M. & Rickard D. T., *Geochim. Cosmochim. Acta,* **1999***, 63*(19), 3159-3169.

63. Daskalakis K. D. & Helz G. R., *Geochim. Cosmochim. Acta,* **1993***, 57*(20), 4923-4931.

64. Rickard D. T., *Geochim. Cosmochim. Acta,* **2006***, 70*(23), 5779-5789.

65. Davison W., Phillips N. & Tabner B. J., *Aquat. Sci.,* **1999***, 61*(1), 23-43.

66. Zemaitis J. F., Clark D. M., Rafal M. & Scrivner N. C., *Handbook of aqueous electrolyte thermodynamics,* American Institute of Chemical Engineers, **1986**.

67. Myers R. J., *J. Chem. Educ.,* **1986***, 63*(8), 687.

68. Licht S., *J. Electrochem. Soc.,* **1988***, 135*(12), 2971-2975.

69. Clever H. L., Derrick M. E. & Johnson S. A., *J. Phys. Chem. Ref. Data,* **1992***, 21*(5), 941-1004.

70. Murcia D. C. F., Fosbøl P. L., Thomsen K. & Stenby E. H., *J. Solution Chem.,* **2017***, 46*(9), 1805-1817.

71. Barrett T. J. & Anderson G. M., *Geochim. Cosmochim. Acta,* **1988***, 52*(4), 813-820.

72. Figueroa Murcia D. C., Fosbøl P. L., Stenby E. H. & Thomsen K., *Fluid Phase Equilib.,* **2018***, 475*, 118-126.

73. Van Hövell Tot Westerflier, S. W. F. M., Binsma J. J. M., Stein H. N. & Vandecasteele C., *J. Radioanal. Nucl.,* **1987***, 111*(2), 305-317.

74. Davison W., *Aquat. Sci.,* **1991***, 53*(4), 309-329.

75. Ball J. W. & Nordstrom D. K., **1991***, User's Manual for WATEQ4F, with Revised Thermodynamic Data Base and Text Cases for Calculating Speciation of Major, Trace, and Redox Elements in Natural Waters,* U.S. Geological Survey.

76. Benning L., Wilkin R. & Barnes H., *Chem. Geol.,* **2000***, 167*, 25-51.

77. Lemire R. J., Berner U., Musikas C., Palmer D. A., Taylor P. & Tochiyama O., **2013***, Chemical Thermodynamics of Iron - Part 1 - Chemical Thermodynamics Volume 13a,* Nuclear Energy Agency of the OECD (NEA).

78. Martell A. E. & Smith R. M., *Critical stability constants. vol. 4: Inorganic complexes,* Plenum, **1976**.

79. Bowers T. S., Jackson K. J. & Helgeson H. C., *Equilibrium activity diagrams: For coexisting minerals and aqueous solutions at pressures and temperatures to 5 kb and 600 °C,* Springer, **1984**.

80. Daskalakis K. D. & Helz G. R., *Environ. Sci. Technol.,* **1992***, 26*(12), 2462-2468.

81. Uhler A. D. & Helz G. R., *Geochim. Cosmochim. Acta,* **1984***, 48*(6), 1155-1160.

82. Nims L. F. & Bonner W. D., *J. Phys. Chem.,* **1929***, 33*(4), 586-590.

83. Shea D. & Helz G. R., *Geochim. Cosmochim. Acta,* **1989***, 53*(2), 229-236.

84. Hayashi K., Sugaki A. & Kitakaze A., *Geochim. Cosmochim. Acta,* **1990***, 54*(3), 715-725.

85. Davies C. W., *J. Chem. Soc.,* **1938**, 2093-2098.

86. Mountain B. W. & Seward T. M., *Geochim. Cosmochim. Acta,* **1999***, 63*(1), 11-29.

87. Olsen N. J., Mountain B. W. & Seward T. M., *ACS Earth Space Chem.,* **2019***, 3*(6), 1058-1072.

88. Benoit J. M., Gilmour C. C., Mason R. P. & Heyes A., *Environ. Sci. Technol.,* **1999***, 33*(6), 951-957.

89. Krupp R. E., *Geochim. Cosmochim. Acta,* **1988***, 52*(12), 3005-3015.

90. Helz G. R. & Tossell J. A., *Geochim. Cosmochim. Acta,* **2008***, 72*(18), 4457-4468.

91. Lacour S., van Hille R. P., Peterson K. & Lewis A. E., *AIChE J.,* **2005**, *51*(8), 2358-2368.

92. *MINTEQA2/PRODEFA2, A geochemical assessment model for environmental systems:User manual supplement for version 4.0,* HydroGeoLogic, Inc. & Allison Geoscience Consultants, Inc., **1999**.

93. MINEQL+ Chemical Equilibrium Modeling System, Environmental Research Software, https://mineql.com/Overview.html, Retriewed: June 23, 2021.

94. OLI Studio: Stream Analyzer, OLI Systems, Inc, https://www.olisystems.com/oli-studio-stream-analyzer, Retriewed: June 23, 2021.

95. Aspen Plus®, Aspen Technology, Inc, https://www.aspentech.com/en/products/engineering/aspen-plus, Retriewed: June 23, 2021.

96. Luther G. W. & Ferdelman T. G., *Environ. Sci. Technol.,* **1993**, *27*(6), 1154-1163.

97. Harvey D., *Analytical chemistry 2.1,* **2019**.

98. DeFord D. D. & Hume D. N., *J. Am. Chem. Soc.,* **1951**, *73*(11), 5321-5322.

99. DIPPR's Project 801 Database, Design Institute for Physical Properties, https://www.aiche.org/dippr, Retriewed: May 6, 2021.

100. FREED® - Thermodynamic Database, ThermarT, https://www.thermart.net/, Retriewed: May 6, 2021.

101. FactSage®, CRCT-ThermFact Inc. and GTT-Technologies, https://www.factsage.com/, Retriewed: May 6, 2021.

102. Nordstrom D., Plummer L., Langmuir D., Busenberg E., May H., Jones B., et al., *Revised chemical equilibrium data for major Water—Mineral reactions and their limitations,* in: *Chemical modeling of aqueous systems II:* Ed. Melchior D. C. & Bassett R. L., American Chemical Society, **1990**.

103. Parker V. B. & Khodakovskii I. L., *J. Phys. Chem. Ref. Data,* **1995**, *24*(5), 1699-1745.

104. Pitzer K. S., Brewer L., Lewis G. N. & Randall M., *Thermodynamics,* McGraw-Hill, **1961**.

105. Gamsjäger H., Lorimer J. W., Scharlin P. & Shaw D. G., *Pure Appl. Chem.,* **2008**, *80*(2), 233-276.

106. Brookins D. G., *Eh-pH diagrams for geochemistry,* Springer Berlin Heidelberg, **1988**.

107. Huang H., *Metals,* **2016**, *6*(1).

108. Patel A. M., Nørskov J. K., Persson K. A. & Montoya J. H., *Phys. Chem. Chem. Phys.,* **2019***, 21*(45), 25323-25327.

109. Persson K. A., Waldwick B., Lazic P. & Ceder G., *Phys. Rev. B,* **2012***, 85*(23), 235438.

110. Takeno N., **2005***, Atlas of Eh-pH Diagrams Intercomparison of Thermodynamic Databases,* National Institute of Advanced Industrial Science and Technology.

111. Bromley L. A., *AIChE J.,* **1973***, 19*(2), 313-320.

112. Pitzer K. S., *J. Phys. Chem.,* **1973***, 77*(2), 268-277.

113. Thompson W. T., Kaye M. H., Bale C. W. & Pelton A. D., *Pourbaix diagrams for multielement systems,* in: *Uhlig's corrosion handbook, second edition:* Ed. Winston R., John Wiley & Sons, Inc., **2000**.

114. Anderko A. & Shuler P. J., *Comput. Geosci.,* **1997***, 23*(6), 647-658.

115. Wei D. & Osseo-Asare K., *Colloids Surf. Physicochem. Eng. Aspects,* **1996***, 118*(1), 51-61.

116. Liu Y., Zhang Z., Bhandari N., Dai Z., Yan F., Ruan G. et al., *Ind. Eng. Chem. Res.,* **2017***, 56*(31), 9016-9027.

117. Rumble J. R., *CRC handbook of chemistry and physics,* CRC Press, **2020**.

118. Helz G. R., Valerio M. S. & Capps N. E., *Environ. Sci. Technol.,* **2002***, 36*(5), 943-948.

119. Couture R. & Van Cappellen P., *J. Hazard. Mater.,* **2011***, 189*(3), 647-652.

120. Shakeri Yekta S., Svensson B. H., Björn A. & Skyllberg U., *Appl. Geochem.,* **2014***, 47*, 61-73.

121. Munson B. R., Rothmayer A. P., Okiishi T. H. & Huebsch W. W., *Fluid mechanics: International student version,* Wiley, **2013**.

122. Chung T. J., *Computational fluid dynamics,* Cambridge University Press, **2010**.

123. Rickard D. T., *Geochim. Cosmochim. Acta,* **1995***, 59*(21), 4367-4379.

124. Rickard D. T., *Chem. Geol.,* **1989***, 78*, 315-324.

125. Grootscholten T., Keesman K. & Lens P., *Sep. Purif. Technol.,* **2008***, 63*(3), 654-660.

126. Yang Z., Li B., Zeng W., Li K., Liu S., Hu H. et al., *Environ. Sci. Pollut. R.,* **2019***, 26*(33), 34531-34551.

127. Zieliński J., Huculak-Mączka M., Kaniewski M., Nieweś D., Hoffmann K. & Hoffmann J., *Hydrometallurgy,* **2019***, 190*, 105157.

128. Metzger L. & Kind M., *Chem. Eng. Sci.,* **2017***, 169*, 284-298.

129. Wei H. & Garside J., *Chem. Eng. Res. Des.,* **1997***, 75*(2), 219-227.

130. Wei H., Zhou W. & Garside J., *Ind. Eng. Chem. Res.,* **2001***, 40*(23), 5255-5261.

131. Al-Tarazi M., Heesink A. B. & Versteeg G. F., *Chem. Eng. Sci.,* **2004***, 59*(3), 567-579.

132. Burton W. K., Cabrera N., Frank F. C. & Mott N. F., *Philos. T. R. Soc. S-A,* **1951***, 243*(866), 299-358.

133. Veeken A. H. M. & Rulkens W. H., **2003***, Innovative Developments in the Selective Removal and Reuse of Heavy Metals from Wastewaters,* IWA, London, 9-16.

134. Bałdyga J., *KONA Powder Part. J.,* **2016***, 33*, 127-149.

135. Paschedag A. R., *Chem. Eng. Technol.,* **2004***, 27*(3), 232-236.

136. Kagoshima M. & Mann R., *Chem. Eng. Sci.,* **2005***, 60*(8-9), 2155-2165.

137. Paul E. L., Atiemo-Obeng V. A. & Kresta S. M., *Handbook of industrial mixing: Science and practice,* Wiley, **2004**.

138. Bałdyga J. & Pohorecki R., *Chem. Eng. J. Bioch. Eng.,* **1995***, 58*(2), 183-195.

139. Bałdyga J. & Bourne J. R., *Chem. Eng. J.,* **1989***, 42*(2), 83-92.

140. Bałdyga J. & Bourne J. R., *Chem. Eng. J.,* **1989***, 42*(2), 93-101.

141. König J., Keesman K. J., Veeken A. H. M. & Lens P. N. L., *Sep. Sci. Technol.,* **2006***, 41*(6), 1025-1042.

142. Sampaio R. M. M., Keesman K. J. & Lens P. N. L., *Sep. Sci. Technol.,* **2009***, 44*(8), 1675-1703.

143. Scott-Pomerantz C. D. **2004***, The k-epsilon model in the theory of turbulence,* University of Pittsburgh.

7. APPENDICES

APPENDIX A: List of species for the Eh – pH diagrams

In the following tables, the Gibbs free energy of formation data used in the generation of the Eh – pH diagrams presented in this work is given. The data has been taken from the HSC-Chemistry® 10 database[56]. Species that have been excluded from the metastable diagrams presented in section 3.5 have been shaded.

Table A1. Sulfur species

Species	$\Delta_f G^0$ kJ/mol
S	0.000
S(M)	0.083
H2S(a)	-27.763
SO2(a)	-300.555
SO3(a)	-525.637
HS(-a)	12.160
HS2(-a)	11.506
HS3(-a)	20.510
HS4(-a)	27.714
HS5(-a)	33.017
HS6(-a)	36.228
HSO3(-a)	-527.613
HSO4(-a)	-755.312
S2(-2a)	79.727
S3(-2a)	73.878
S4(-2a)	69.408
S5(-2a)	66.194
S6(-2a)	66.221
SO3(-2a)	-486.546
SO4(-2a)	-744.361
S2O3(-2a)	-518.647
S2O4(-2a)	-600.567
S2O5(-2a)	-790.876
S2O6(-2a)	-969.037
S3O6(-2a)	-957.360
S4O6(-2a)	-1040.253

S(M) Monoclinic sulfur

Table A2. Zn species

Species	$\Delta_f G^0$ kJ/mol
Zn(FCC)	1.776
Zn(HCP)	0.000
ZnO	-318.150
ZnO(RS)	-297.237
Zn(OH)2	-555.918
ZnO*2ZnSO4	-2067.683
ZnS	-198.516
ZnS(B)	-200.400
ZnS(W)	-188.201
ZnSO4	-868.741
ZnSO4*H2O	-1132.013
ZnSO4*2H2O	-1370.023
ZnSO4*6H2O	-2324.173
ZnSO4*7H2O	-2562.314
Zn(HS)2(a)	-179.001
ZnO(a)	-274.957
ZnS(a)	-61.725
HZnO2(-a)	-460.830
Zn(+2a)	-147.252
ZnHS(+a)	-184.889
Zn(HS)3(-a)	-187.113
Zn(HS)4(-2a)	-181.458
Zn(HS)2OH(-a)	-379.486
ZnO2(-2a)	-390.269
ZnOH(+a)	-334.887
Zn(OH)3(-a)	-705.509
Zn(OH)4(-2a)	-876.367

ZnS(B) beta-sphalerite
ZnS(W) wurtzite
ZnO(RS) rock salt

Table A3. Fe species

Species	$\Delta_f G^0$ kJ/mol
Fe	0.000
Fe(A)	-0.012
Fe(FCC)	5.301
Fe0.945O	-242.652
Fe0.947O	-245.189
FeO	-244.169
FeO1.056	-257.816
FeO1.5(W)	-343.260
Fe2O3	-742.826
Fe3O4	-1012.343
FeO*OH	-490.520
FeO*OH(L)	-482.630
Fe(OH)2	-486.971
Fe(OH)3	-703.282
Fe2O3*H2O	-975.834
Fe2O3*3H2O	-1398.665
Fe(OH)SO4	-1013.611
Fe(OH)SO4*1.5H2O	-1373.513
Fe(OH)SO4*2H2O	-1492.626
Fe(OH)SO4*2H2O(P)	-1493.226
Fe(OH)SO4*3H2O	-1730.466
Fe(OH)SO4*3.5H2O	-1845.223
Fe(OH)SO4*5H2O	-2202.734
Fe0.877S	-106.869
Fe0.9S	-99.561
FeS	-101.174
FeS(LT)	-102.354

Fe(A) ferrite (α-delta iron)
FeO1.5(W) wurtzite
FeO*OH(L) lepidocrocite
Fe(OH)SO4*2H2O(P) parabutlerite
FeS(LT) low troililte

Table A3. (continued) Fe species

Species	$\Delta_f G^0$ kJ/mol
FeS(P)	-100.864
FeS2	-160.164
FeS2(M)	-155.513
Fe2S	-44.703
Fe2S3	-280.455
FeSO4	-824.886
Fe2(SO4)3	-2264.372
FeSO4*H2O	-1079.270
FeSO4*4H2O	-1796.792
FeSO4*7H2O	-2509.738
Fe2(SO4)3*7H2O	-3964.882
Fe2(SO4)3*9H2O	-4440.666
FeO(a)	-212.192
Fe(OH)2(a)	-393.429
Fe(OH)3(a)	-476.316
FeS(a)	6.566
FeSO3(a)	-565.546
Fe(+2a)	-78.873
Fe(+3a)	-17.287
FeO(+a)	-222.142
FeO2(-a)	-387.612
FeOH(+a)	-275.496
FeOH(+2a)	-241.959
Fe(OH)2(+a)	-452.196
Fe(OH)3(-a)	-620.038
Fe(OH)4(-a)	-849.288
Fe(OH)4(-2a)	-774.545
Fe2(OH)2(+4a)	-467.532
FeSO4(+a)	-772.599

FeS2(M) marcasite
FeS(P) pyrrhotite

Table A4. Cu species

Species	$\Delta_f G^0$ kJ/mol
Cu	0.000
Cu(FCC)	0.012
CuO	-127.469
CuO(T)	-127.878
Cu2O	-147.844
Cu(OH)2	-372.709
CuO*CuSO4	-792.255
CuS	-53.748
Cu2S	-88.622
CuSO4	-662.198
Cu2SO4	-654.503
CuSO4*H2O	-914.761
CuSO4*3H2O	-1400.131
CuSO4*5H2O	-1879.859
CuSO4*3Cu(OH)2	-1818.434
CuHS(a)	-14.213
CuO(a)	-87.158
CuOH(a)	-107.279
CuSO3(a)	-421.110
Cu2SO4(a)	-645.542
Cu(+a)	49.982
Cu(+2a)	65.040
Cu(HS)2(-a)	-24.535
CuO2(-2a)	-172.462
CuOH(+a)	-126.397
Cu(OH)3(-a)	-501.517
Cu(OH)4(-2a)	-656.762
Cu2OH(+3a)	-68.716
Cu2(OH)2(+2a)	-283.780
Cu3(OH)4(+2a)	-633.543
HCuO2(-a)	-251.442

CuO(T) tenorite

Table A5. Cd species

Species	$\Delta_f G^0$ kJ/mol
Cd	0.000
Cd(A)	-0.585
CdO	-229.305
Cd(OH)2	-474.546
(CdO)2*CdSO4	-1280.489
CdS	-156.263
CdSO4	-822.789
CdSO4*H2O	-1068.930
CdSO4*2.667H2O	-1465.053
CdSO4*2.67H2O	-1465.151
CdO(a)	-198.728
CdS(a)	7.797
CdSO3(a)	-564.315
CdSO4(a)	-836.635
CdS2O3(a)	-594.228
Cd(+2a)	-77.710
CdO2(-2a)	-281.689
CdOH(+a)	-257.461
Cd(OH)4(-2a)	-756.706
Cd2OH(+3a)	-341.211
Cd4(OH)4(+4a)	-1076.425
Cd(S2O3)2(-2a)	-1146.417
Cd(S2O3)3(-4a)	-1667.141
HCdO2(-a)	-362.033

Cd(A) α-cadmium

Table A6. Pb species

Species	$\Delta_f G^0$ kJ/mol
Pb	0.000
PbO	-188.641
PbO(R)	-188.924
PbO2	-217.372
Pb2O3	-406.601
Pb3O4	-601.591
Pb(OH)2	-422.749
PbO*PbSO4	-1022.920
*2PbO*PbSO4	-1229.955
*3PbO*PbSO4	-1427.362
*4PbO*PbSO4	-1604.712
PbS	-98.726
Pb2S2	29.500
PbSO3	-591.642
PbSO4	-813.033
PbS2O3	-575.041
PbS3O6	-1021.711
Pb(HS)2(a)	-83.770
Pb(HSO3)2(a)	-997.695
Pb(HSO4)2(a)	-1515.428
PbO(a)	-164.566
Pb(OH)2(a)	-338.950
PbS(a)	61.043
PbSO3(a)	-511.069
PbSO4(a)	-769.935
PbS2O3(a)	-540.982
HPbO2(-a)	-338.980
Pb(+2a)	-24.237
Pb(HS)3(-a)	-83.280
PbOH(+a)	-225.900
Pb3(OH)4(+2a)	-888.234
Pb4(OH)4(+4a)	-936.369
Pb6(OH)8(+4a)	-1800.151

PbO(R) Litharge tetragonal

Table A7. Sb species

Species	$\Delta_f G^0$ kJ/mol
Sb	0.000
SbO2	-397.979
Sb2O3	-633.643
Sb2O3(O)	-626.332
Sb2O4	-795.895
Sb2O5	-829.185
Sb4O6	-1249.443
Sb4O6(C)	-1274.514
Sb2O3*3H2O	-1279.874
Sb2S3	-149.787
Sb2(SO4)3	-2066.501
HSbO2(a)	-407.483
Sb(OH)3(a)	-644.622
SbO(+a)	-175.684
SbO2(-a)	-344.690
Sb(OH)4(-a)	-813.060
Sb2S4(-2a)	-99.295

Sb2O3(O) valentinite (orthorhombic)
Sb4O6(C) cubic

Table A8. As species

Species	$\Delta_f G^0$ kJ/mol
As	0.000
As(A)	14.741
As(Y)	20.932
As2O3	-576.651
As2O3(A)	-576.686
As2O3(C)	-577.403
As2O3(OR)	-576.156
As2O4	-700.859
As2O5	-774.821
As4O6	-1151.926
As4O6(C)	-1151.746

Table A8. (continued) As species

Species	$\Delta_f G^0$ kJ/mol
AsS	-38.032
AsS(A)	-30.351
AsS(B)	-29.730
As2S2	-68.521
As2S3	-92.424
As2S3(A)	-84.671
As2S3(AM)	-76.564
As2S3(G)	-69.512
As2S5	-97.286
As4S3	-125.797
As4S4	-132.686
As4S4(B)	-130.991
AsH3(a)	80.627
HAsO2(a)	-402.778
H3AsO3(a)	-639.596
H3AsO4(a)	-766.618
AsO2(-a)	-349.841
AsO3(-3a)	-447.415
AsO4(-3a)	-646.229
As(OH)4(-a)	-824.102
HAsO3(-2a)	-523.697
HAsO4(-2a)	-713.591
H2AsO3(-a)	-587.537
H2AsO4(-a)	-753.512

As(A) amorphous arsenic
As(Y) yellow arsenic
As2O3(A) arsenolite
As2O3(C) claudetite
As2O3(OR) orthorhombic arsenic(III)oxide
As4O6(C) cubic arsenic oxide
AsS(A) alpha realgar
AsS(B) beta realgar
As2S3(A) orpiment
As2S3(AM) amorphous orpiment
As2S3(G) diarsenic trisulfide (glass)
As4S4(B) beta realgar

Table A9. Hg species

Species	$\Delta_f G^0$ **kJ/mol**
Hg	0.000
HgO	-58.575
Hg2O	-54.464
HgS	-52.215
HgS(A)	-40.245
HgS(M)	-43.153
Hg2S	-11.786
HgSO4	-548.854
Hg2SO4	-625.701
HgSO4*HgO	-625.922
HgSO4*2HgO	-753.364
Hg(a)	37.224
HgO(a)	-37.312
Hg(OH)2(a)	-270.113
Hg2(OH)2(a)	-160.885
HgS(H2S)2(a)	-82.788
HgSO3(a)	-321.952
HgSO4(a)	-580.818
Hg2SO4(a)	-591.868
HHgO2(-a)	-188.854
Hg(+2a)	164.662
Hg2(+2a)	153.647
HgOH(+a)	-52.936
Hg2OH(+3a)	112.388
Hg2(OH)2(+2a)	-117.041

HgS(A) red mercury sulfide
HgS(B) black mercury sulfide

APPENDIX B: Eh – pH diagrams of Me-S-O-H systems

The Eh – pH diagrams shown in this appendix have been generated by including the data for all the species listed in appendix A in the calculations. Thus, these figures correspond to the thermodynamically most stable situation. However, it should be remembered that these figures can lead to incorrect conclusions if data for some stable species is missing, or it is otherwise deficit, which is quite probable. Also, it is possible that kinetic barriers prevent the real system from ever reaching the true equilibrium under ambient conditions. It is advised to refer to section 3.3 for a brief discussion on the principles and limitations of the Eh – pH diagrams.

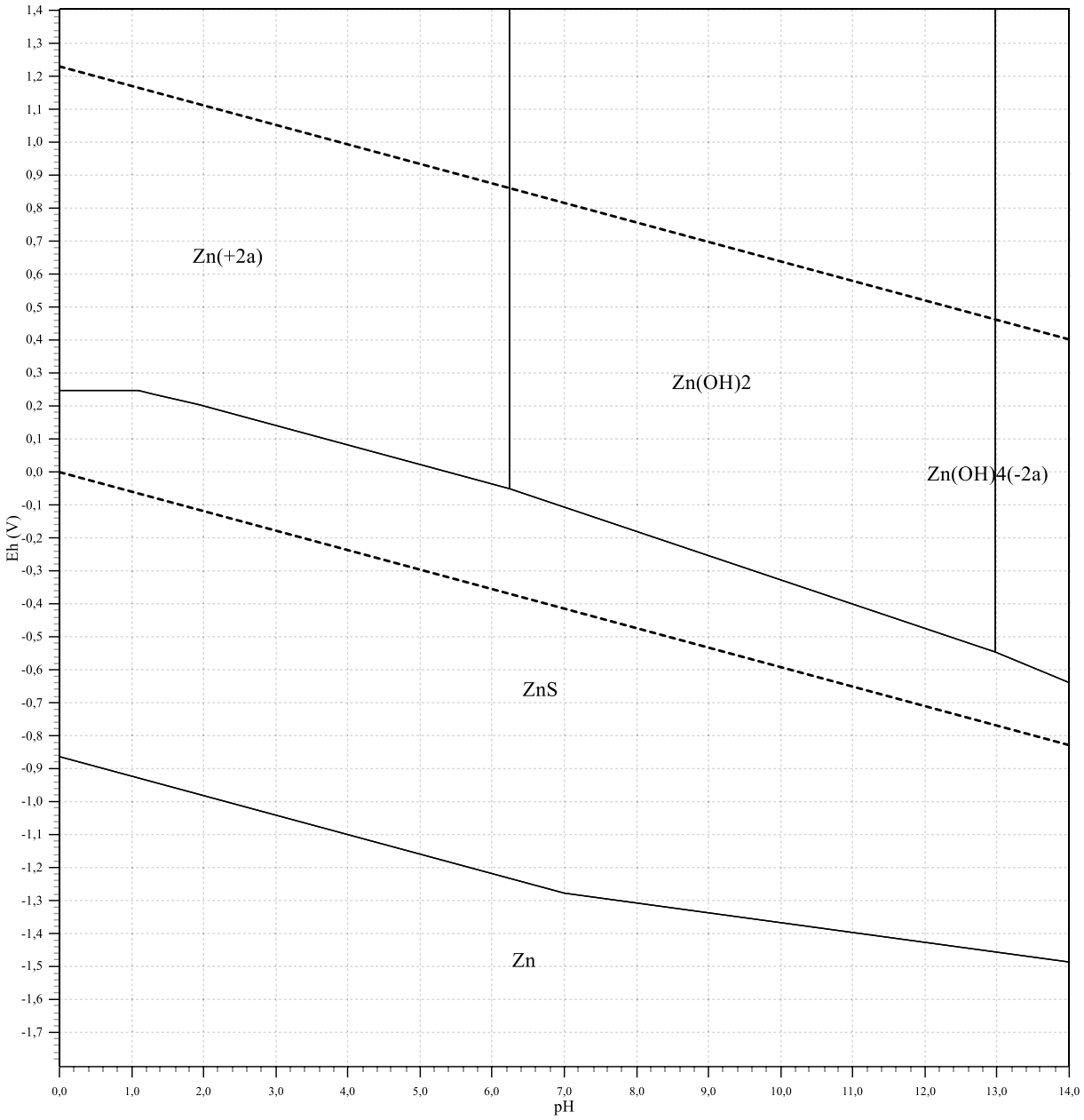

Fig B1. The Eh – pH diagram of the Zn-S-H_2O system at $T = 298.15$ K, $p = 0.1$ Mpa and total zinc and sulfur molalities of 0.1 mol/kg.

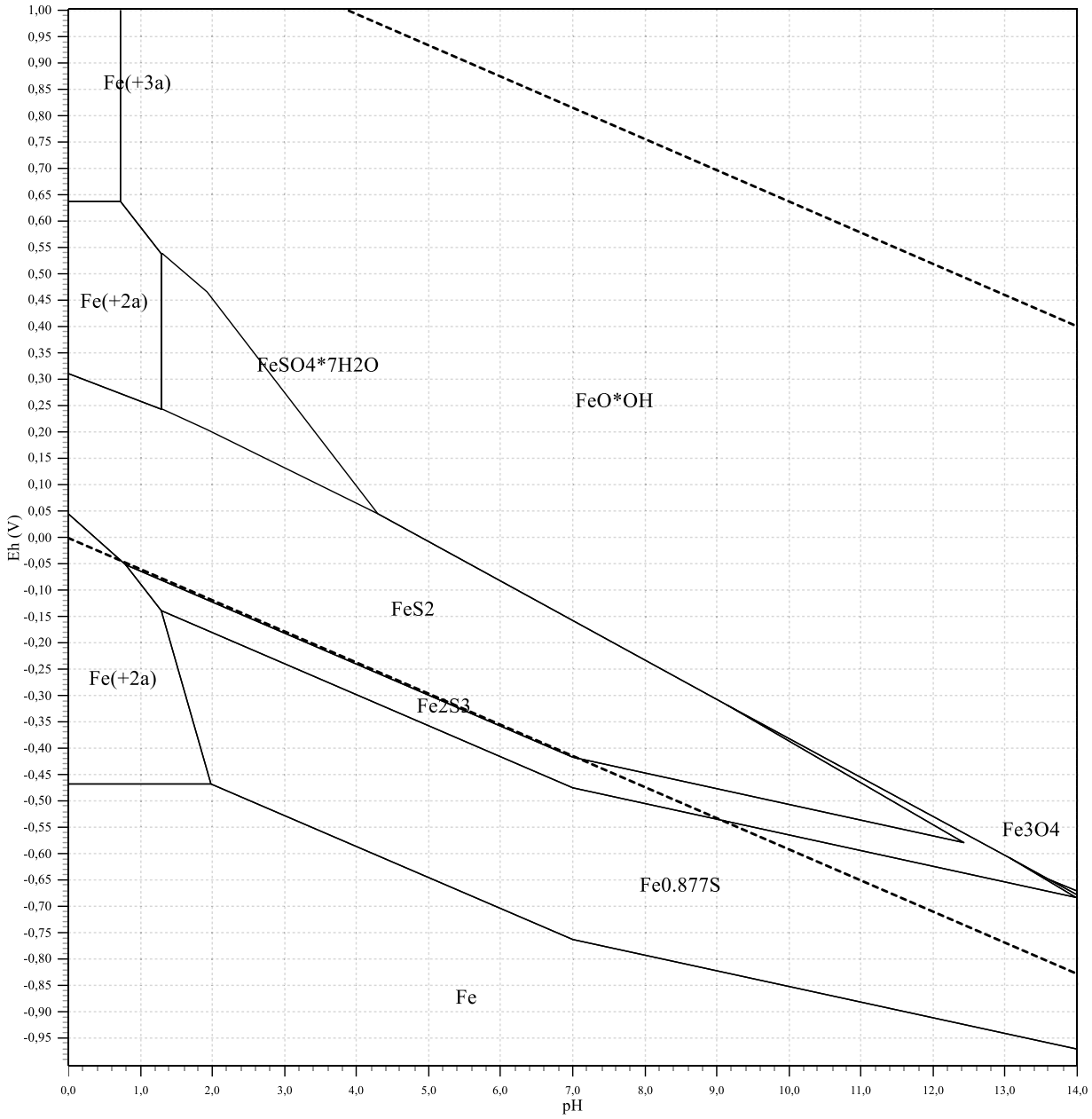

Fig B2. The Eh – pH diagram of the Fe-S-H_2O system at $T = 298.15$ K, $p = 0.1$ Mpa and total iron and sulfur molalities of 0.01 mol/kg.

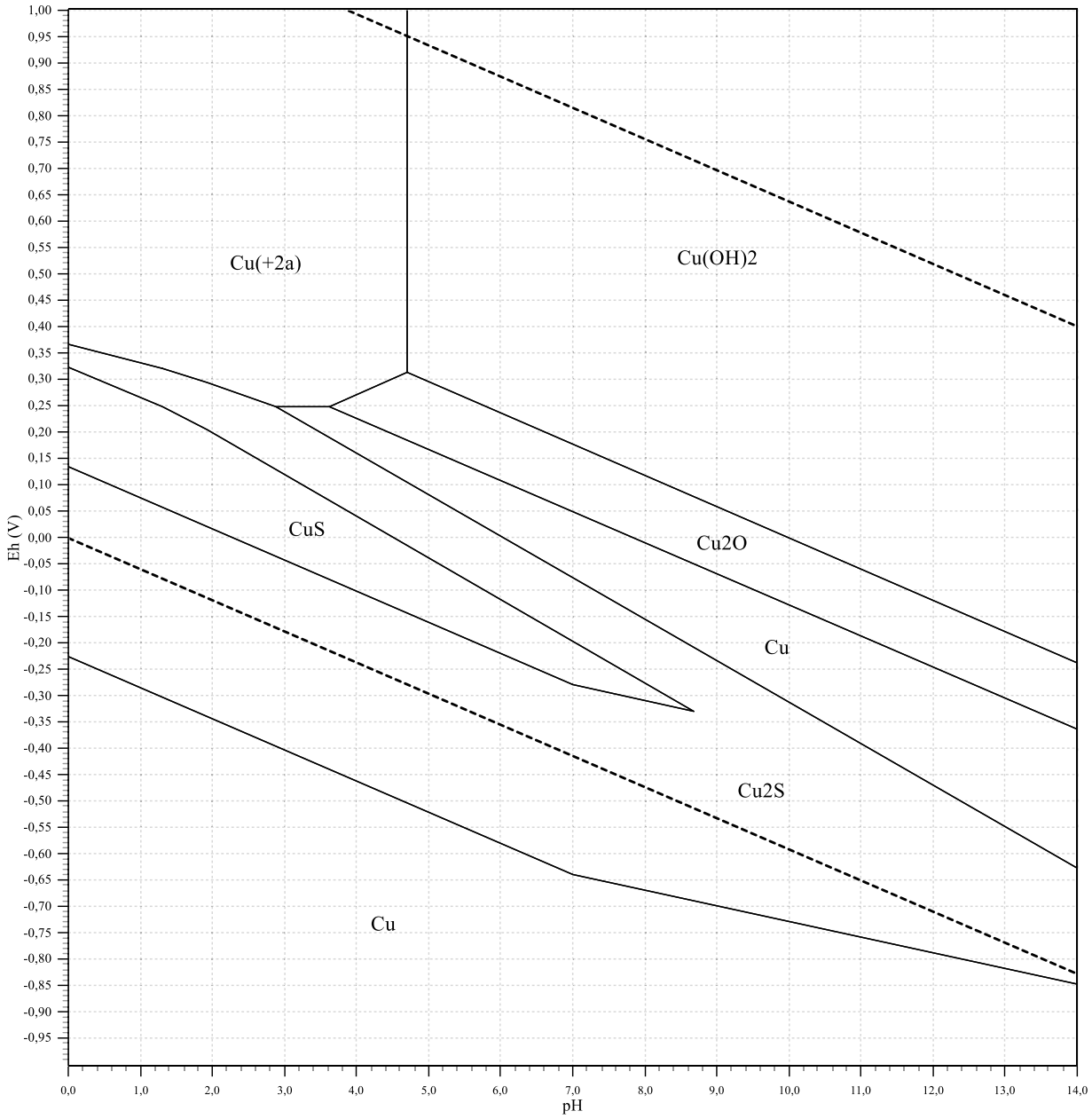

Fig B3. The Eh – pH diagram of the Cu-S-H_2O system at $T = 298.15$ K, $p = 0.1$ Mpa and total copper and sulfur molalities of 0.001 mol/kg.

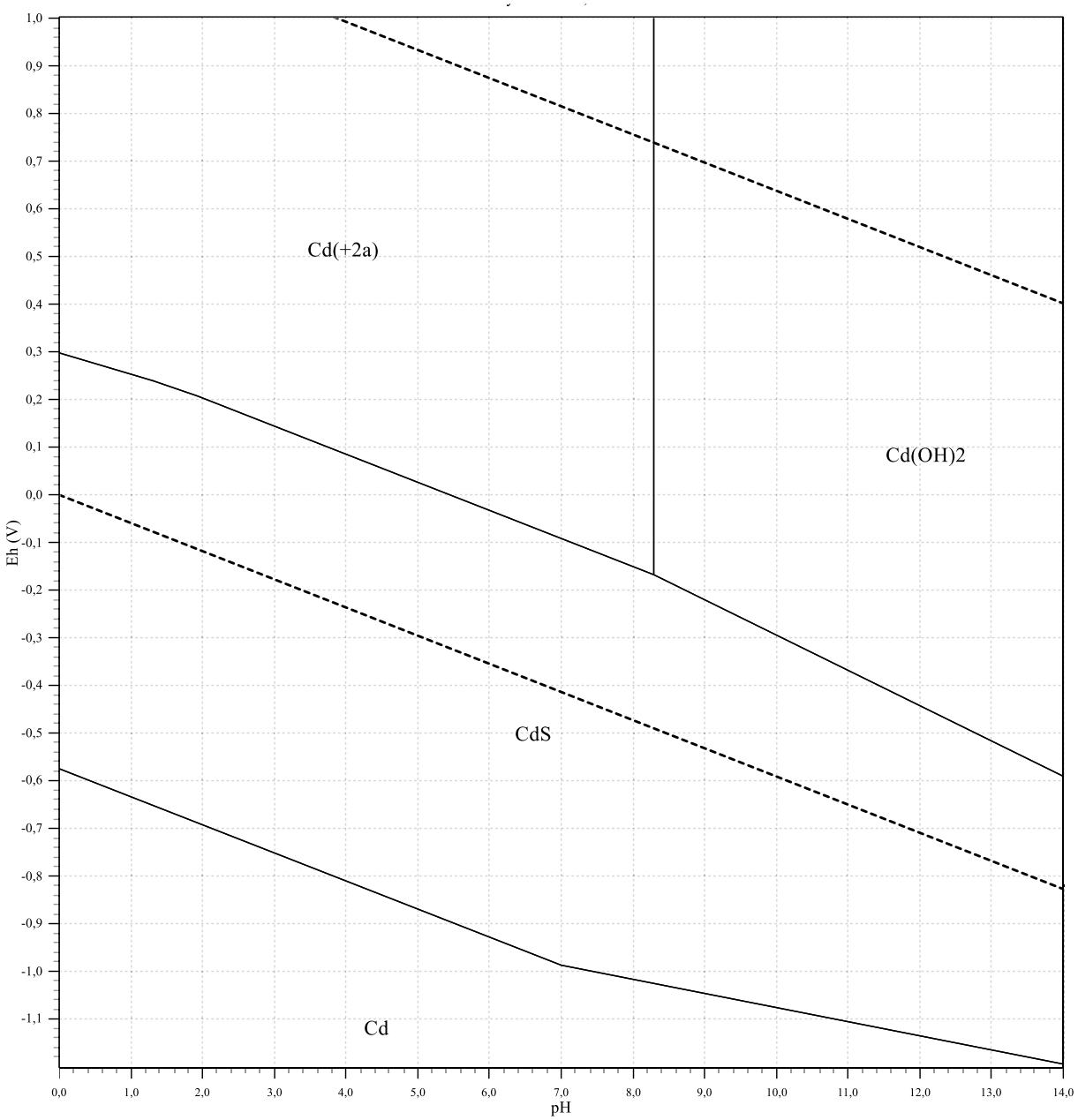

Fig B4. The Eh – pH diagram of the Cd-S-H_2O system at $T = 298.15$ K, $p = 0.1$ Mpa and total cadmium and sulfur molalities of 0.001 mol/kg.

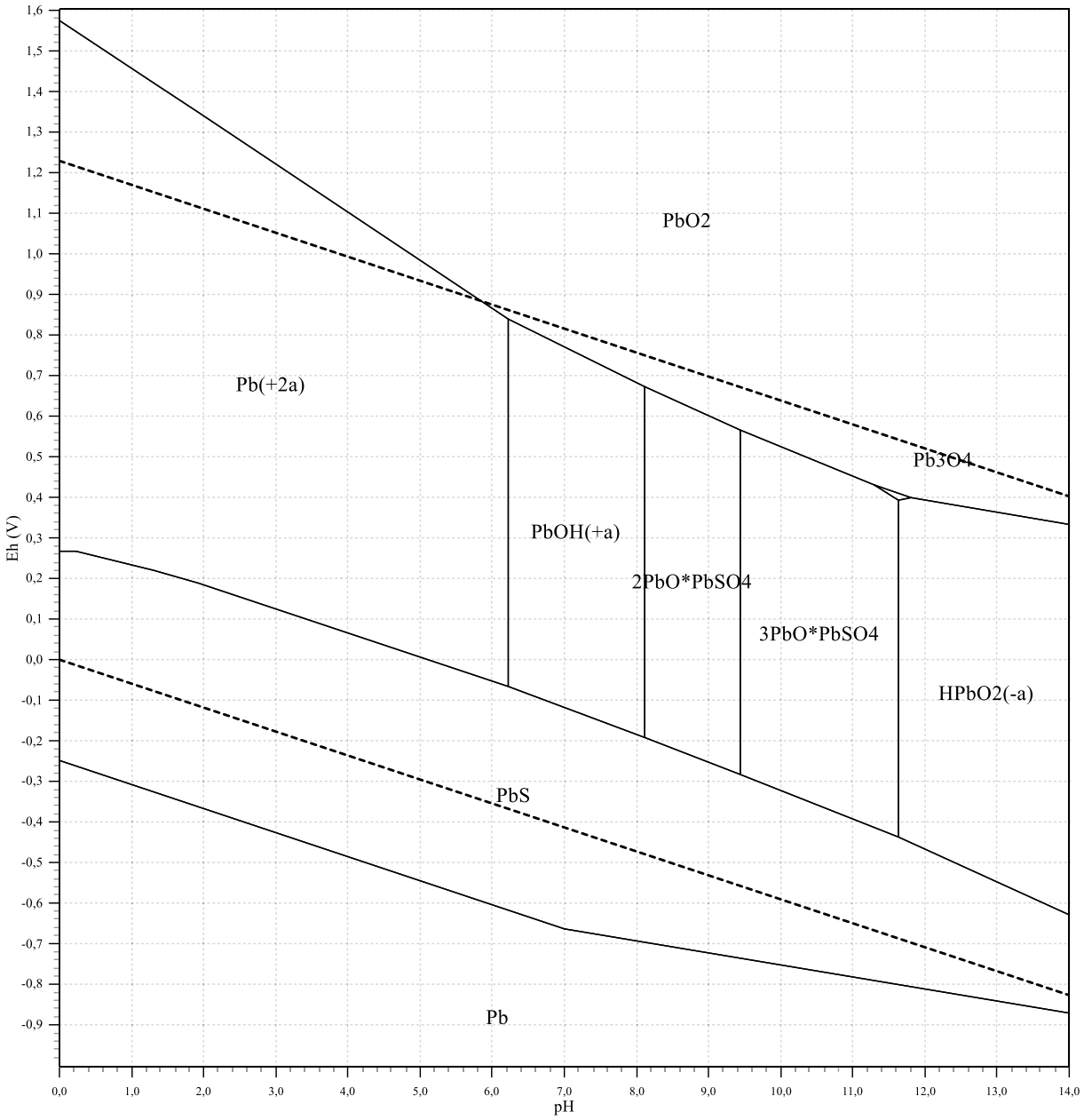

Fig B5. The Eh – pH diagram of the Pb-S-H_2O system at $T = 298.15$ K, $p = 0.1$ Mpa and total lead and sulfur molalities of $1 \cdot 10^{-4}$ mol/kg.

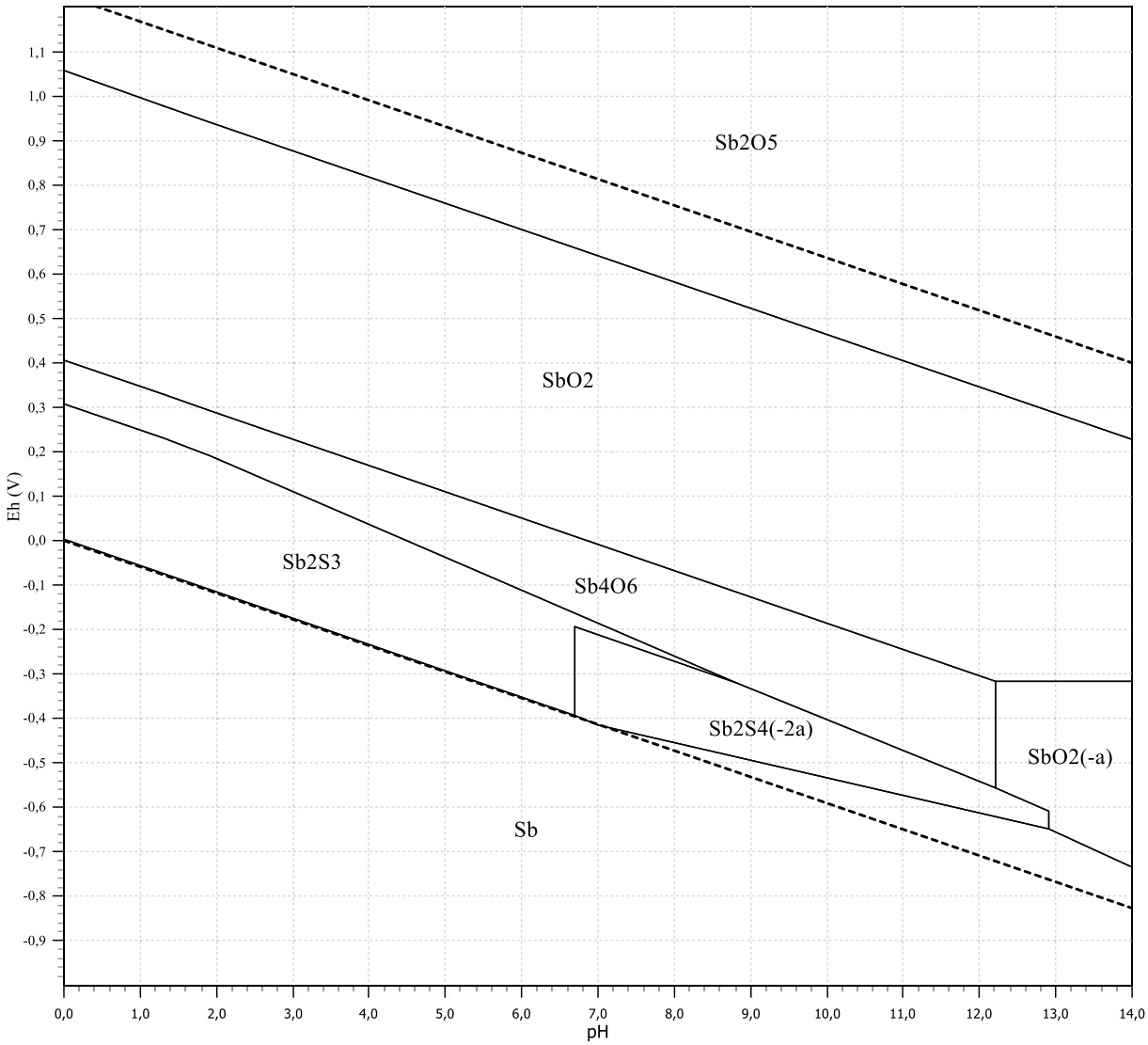

Fig B6. The Eh – pH diagram of the Sb-S-H_2O system at $T = 298.15$ K, $p = 0.1$ Mpa and total antimony and sulfur molalities of $1 \cdot 10^{-4}$ mol/kg.

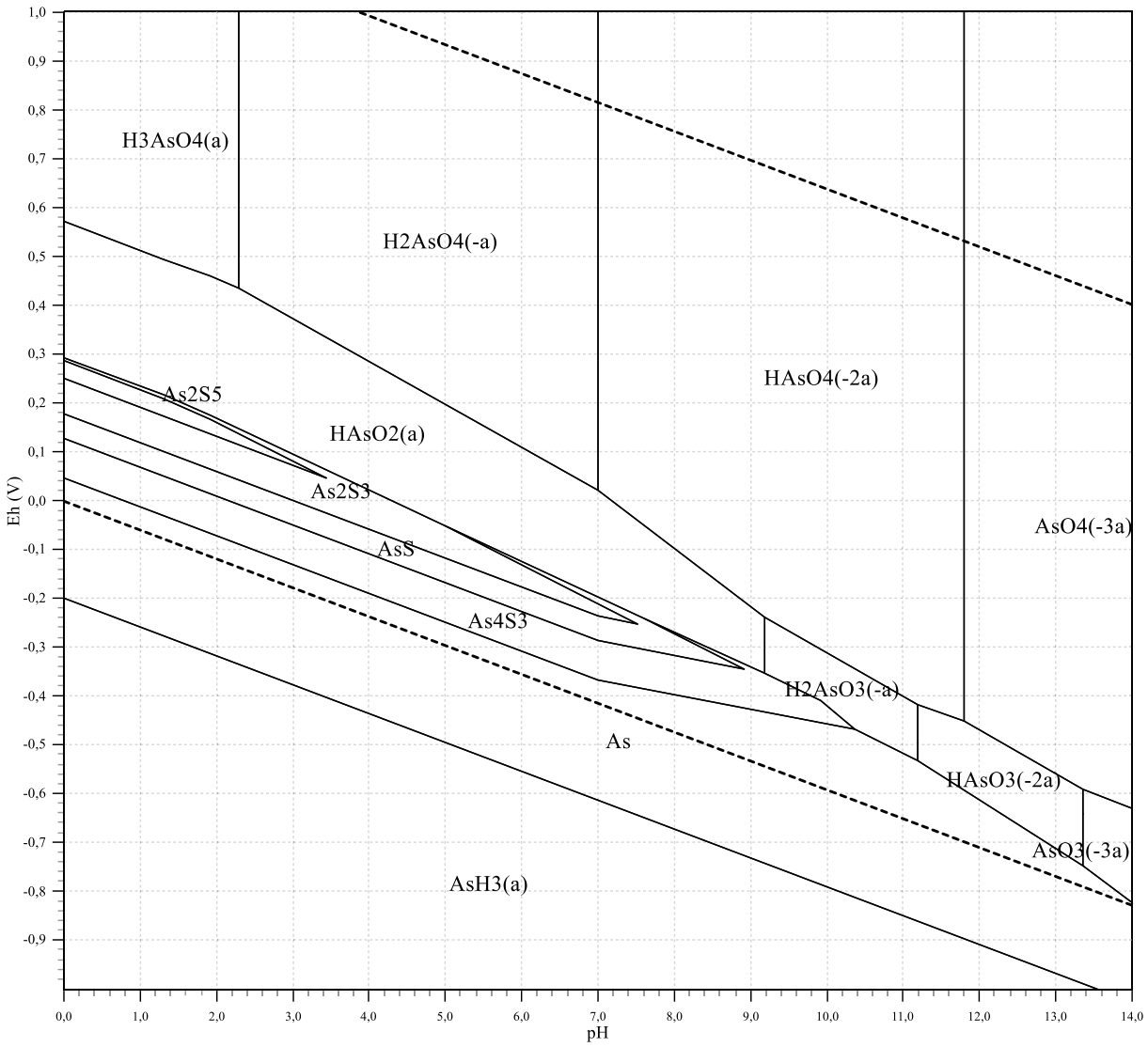

Fig B7. The Eh – pH diagram of the As-S-H_2O system at $T = 298.15$ K, $p = 0.1$ Mpa and total arsenic and sulfur molalities of $1 \cdot 10^{-4}$ mol/kg.

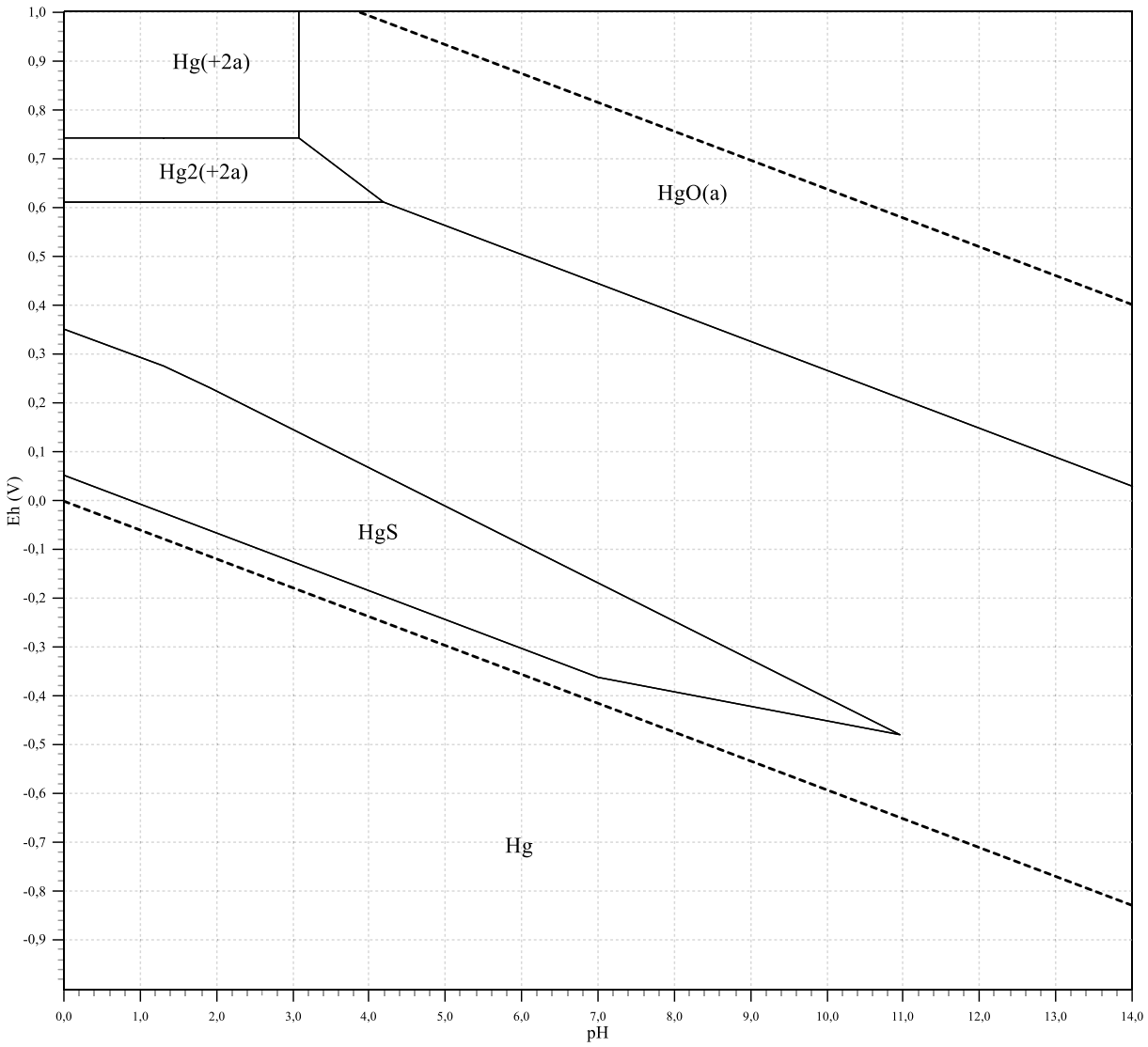

Fig B8. The Eh – pH diagram of the Hg-S-H_2O system at $T = 298.15$ K, $p = 0.1$ Mpa and total mercury and sulfur molalities of $1 \cdot 10^{-6}$ mol/kg.

APPENDIX C: Speciation Models for Selected Metal Sulfides

In this appendix, a few examples of speciation diagrams for Me-S-O-H systems constructed from literature data are presented. Note that these figures correspond to a total S(-II) concentration of 0.01 mol/kg. To determine speciation at any other S(-II) concentration, the figures must be recalculated by solving the appropriate set of equations with the new S(-II) concentration in the material balance.

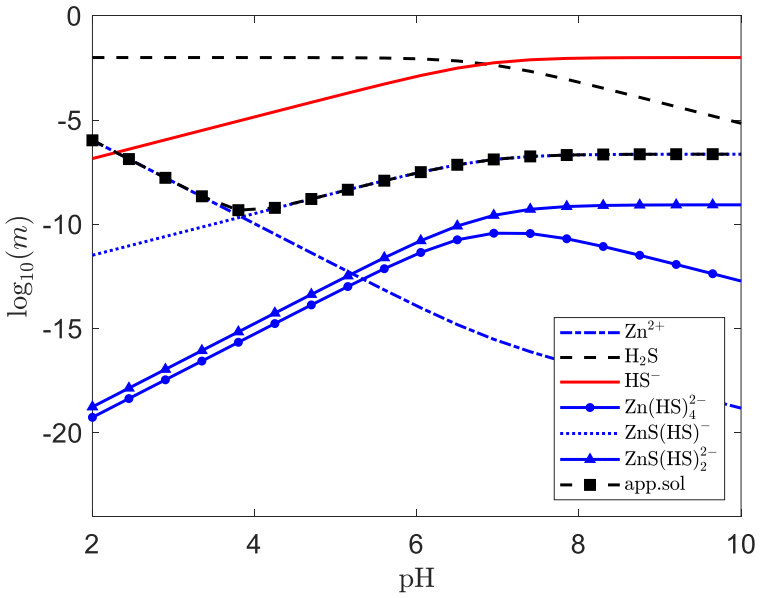

Figure C1. Apparent solubility of sphalerite (app.sol) and the molalities of individual species as functions of pH according to Daskalakis and Helz[63]. $T = 298.15$ K, $I = 0.3$ mol/kg and $m_{\mathrm{S(-II),tot}} = 10^{-2}$ mol/kg.

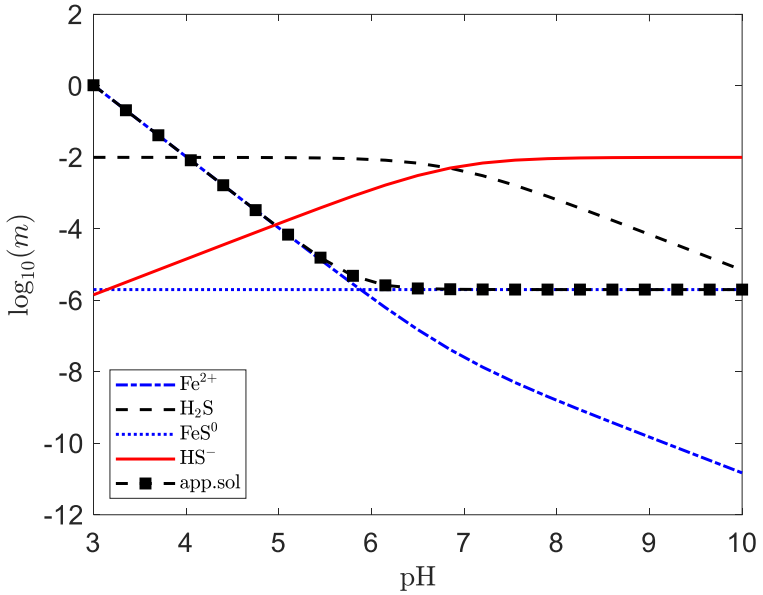

Figure C2. Apparent solubility of amorphous FeS (app.sol) and the molalities of individual species as functions of pH according to Rickard[64]. $T = 298.15$ K, $I = 0.3$ mol/kg and $m_{\mathrm{S(-II),tot}} = 10^{-2}$ mol/kg.

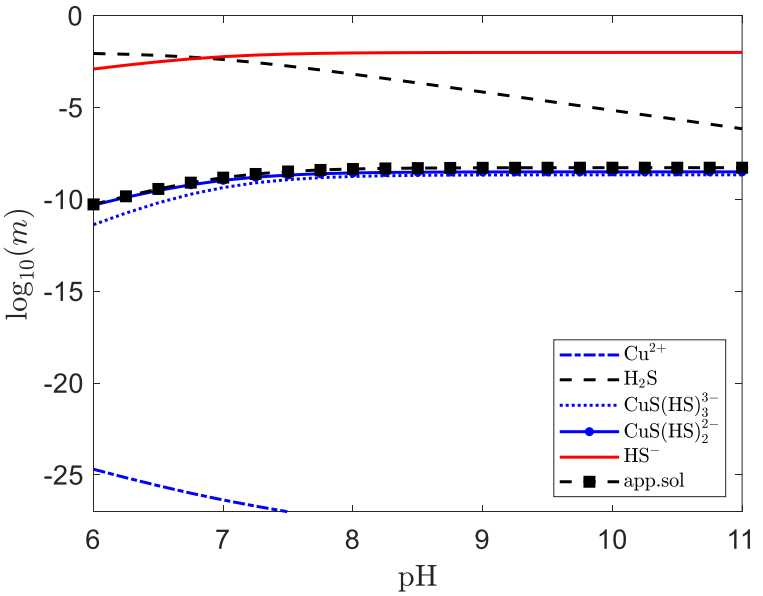

Figure C3. Apparent solubility of covellite CuS (app.sol) and the molalities of individual species as functions of pH according to Shea and Helz[10, 83]. $T = 298.15$ K, $I = 0.3$ mol/kg and $m_{\mathrm{S(-II),tot}} = 10^{-2}$ mol/kg.

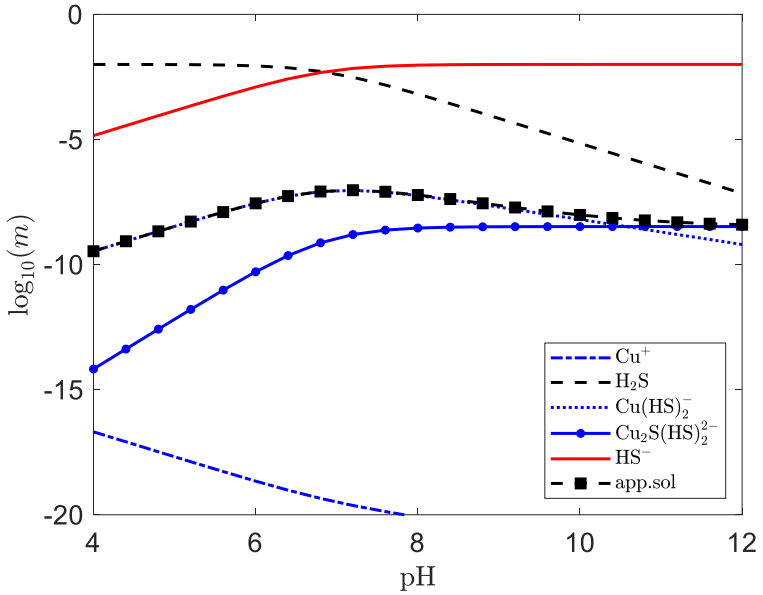

Figure C4. Apparent solubility of chalcocite Cu_2S (app.sol) and the molalities of individual species as functions of pH according to Mountain and Seward[86]. $T = 298.15$ K, $I = 0.3$ mol/kg and $m_{S(-II),tot} = 10^{-2}$ mol/kg.

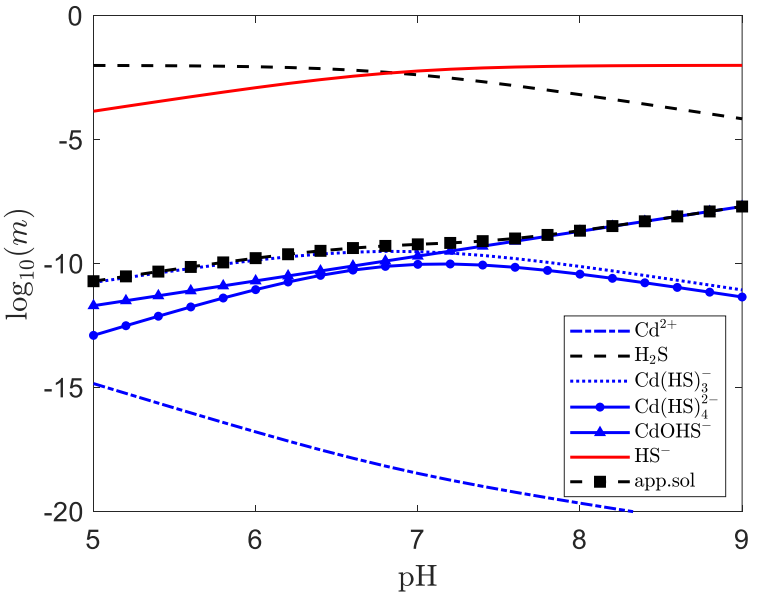

Figure C5. Apparent solubility of greenockite CdS (app.sol) and the molalities of individual species as functions of pH according to Daskalakis and Helz[80]. $T = 298.15$ K, $I = 0.3$ mol/kg and $m_{S(-II),tot} = 10^{-2}$ mol/kg.

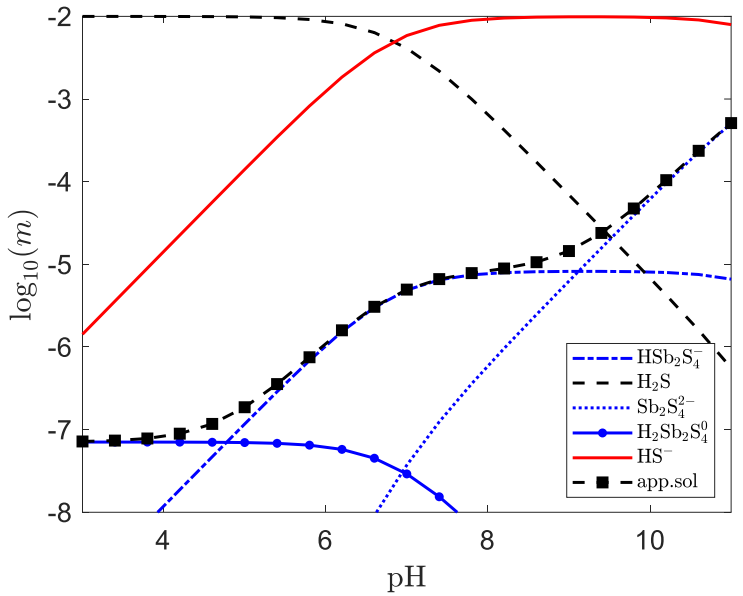

Figure C6. Apparent solubility of stibnite Sb_2S_3 (app.sol) and the molalities of individual species as functions of pH according to Krupp[89]. $T = 298.15$ K, $I = 0.3$ mol/kg and $m_{\mathrm{S(-II),tot}} = 10^{-2}$ mol/kg.

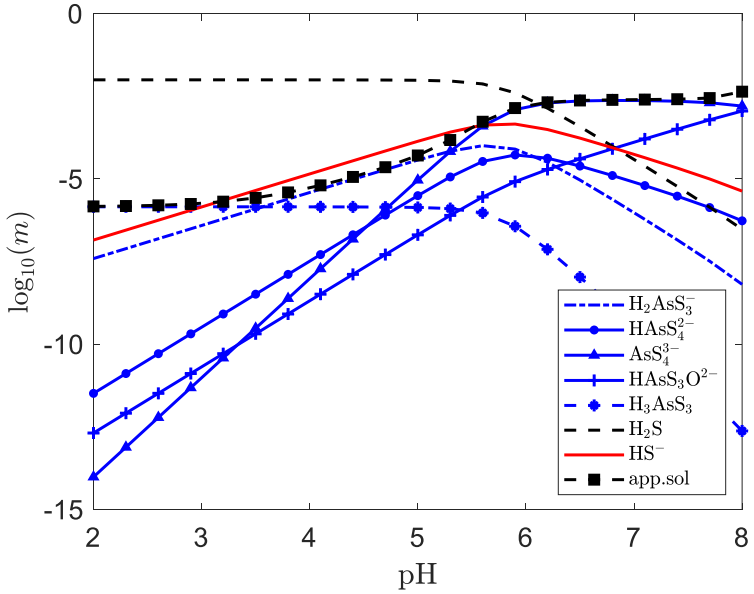

Figure C7. Apparent solubility of orpiment As_2S_3 (app.sol) and the molalities of individual species as functions of pH according to Helz and Tossel[90]. Only major species shown. As_2S_3 has been assumed to be in equilibrium with AsS, so $a_{S^0} = 3.91$. $T = 298.15$ K, $I = 0.3$ mol/kg and $m_{\mathrm{S(-II),tot}} = 10^{-2}$ mol/kg.

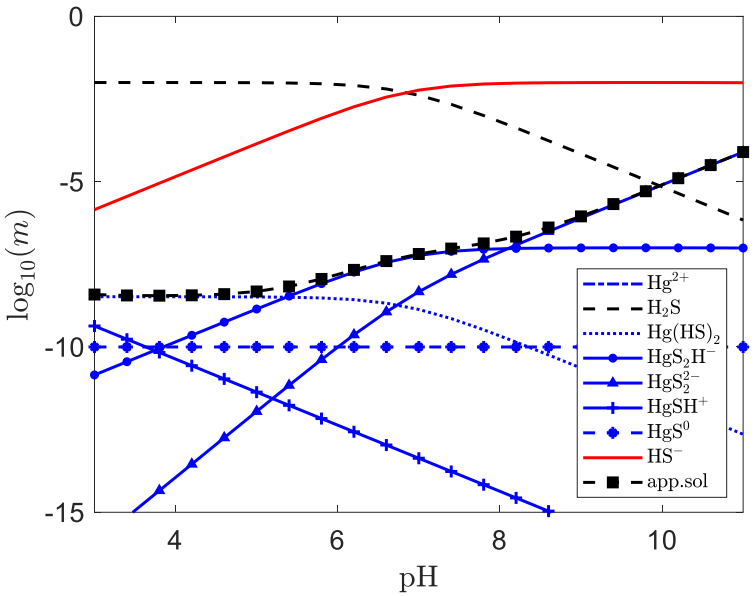

Figure C8. Apparent solubility of HgS (red) (app.sol) and the molalities of individual species as functions of pH according to Benoit et al.[88] $T = 298.15$ K, $I = 0.3$ mol/kg and $m_{\mathrm{S(-II),tot}} = 10^{-2}$ mol/kg.